Optical spectroscopy of van der Waals heterostructures

Dissertation
zur Erlangung des Doktorgrades der Naturwissenschaften
(Dr. rer. nat.)
der Fakultät für Physik der Universität Regensburg

vorgelegt von

Johannes Maria Holler
aus Pfaffenhofen an der Ilm

im Jahr 2021

Das Promotionsgesuch wurde eingereicht am: 05.05.2021
Die Arbeit wurde angeleitet von: Prof. Dr. Tobias Korn.

Prüfungsausschuss:	Vorsitzender:	Prof. Dr. Gunnar Bali
	1. Gutachter:	Prof. Dr. Tobias Korn
	2. Gutachter:	Prof. Dr. Sergey Ganichev
	weiterer Prüfer:	Prof. Dr. Franz J. Gießibl

Contents

Chapter 1

Introduction

In the process of writing a doctoral thesis one question is unavoidable. From colleagues to friends to family, eventually they will ask:

What do you do in your doctoral thesis?

The short answer for non-physicists is: "I shoot with lasers on very thin materials and see what happens." Although this answer sounds like a joke it actually hits the nail on the head. Naturally, for physicists a more sophisticated answer is required. Transition metal dichalcogenides (TMDCs) are semiconductors, that exhibit a layered structure and can be mechanically exfoliated down to one layer. In this monolayer limit they feature a direct band gap in the visible regime [Mak10, Spl10], which makes them ideal materials for optical experiments. Additionally, excitonic quasiparticles form in transition metal dichalcogenides at room temperature and allow an absorption of up to 20 % of the incoming light [Li14]. These materials exhibit rich physics, e.g. valleytronics. This allows to address different band extrema in the Brillouin zone with σ^+ and σ^- circularly polarized light, which leads to the so called valley polarization [Cao12, Mak12, Zen12]. By stacking different two-dimensional materials on top of each other van der Waals heterostructures are fabricated. These establish a new research field with countless combination possibilities of different materials.
In the framework of this thesis van der Waals heterostructures consisting predominantly of TMDCs are investigated via optical spectroscopy, specifically Raman scattering and photoluminescence (PL). Chapter 2 introduces the theoretical results and preliminary studies, chapter 3 explains the experimental methods and chapter 4 presents the experimental results. In section 4.1 the two-dimensional insulator hBN, which is used to preserve and improve material properties, is investigated as a protective layer against

air. In section 4.2 the behaviour of the interlayer exciton of $MoSe_2$-WSe_2 heterobilayers in high magnetic fields is presented. Section 4.3 proposes Raman spectroscopy as a non-invasive method to characterize twisted TMDC bilayers. On the one hand, atomic reconstruction can rearrange atomic lattices [Ros20, Wes20], which is investigated by the interlayer shear phonon mode. On the other hand, moiré lattices form. This is studied by folded acoustic phonons [Lin18]. Finally, chapter 5 summarizes the results of this thesis.
As the first question is answered the second question is the logical follow-up:

Why?

This is an important question, which every researcher should ask oneself. There are many reasons for research on van der Waals heterostructures. On the one hand, it improves knowledge and understanding of basic science. The investigation of condensation signatures [Wan19, Sig20], ferromagnetism [Hua17], superconductivity [Uge16], correlated electronic phases[Wan20b], to name a few, gives new insight into physical effects. On the other hand, van der Waals heterostructure based devices like transistors [Che20], photodetectors [Ma18], LEDs [Wan20a] and even neural network applications [Men20] are visionary projects. So the research on van der Waals heterostructures deepens our physical understanding of the world. If it has an influence on our everyday life, remains to be seen.

Chapter 2

Theory

2.1 Material systems

The materials used in this work belong to the group of two-dimensional materials, which have a layered structure in common. The atoms exhibit strong bonds within the layer and weak bonds in between the layers and therefore the layers can be split apart (see section 3.1). By thinning down a material to one monolayer new physics emerge. The most prominent example is graphene whose discovery [Nov04] was awarded with the Nobel prize in physics to Andre Geim and Konstantin Novoselov in 2010. While graphene is a semimetal and therefore is not suitable for the optical experiments conducted in this work there are hundreds of other two-dimensional materials and thousands more are predicted [Ash17, Mou18]. Also semiconductors, insulators and superconductors are represented and the materials relevant for this work are introduced in the following subsections.

2.1.1 Transition metal dichalcogenides

Transition metal dichalcogenides (TMDCs) are materials consisting of a transition metal M and two chalcogenide atoms X with the chemical formula MX_2. The most typical TMDCs are molybdenum disulfide (MoS_2), molybdenum diselenide ($MoSe_2$), tungsten disulfide (WS_2) and tungsten diselenide (WSe_2). In the following, the characteristics for these four TMDCs will be explained in general or on the basis of one of them. If there are important differences between the materials, these will be highlighted.

Crystal structure

The crystal structure for these typical TMDCs (MoS_2, $MoSe_2$, WS_2 and WSe_2) is known since 1923, where it was described for MoS_2 [Dic23]. Fig 2.1 shows a perspective view of the material and the hexagonal structure can be seen in the orthographic top view. In this work, only $MoSe_2$ and WSe_2 were investigated. Their lattice constants are given in table 2.1 where a denotes the distance between two chalcogen atoms in the same plane and c the height of a layer. This is the description of one layer of a TMDC, which will be referred to as a monolayer. While the monolayer has no inversion center it features a 3-fold symmetry (D_{3h}) and strong covalent bonds between the atoms in a layer.

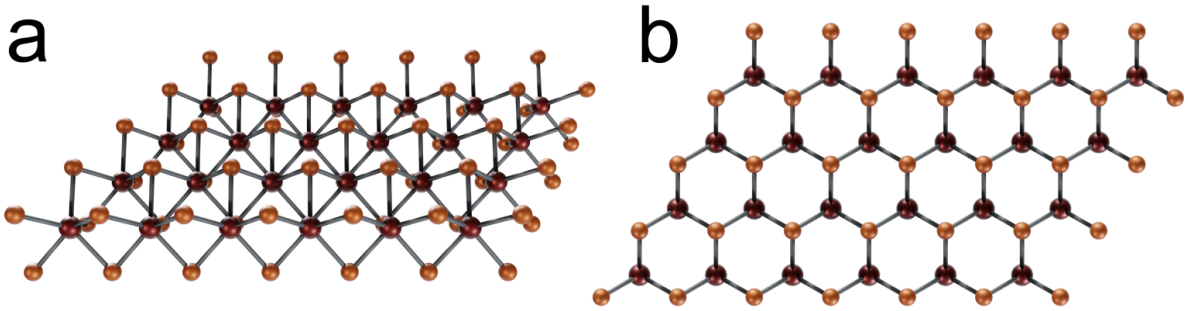

Figure 2.1 | a Perspective view and **b** orthographic top view of a monolayer MX_2. The metal atoms are depicted in red and the chalcogen atoms in orange.

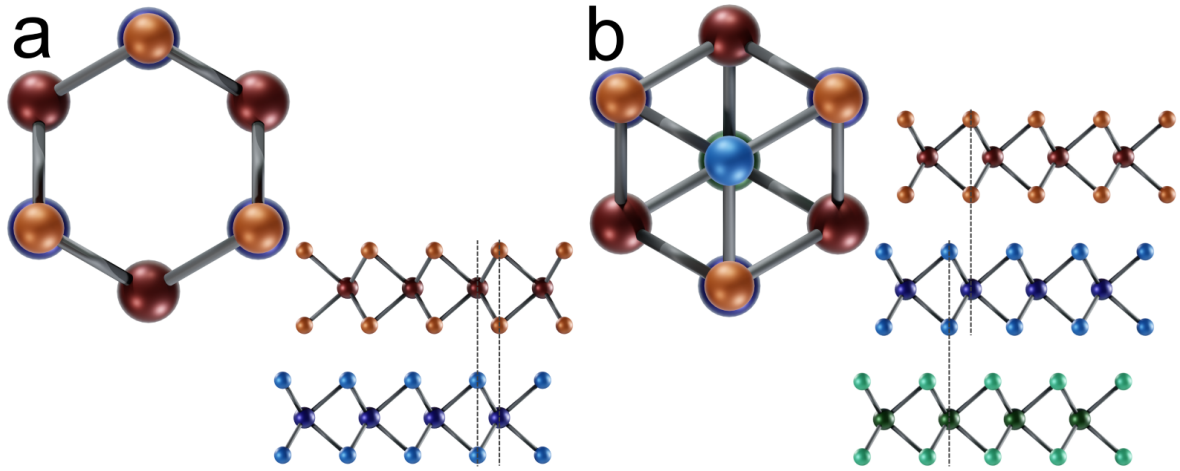

Figure 2.2 | Orthographic top and side view of **a** 2H and **b** 3R stacked MX_2.

The bulk material is build from monolayers stacked on top of each other. In contrast to the strong bonds in the layer, between the layers only weak van der Waals forces prevail. Whether the bulk material has an inversion center depends on the number of

	a (Å)	c (Å)
$MoSe_2$	3.288 [Jam63]	6.46 [Jam63]
WSe_2	3.286 [Hic64]	6.49 [Hic64]

Table 2.1: Bulk lattice constants of $MoSe_2$ and WSe_2.

layers. TMDCs with an even number of layers feature an inversions center, TMDCs with an odd number of layers not. There are two typical stacking configurations:

- In the 2H-stacking two layers next to each other are twisted by 60° and therefore the metal atoms of one layer lies above or below the chalcogen atoms of the neighbouring layer (see Fig 2.2a).
- In the 3R-stacking all the layers have the same orientation and the chalcogen atoms lie above the metal atoms of the layer beneath. Therefore this structure repeats after three layers (see Fig 2.2b).

Of these two stacking configurations the 2H-stacking is more common for bulk material. For artificially stacked multilayers the stacking is more complicated and is explained in section 2.5.1. Strictly speaking, the terms 2H and 3R are only valid for bulk material. Therefore, the terms H-type and R-type will be used for the non bulk TMDC multilayers.

Band structure

To understand the behaviour of a semiconductor knowledge over the band structure is required. Because of the hexagonal shape of the crystal lattice, which can be seen in Fig 2.1b, the TMDCs exhibit a hexagonal Brillouin zone [Bro72]. The first Brillouin zone is depicted in Fig 2.3. The two inequivalent points K^+ and K^- at the corners of the zone are of particular importance.

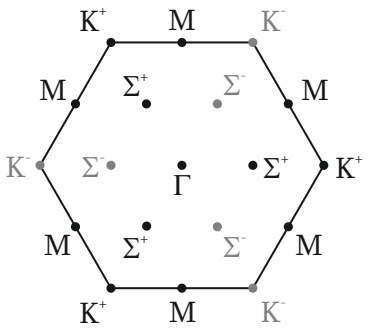

Figure 2.3 | The first Brillouin zone of monolayer TMDCs.

The band structure of the bulk material features an indirect bandgap between the Γ point in the valence band and the K point in the conduction band. This is exemplarily shown for MoS_2 in Fig 2.4. While the states at the K point consist mainly of d-orbitals localized at the metal atoms, the states at the Γ point are influenced by the p_z-orbitals of the chalcogen atoms. These are sensitive to neighbouring layers and therefore the band structure changes with the layer number at the Γ point [Spl10, Kuc11]. When the material is thinned down to one monolayer the band structure undergoes a transition from an indirect bandgap to a direct bandgap at the K point (see Fig 2.4) [Voß99, Leb09, Kad12]. The Σ point, which is also denoted as Q or Λ point in some publications, has a conduction band minimum close to the minimum of the K point. Depending on the material and strain the transition energy between the K point of the valence band and the Σ point of the conduction band is very close to the direct transition at the K point [Ste15]. The dominating transition for optical measurements is at the K point, because the transition from the K to the Σ point is k-space indirect and therefore momentum dark. Due to the direct bandgap at the K point in the monolayer, which is in the energy range of visible light, TMDCs are a very interesting material for optical experiments. Photoluminescence (PL) measurements confirmed the theoretical calculations and are further discussed in section 2.3 [Mak10, Spl10].

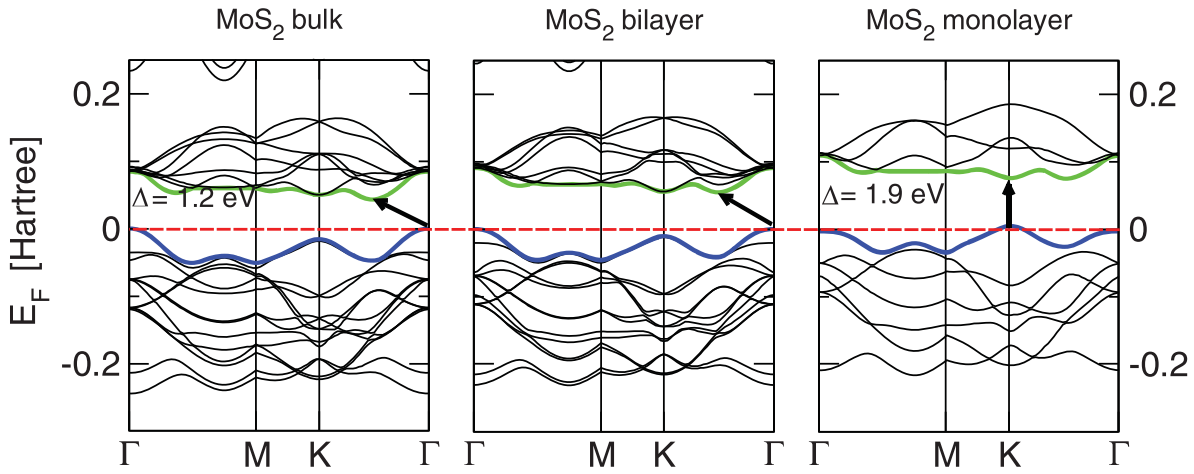

Figure 2.4 | Calculated band structure of bulk, bilayer and monolayer MoS_2. The fundamental bandgap (arrow), the Fermi level (orange), the valence band (blue) and the conduction band (green) are highlighted (adapted from [Kuc11]).

The bulk material is time and inversion symmetric and therefore Kramer's degeneracy holds. In contrast to the bulk material the monolayer has a broken inversion symmetry and due to the spin-orbit interaction the degeneracy is lifted at most points of the Brillouin zone [Zhu11, Kor15]. The spin splitting of the valence and conduction band

for the common TMDCs at the K point is given in table 2.2. As can be seen the splitting in the valence band is in the range of hundreds of meV, while the splitting of the conduction band is rather small and even changes its sign, depending on the material. The valence band can be directly mapped via angle-resolved photoemission spectroscopy (ARPES) and the experimental measurements confirm the calculated spin splitting (see Fig 2.5) [Zha14, Ali14].

	Δ_{VB}(meV)	Δ_{CB}(meV)
MoS_2	148	-3
$MoSe_2$	186	-22
WS_2	429	32
WSe_2	466	37

Table 2.2 | Calculated spin splitting at the K point of the valence (Δ_{VB}) and conduction band (Δ_{CB}) [Kor15].

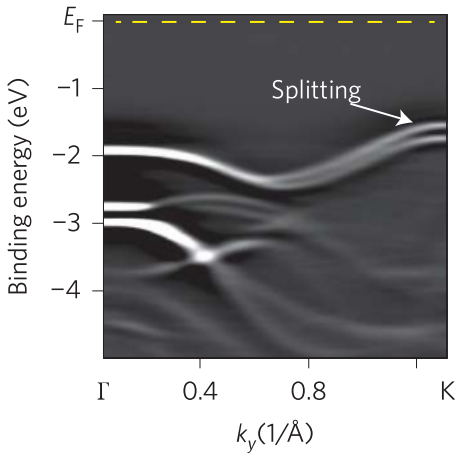

Figure 2.5 | Second-derivative of the ARPES spectra of monolayer $MoSe_2$ along the Γ-K direction [Zha14].

Spin-valley effects

In semiconductor physics a valley is a minimum (maximum) in the conduction (valence) band e.g. the band structure at the K point in TMDCs. These valley physics were already investigated before in materials like aluminium arsenide quantum wells [Shk02] or silicon heterostructures [Tak06] and are known as valleytronics. The special feature of TMDC monolayers is that these valleys are distinguishable at the K^+ and K^- point, can be selectively addressed by circularly polarized light and are locked to the spin polarization.

As discussed above the bands at the K point are spin split with a large splitting at the valence band maximum and a small splitting at the conduction band minimum. Because optical transitions in TMDC monolayers are spin-conserving there are two possibilities. An electron-hole pair can form an exciton between the upper valence band and the corresponding conduction band (A exciton) or between the lower valence band and the corresponding conduction band (B exciton). Only the energetically lowest allowed transition is bright in optical experiments like PL measurements. For the K^+ valley this

transition is between spin up bands and for the K^- valley between spin down bands. Therefore the spin is locked to the valley [Kor15]. This is illustrated in Fig 2.6. It has to be noted, that the energetically lowest transition is not always optically allowed. Excitonic effects will be discussed in section 2.2.

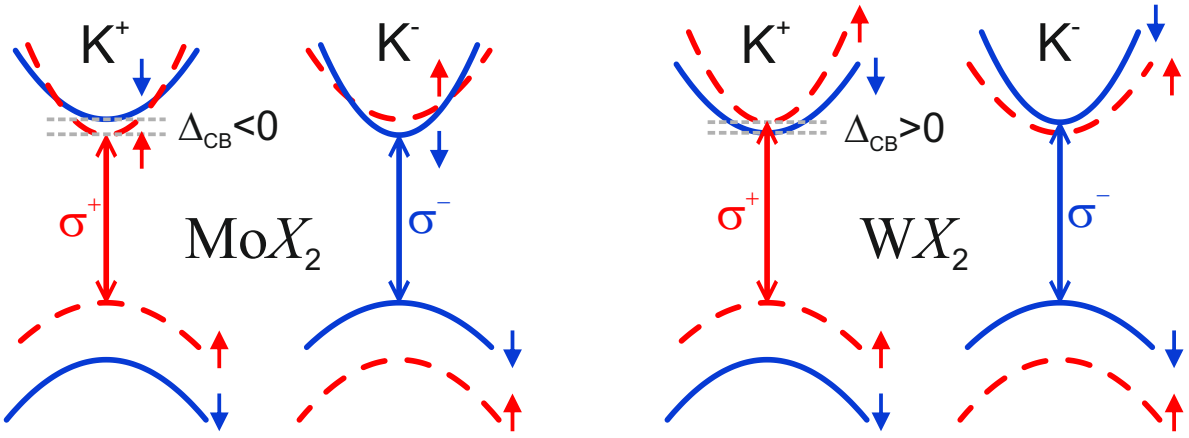

Figure 2.6 | Schematic illustration of the band structure at the K points for MoX_2 and WX_2. The spin polarization of the bands, the conduction band splitting (Δ_{CB}) and the circular polarization of the energetically lowest allowed transition is marked [Wan18].

In monolayer TMDCs selection rules for circularly polarized light prevail. The transition in the K^+ valley can only be accessed via σ^+ polarized light and the transition in the K^- valley only via σ^- polarized light (see Fig 2.6). The reason for these optical selection rules is the broken inversion symmetry of the monolayer and the C_{3h} symmetry at the K points [Yao08, Xia12]. Therefore the K^+ and the K^- valley can be selectively excited and probed with circularly polarized light. This additional information is called valley pseudospin and can be understood as an additional degree of freedom besides charge and spin. The pseudospin is directly coupled to the spin due to the particular configuration of the band structure. By exciting and probing the different valleys with σ^+ and σ^- polarized light the optical selection rules can be utilized in PL measurements, which is shown in Fig 2.7a and b. As expected, for σ^+ polarized excitation the PL yields more σ^+ polarized light and vice versa. This effect is quantified by the valley polarization P, which is defined by the difference of the emitted intensities of σ^+ polarized light I_{σ^+} and σ^- polarized light I_{σ^-} normalized by their sum and was already measured for monolayer TMDCs [Cao12, Mak12, Zen12].

$$P = \frac{I_{\sigma^+} - I_{\sigma^-}}{I_{\sigma^+} + I_{\sigma^-}}$$

This valley polarization can reach values near unity [Mak12, Wu13]. For bright excitons the limiting factor for the valley polarization lifetime is the electron-hole exchange interaction. The lifetime is further reduced by an increase of the excitation laser energy, temperature or excitation density [Sch16a]. Fig 2.7c shows a pump-probe measurement of the valley polarization lifetime which is in the order of $1 - 100\,\mathrm{ps}$ for TMDC monolayers, depending on the specific material, temperature and excitation conditions [Mai14, Dal15].

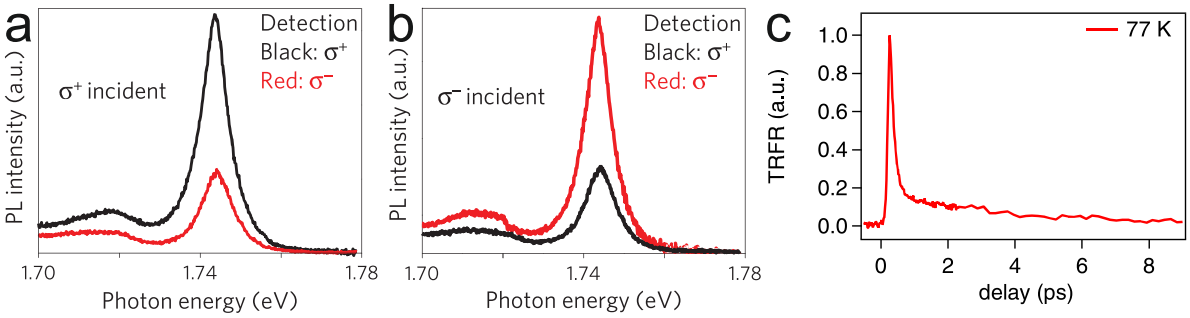

Figure 2.7 | a, **b** Polarization-resolved PL measurements on WSe_2 (adapted from [Xu14]). **c** Normalized time-resolved Faraday rotation dynamics (adapted from [Dal15]).

2.1.2 Hexagonal Boron Nitride

Hexagonal Boron Nitride (hBN) is a two-dimensional material with a layered structure in its bulk form. A monolayer of hBN crystallizes in a planar honeycomb lattice with strong covalent bonds in the layer and weak van der Waals forces between the layers. While experiments show that hBN features an indirect band gap of about 6 eV [Cas16] in this work it will be treated as an insulator. This is appropriate because all conducted experiments were carried out at far lower energies and the band alignment relative to TMDCs is such that no charge transfer to hBN occurs.

HBN is mainly used to improve the properties of other two dimensional materials. Dean et al. first found an enhancement of the mobility of graphene by hBN [Dea10]. This is accomplished via encapsulation i.e. embedding the desired material between two thin sheets of hBN. Furthermore this not only works for graphene but also encapsulating TMDCs yields improvements [Jin17]. The dominant effect is hBN working, due to its layered structure, as a perfectly flat substrate with no dangling bonds in contrast to SiO_2 which is normally used as a substrate. Additionally the hBN layers serve as a protection of the sample surface, which was further investigated in this work (see chapter 4.1).

Another improvement by hBN encapsulation is the decrease of the transition linewidth of monolayer TMDCs [Wan17, Cad17]. Substrate roughness, impurities and adsor-

bates lead to a fluctuation of the dielectric environment which influences the electron-electron and electron-hole interaction (see figure 2.8a). Because most measurements are conducted with a micrometer spot size on the sample the result is an average over a macroscopic area, compared to the exciton radius (see section 2.2). Due to the spatial fluctuations of the above mentioned interactions also the transition energies vary, which leads to an inhomogeneous broadening in the measurement [Raj19]. This is illustrated in figure 2.8b. By encapsulation these fluctuations are suppressed and therefore the linewidth is reduced, which is crucial for many experiments.

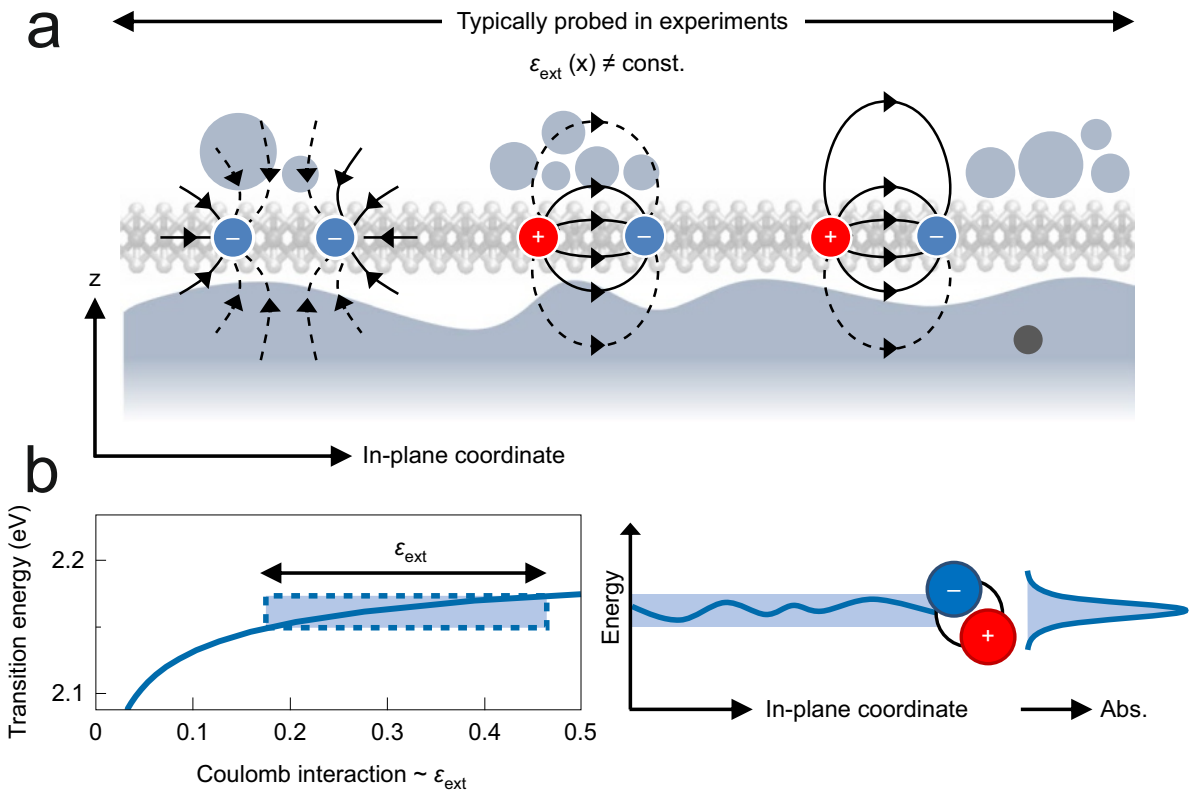

Figure 2.8 | a Illustration of the influence of a fluctuating dielectric environment $\varepsilon_{ext}(x)$ on the electron-electron and electron-hole interaction. **b** Illustration of the inhomogeneous broadening of a transition as a result of the change of the dielectric environment (adapted from [Raj19]).

All these advantages of using hBN with TMDCs lead to hBN being a standard material utilized in van der Waals heterostructures. In current research, due to its high quality, mostly hBN synthesized by T. Taniguchi and K. Watanabe is used [Tan07].

2.1.3 Niobium Diselenide

Niobium Diselenide ($NbSe_2$) is a metallic TMDC with the same crystal structure as described for the classical TMDCs (see section 2.1.1). Therefore, it is a van der Waals material and can be exfoliated down to the monolayer. In contrast to the four semiconducting TMDCs introduced in this work, $NbSe_2$ is a superconductor with a critical temperature $T_C = 7.2\,\mathrm{K}$ in its bulk form and $T_C = 1.9\,\mathrm{K}$ in the monolayer limit [Uge16]. Another difference is the stability of $NbSe_2$ under ambient conditions. While the other TMDCs are stable, $NbSe_2$ oxidizes if exposed to air [Cao15]. The oxidation is even enhanced by the exposure to light [Li19], e.g. by a laser while conducting optical experiments. This is a major obstacle when working with many two-dimensional materials and was further investigated in this work (see chapter 4.1).

2.2 Excitons

If an electron is excited from the valence band to the conduction band a hole remains in the valence band. This positively charged hole couples to the electron via the Coulomb interaction and this electron-hole pair can be treated as a quasiparticle, the exciton. There are two types of excitons namely the Frenkel exciton, which is strongly localized in the crystal lattice, and the Wannier-Mott exciton, which is delocalized over many unit cells. Excitons in TMDCs belong to the latter type and their characteristics will be described in the following.

The classification of excitons in TMDCs as Wannier-Mott excitons is justified by the measurement of the extent of the electron-hole pair. This is done by the determination of the Bohr radius via optical measurements in high magnetic fields and yields the result of a radius of $\sim 1\,\mathrm{nm}$ [Sti16, Ple16]. For Wannier excitons the energies of ground and excited states can be calculated via the effective mass approximation. This gives a modified Rydberg series for the excitonic energies in TMDCs similar to the hydrogen atom and is experimentally verified [Che14] (see Fig 2.9). Another important feature of excitons is the exciton binding energy, which is relatively high for TMDCs. The reasons for the strong coupling are the two-dimensional confinement, the relatively big effective masses and the reduced dielectric screening [Wan18]. The reduced screening can be visualized via the electric field lines of the Coulomb interaction, which are located outside of the material due to the thinness of a monolayer, and experience a lower dielectric constant surrounding the TMDC. Therefore, the energy of the optical band gap E_{PL} (see section 2.3) is not equal to the energy of the free particle bandgap E_G,

but reduced by the exciton binding energy E_X^B: $E_{PL} = E_G - E_X^B$ The binding energy is in the order of 500 meV and an overview over the binding energies of the different TMDCs on different substrates can be found in [Wan18]. Due to the two-dimensional confinement, the dipole moment of the exciton in a monolayer (intralayer exciton) lies in the layer [Sch13]. In section 2.1.1 the selection rules are discussed and as a result of the valence band splitting two energetically different excitons emerge. An electron-hole pair with the hole in the upper valence band is called A exciton and an electron-hole pair with the hole in the lower valence band B exciton.

Besides the neutral exciton, which consists of a bound electron-hole pair and was described above, other excitons exist. The trion is a neutral exciton bound to an electron or hole and the biexciton is a system consisting of two neutral excitons. These quasiparticles exhibit additional binding energies, which add to the binding energy of the neutral exciton. The binding energies of the trions and biexcitons lie in the order of the thermal energy at room temperature [Mak13] and therefore these excitons can only be measured at low temperatures. A gate-voltage-dependent differential reflectance measurement which shows the neutral exciton, positively and negatively charged trion and the first excited state of the neutral exciton is shown in Fig 2.9.

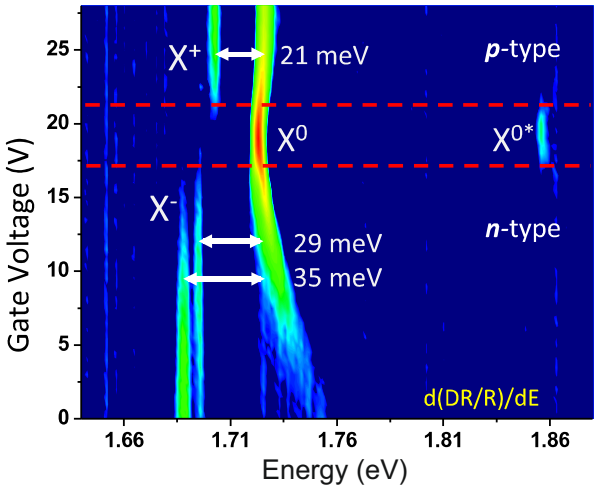

Figure 2.9 | Heatmap of the first derivative of the differential reflectivity measured on a monolayer of WSe_2 at low temperatures. A gate voltage is used to tune the Fermi level of the monolayer. The neutral exciton (X^0), negatively charged (X^-), positively charged (X^+) trion and first excited state of the neutral exciton (X^{0^*}) are marked [Cou17].

2.3 Optical spectroscopy

2.3.1 Photoluminescence spectroscopy

Photoluminescence (PL) spectroscopy is a standard tool for investigating semiconductors. A light source, usually a laser, excites an electron from the valence to the conduction band. Therefore, the energy of the incoming light has to be bigger than the optical bandgap of the material. After the excitation, a hole remains in the valence band and the hole and the electron relax via phonons to their respective band extrema. Next, they recombine radiatively by emitting a photon. This is depicted in Fig 2.10a. Due to the coupling of the electron to the hole in an excitonic quasiparticle the energy of the emitted light E_{PL} is the difference between the free particle bandgap E_G and the exciton binding energy E_X^B. The absorption and emission of light has to fulfill energy and momentum conservation. Therefore only k-space direct transitions are allowed because of the negligible momentum of the photons. As a consequence, monolayer TMDCs show bright luminescence, while multilayer TMDCs are dark owing to their indirect bandgap. This sparked the interest in TMDCs when it was first reported in 2010 [Mak10, Spl10] (see Fig 2.10b). The optical transitions in TMDC monolayers are also limited by selection rules, which are discussed in section 2.1.1.

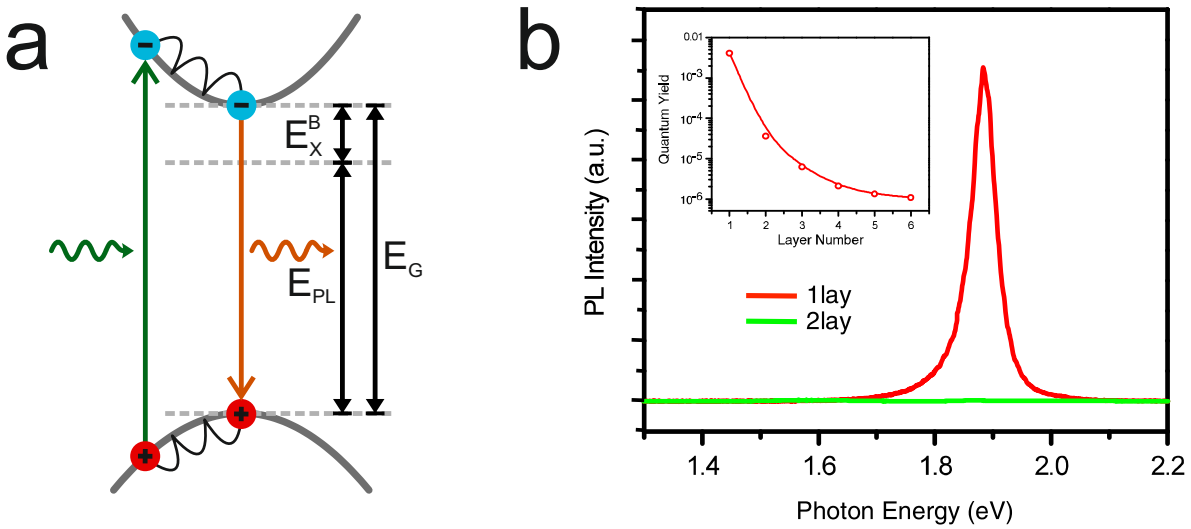

Figure 2.10 | a Schematic drawing of a photoluminescence measurement. The excitation, relaxation and emission and the important energies are shown. **b** PL spectra for mono- and bilayer MoS_2. The inset shows the dependence of the quantum yield on the layer number on a logarithmic scale [Mak10].

2.3.2 Raman Spectroscopy

Raman scattering is a widely used tool in optical spectroscopy. It utilizes inelastic light scattering to measure vibrations of molecules, electronic excitations, lattice vibrations, etc. For the measurement of phonons the sample is excited with a laser and most of the light is elastically backscattered by the Rayleigh scattering. But a part of the backscattered light is inelastically scattered allowing the creation (Stokes) or annihilation (Anti-Stokes) of a phonon (see Fig 2.11a). Therefore the energy of the phonon can be measured via the energetic shift in the spectrum (see Fig 2.11b). The energy scale of the spectrum is normally depicted as the difference to the energy of the Rayleigh scattered light in wavenumbers (cm^{-1}) with a positive sign for the Stokes side.

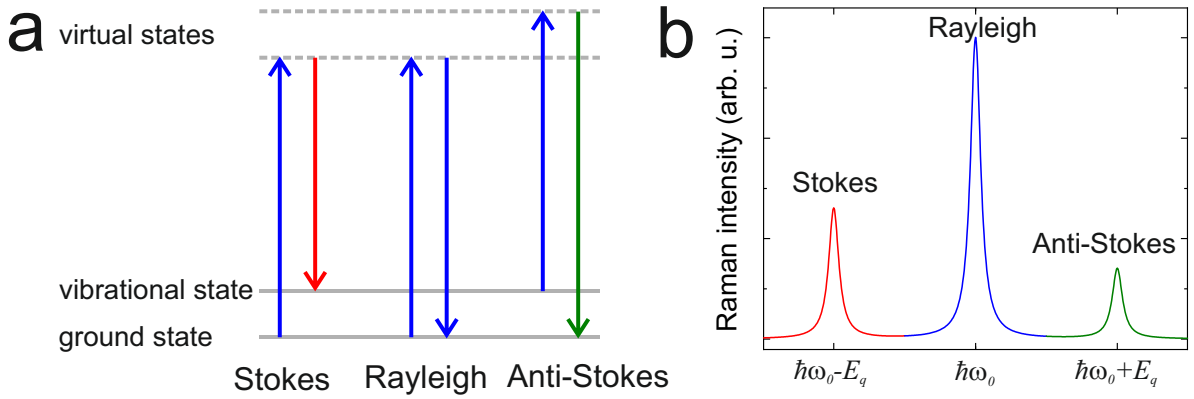

Figure 2.11 | Schematic plot **a** and spectrum **b** of light scattering. The Rayleigh scattered light has the same energy $\hbar\omega_0$ as the incoming light (blue). The Raman scattered light has either lower energy for the Stokes process (red) or higher energy for the Anti-Stokes process (green).

Raman processes must fulfill momentum and energy conservation:

$$\hbar\omega_i - \hbar\omega_s \pm E_q(\mathbf{k}) = 0$$
$$\hbar\mathbf{k}_i - \hbar\mathbf{k}_s \pm \hbar\mathbf{q} = 0$$

Here, ω_i and ω_s are the frequencies of the incoming and the scattered light and $E_q(\mathbf{k})$ is the energy of the phonon. $\mathbf{k}_i$ and $\mathbf{k}_s$ are the respective wave vectors of the light and $\hbar\mathbf{q}$ is the momentum of the phonon. So the measured spectrum (see Fig 2.11b) yields the energy of the phonon $E_q(\mathbf{k})$ [Sch06]. Due to the low wave vectors of the photon, Raman spectroscopy is mostly limited to studying optical phonons close to the Γ point of the phonon dispersion. An important exception is discussed in section 2.5.4. Moiré phonons are folded acoustic phonons and can be measured by Raman spectroscopy.

Other characteristic Raman modes, namely the interlayer shear and breathing mode, of the investigated systems will be presented in section 2.5.3.

2.3.3 Second harmonic generation

Second harmonic generation (SHG) is a nonlinear optical effect where two photons of the same wavelength get absorbed and a photon with twice the energy is emitted. In this work, SHG was used to determine the relative orientation of two monolayers, which is required for the structures described in section 2.5 and 2.6. Second harmonic generation is an interaction between an electromagnetic wave and an optically nonlinear material, whose second-order nonlinear susceptibility tensor $\chi^{(2)}$ has to be non-zero [Boy20]. Therefore, it is only possible in non inversion symmetric crystals. For TMDCs, these are the ones with odd layer number (see section 2.1.1), i.e. monolayers, trilayers, etc. To determine the crystal orientation the polarization of the light is crucial. For parallel polarization (incoming and outgoing light have the same linear polarization) the intensity of the SHG signal $I_{||}$ is dependent on the angle φ of the polarization of the incoming light with respect to the crystallographic axes of the material: $I_{||} \propto \cos^2(3\varphi)$ This angle dependency corresponds to the crystallographic orientation of the material as shown in Fig 2.12 [Mal13, Li13].

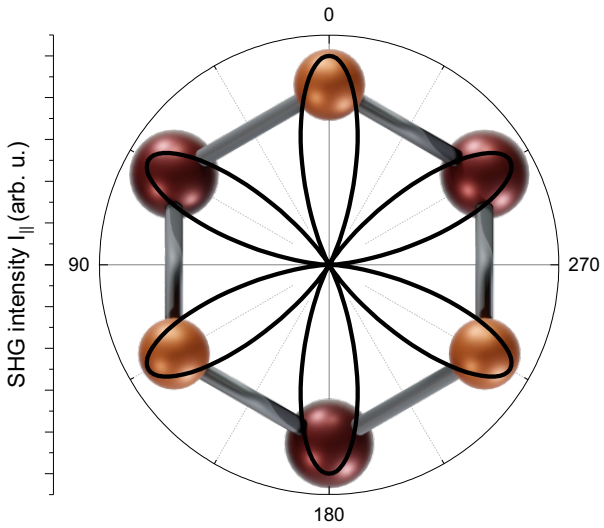

Figure 2.12 | Polarized SHG intensity $I_{||}$ of a TMDC monolayer showing the relationship between the crystallographic orientation and the intensity dependency on the polarization angle φ.

The measurement works similar with crossed polarizations (incoming and outgoing light have perpendicular linear polarization). It has to be noted, that this method can only

determine the orientation with an arbitrariness of 60°, as the monolayer features only a threefold symmetry while the SHG signal features a sixfold symmetry.

2.4 Excitons in high magnetic fields

Spectroscopy in high magnetic fields is a powerful tool for investigating TMDCs. By applying a magnetic field the time reversal symmetry is broken and the valley degeneracy is lifted. The dominating effects that are experimentally observed are an effective Zeeman splitting and a diamagnetic shift. These observations yield information about the Bohr radius [Sti16], the reduced mass and the binding energy of the exciton [Sti18, Mol19] and give experimental evidence for the Rydberg series of the exciton up to 11s [Wan20c] in TMDCs. Via a tilted magnetic field also spin-forbidden dark states could be investigated [Rob20].
Up to now, the effective Zeeman shift was explained by adding up contributions from the spin, orbital and valley magnetic moment [Aiv15]. Only recently, more precise, ab initio calculations for the effective exciton g factor were conducted [Dei20, För20, Woź20, Xua20]. In the following, the approach of Woźniak et al. [Woź20] will be outlined, who also calculated g factors for TMDC heterostructures (see section 2.6.2).
The following Hamiltonian H is used to calculate the effective g factor $g_{n\mathbf{k}}$ of a Bloch state $|n\mathbf{k}\rangle$:

$$H(\mathbf{B}) = H^0 + \mu_B \mathbf{B} \cdot \left(\mathbf{L} + \frac{g_0}{2}\mathbf{\Sigma}\right) + \frac{e_0^2}{8m_0}\left(\mathbf{B} \times \mathbf{r}\right)^2$$

Here, μ_B is the Bohr magneton, $\mathbf{B}$ the external magnetic field, $\mathbf{L}$ the angular momentum operator, g_0 the g factor of the free electron, $\mathbf{\Sigma}$ the vector of Pauli matrices, e_0 the elementary charge, m_0 the rest mass of the electron and $\mathbf{r}$ the position operator. H^0 is the nonrelativistic band structure Hamiltonian without magnetic field. The magnetic field is taken into account by adding the spin Zeeman term and replacing the momentum operator $\mathbf{p}$ by $\mathbf{p} - q\mathbf{A}$, where q is the charge of the electron and $\mathbf{A} = (\mathbf{B} \times \mathbf{r})/2$ the chosen vector potential. The equation is solved via density functional theory (DFT) by treating the magnetic field dependent terms with first order perturbation theory and choosing $\mathbf{B} = (0, 0, B)$ to be perpendicular to the sample plane. Also relativistic effects, which cannot be neglected due to the high masses of Mo and W, are taken into account. For more detailed calculations see [Woź20].
As a result the effective g factor $g_{n\mathbf{k}}$ of the Bloch state $|n\mathbf{k}\rangle$ can be calculated. This

yields the linear energetic shift $E^L_{\mathbf{k}}(B)$ of the momentum-direct exciton as

$$E^L_{\mathbf{k}}(B) = (g_{c\mathbf{k}} - g_{v\mathbf{k}})\,\mu_B B = g_{\mathbf{k}}\mu_B B,$$

where c (v) denotes the conduction (valence) band and $g_{\mathbf{k}}$ is the intravalley g factor of an exciton at $\mathbf{k}$. Bright excitons in TMDCs are at $\mathbf{k} = K^{\pm}$ and due to symmetry reasons $g_{n,K^+} = -g_{n,K^-}$ and $g_{K^+} = -g_{K^-}$ holds.
In experiment the effective g factor is measured by determining the difference of the exciton emission energies $E_{\sigma^\pm}$ with σ^+ and σ^- polarizations in a magnetic field B perpendicular to the sample (effective Zeeman splitting, see Fig 2.13):

$$E_{\sigma^+}(B) - E_{\sigma^-}(B) = g_{eff}\mu_B B$$

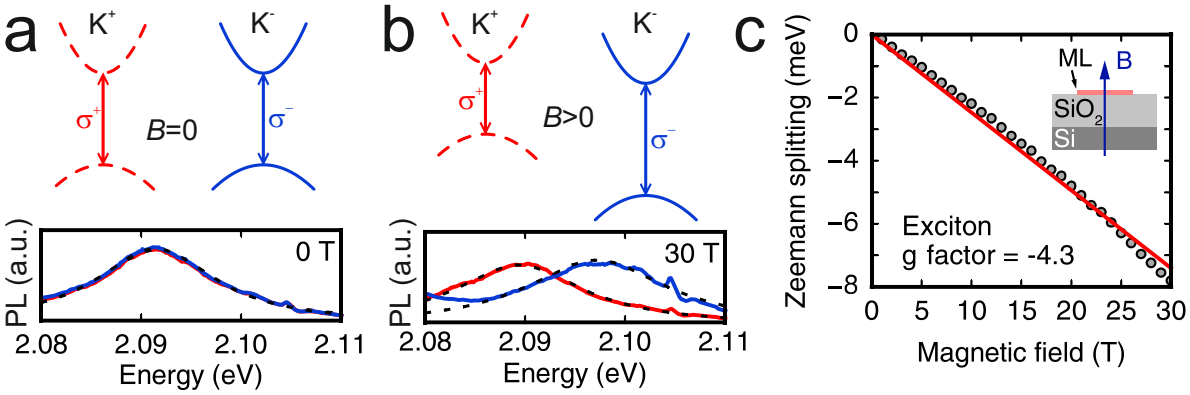

Figure 2.13 | Schematic band structure and PL measurement of WS_2 at **a** 0 T and **b** 30 T. **c** Effective Zeeman splitting obtained from PL measurements. An effective g factor $g_{eff} = -4.3$ is obtained from the linear fit (adapted from [Sch16b]).

Thus in experiment an intervalley g factor is measured, which is therefore called effective g factor g_{eff} in this work. To calculate this effective g factor g^{theo}_{eff} from the intravalley g factors obtained above, the selection rules have to be considered:

$$g^{theo}_{eff} = g_{\sigma^+} - g_{\sigma^-} = g_{K^+} - g_{K^-} = 2g_{K^+}$$

This shows a sensitive dependence of the effective g factor on the selection rules, which will be important in section 2.6.2. The effective g factor for the classical monolayer TMDC is approximately $g_{eff} \approx -4$ and theoretical and experimental results agree rea-

sonably well, as can be seen in table 2.3. Further experimental values and discrepancies to the theoretical values are discussed in [Woź20]. Due to the different energetic shifts of the valleys the distribution of the carriers changes. This leads to a magnetic field induced valley polarization even by excitation with linearly polarized light. Valley polarization is described in section 2.1.1.

	MoS_2	WS_2	$MoSe_2$	WSe_2
g_{eff}^{theo}	-3.68	-3.66	-3.82	-3.80
g_{eff}^{exp}	-4.0 [Sti16]	-3.94 [Sti16]	-4.2 [Aro19]	-3.8 [Aro19]
Intensity	28.6	42.9	21.2	33.1

Table 2.3: Calculated and experimental effective g factors of the A exciton. The given intensities are proportional to the oscillator strength (adapted from [Woź20]).

Besides the linear contribution in a magnetic field B the Hamiltonian also features a quadratic contribution. This diamagnetic shift E_{dia} can be generally described by:

$$E_{dia} = \frac{e_0^2}{8\mu^*} \left\langle r^2 \right\rangle B^2 = \beta B^2$$

Here, e_0 is the elementary charge, μ^* the reduced mass of the exciton and $\langle r^2 \rangle$ the root-mean-square radius of the exciton. Therefore, this is very useful to determine the reduced mass and extent of excitons. The diamagnetic shift is always positive. In experiment, the proportionality constant β can be measured by the mean value of the exciton emission energies $E_{\sigma^\pm}$ for circularly polarized light:

$$\frac{E_{\sigma^+}(B) + E_{\sigma^-}(B)}{2} - E_X(0) = \beta B^2$$

$E_X(0)$ is the exciton emission energy at 0 T. By taking the sum of $E_{\sigma^\pm}$ the linear contribution vanishes. β quantifies the quadratic shift and can be extracted from helicity-resolved PL experiments.

2.5 Artificially stacked bilayers

The research on TMDCs has been a booming field since the discovery of the direct bandgap in the monolayer [Mak10, Spl10]. Natural mono-, bi- and multilayers have been extensively studied and while there is still a lot to be done, the next logical step

is stacking monolayers artificially on top of each other. In this work the focus lies on artificially stacked bilayers, which can be divided into bilayers of the same material (homobilayers) and bilayers of different material (heterobilayers). While natural bilayers, exfoliated from a bulk crystal, always crystallize perfectly in H-type or R-type stacking (see section 2.1.1), the twist angle θ of artificially stacked bilayers can be tailored to an arbitrary value and therefore new physics emerge. These will be described in the following section. The discussed effects are valid for both, homobilayers and heterobilayers. Additional consequences due to the different materials in heterobilayers will be discussed in section 2.6.

2.5.1 Moiré patterns

By stacking two TMDC monolayers artificially on top of each other a twist angle θ between the layers arises, either from the inherent inaccuracy of the stacking method or from an intentional misalignment between the layers (see section 3.1). A twist angle of close to (perfect) $0°/60°$ will be denoted as R-type/H-type (perfect R-type/H-type) stacking consistent with the stacking nomenclature in bulk materials. For a twist angle $\theta \neq 0°/60°$ in the sample and assuming a rigid lattice, a moiré pattern forms [Bis11, Van14, Zha17]. This is a large-scale, periodic interference pattern between the crystal lattice of the two layers and an example for a twist angle of $\theta = 13°$ is shown in Fig 2.14. For heterostructures a moiré pattern forms even for $\theta = 0°/60°$, due to the different lattice constants of the layers [Kum15]. The D_{3h} symmetry of the monolayer reduces the relevant twist angle range to $0° \leq \theta \leq 60°$ [Hua14]. The moiré superlattice leads to novel effects like moiré phonons (see section 2.5.4), moiré excitons [Yu17, Ale19, Jin19, Sey19, Tra19] and even electronic phase transitions [Cao18, Wan20b]. Therefore, the term twistronics was coined [Car17].

The moiré pattern is described by a moiré supercell, which repeats periodically over the crystal (red outline in Fig 2.14). Due to the symmetry of the crystal lattice, the moiré period of samples with twist angle θ and $60° - \theta$ is equivalent [Moo13, Lin18]. This holds for the moiré period, but generally between 0° (R-type) and 60° (H-type) stacking has to be distinguished. The moiré period (for $0° \leq \theta \leq 30°$) is given by the lattice constant of the moiré unit cell

$$L^M_{hetero} = \frac{a_1}{\sqrt{1 + (a_1/a_2)^2 - 2 \cdot (a_1/a_2)\cos\theta}},$$

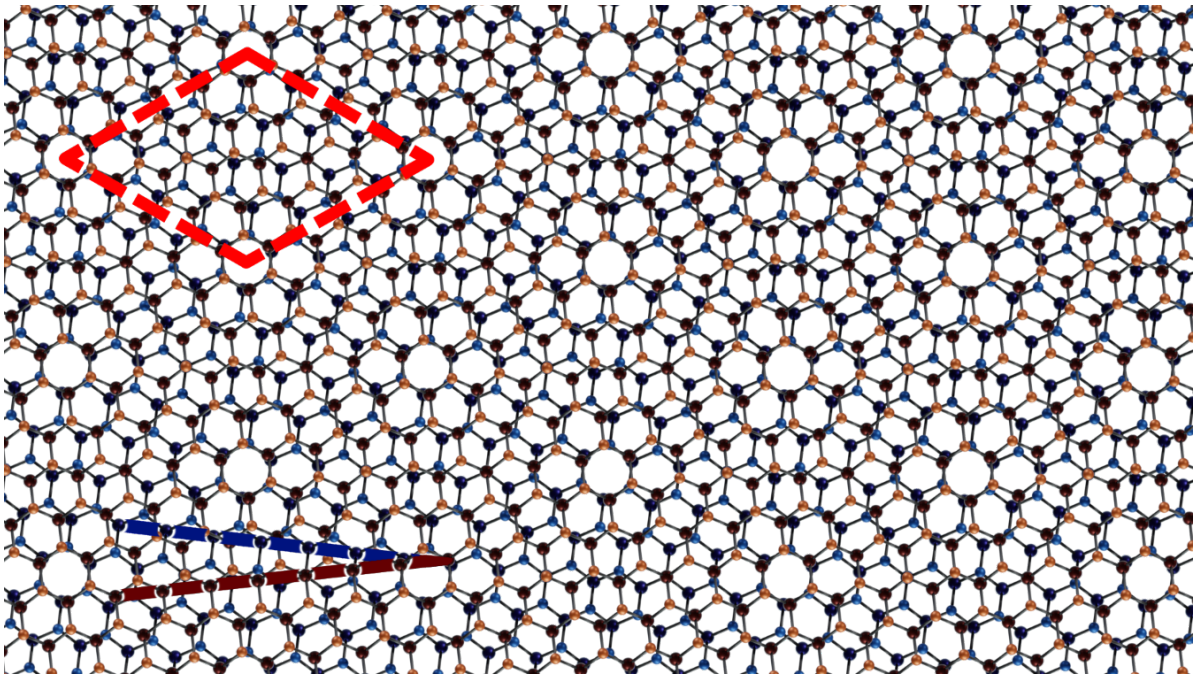

Figure 2.14 | Moiré pattern of a TMDC bilayer with a twist angle $\theta = 13°$. The moiré supercell (red dashed lines) and the twist angle θ (dark-blue/-red line) are illustrated.

where a_1 and a_2 are the lattice constants of the top and bottom monolayer [Her12]. This simplifies to

$$L^M_{homo} = \frac{a}{2\sin(\theta/2)}$$

for homobilayers with the lattice constant $a = a_1 = a_2$ [Her12]. So the size of the moiré supercell diverges for twist angles close to 0° and 60° while it is relatively constant in between. The heterostructures used in this work consist of $MoSe_2$ and WSe_2. Since the difference of their lattice constants $a_1 \approx a_2$ is negligible (see section 2.1.1) the moiré lattice can be treated like in a homobilayer sample. It has to be noted that there is also a crystallographic superlattice, which exists only for certain twist angles and has equal or bigger period than the moiré superlattice. While the crystallographic superlattice is rigorously periodic, in the moiré superlattice high symmetry points repeat [Moo13]. These will be discussed below. For this work, only the moiré superlattice is relevant. The periodic structure of the moiré pattern gives rise to a new periodicity in reciprocal space. For a twisted homobilayer with reciprocal lattice vectors $\mathbf{b_1}$ and $\mathbf{b_2}$ of the top and bottom monolayer a lattice vector for the moiré reciprocal lattice is $\mathbf{g} = \mathbf{b_2} - \mathbf{b_1}$ [Lin18]. These vectors and the corresponding Wigner-Seitz cells of the moiré lattice in

reciprocal space are illustrated in Fig 2.15. Since the moiré supercell is bigger than the unit cell of the crystal lattice in real space, the moiré supercell is smaller than the unit cell of the crystal lattice in reciprocal space.

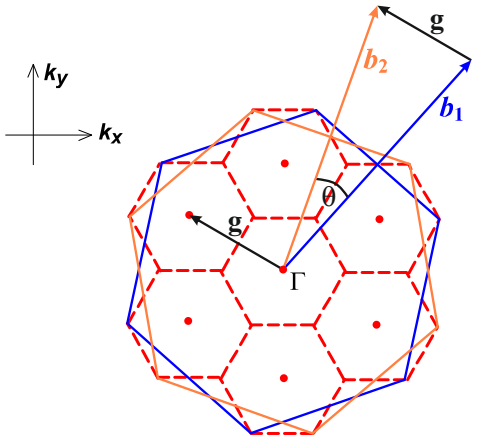

Figure 2.15 | Reciprocal space of a TMDC homobilayer with twist angle $\theta = 22°$. Reciprocal lattice vectors $\mathbf{b_1}, \mathbf{b_2}$ and the Brillouin zones (blue, orange lines) of the monolayers and the reciprocal lattice vector $\mathbf{g}$ of the moiré unit cell are depicted. The Wigner-Seitz cells of the moiré superlattice in reciprocal space (red dashed lines) and points equivalent to Γ (red dots) are marked (adapted from [Lin18]).

Within a moiré supercell several high symmetry points can be classified, which will be important in the next section. At high symmetry points the local lattice of the twisted bilayer approximates the structure of a nonrotated bilayer (perfect R-/H-type) except for a displacement of the layers [Moo13]. These stacking configurations are denoted as R^n_m and H^n_m, where R corresponds to a twist angle of $\theta = 0°$ and H to $\theta = 60°$. n (m) indicates the top (bottom) layer and substitutes the position of the monolayer lattice. X denotes a chalcogen atom site, M a metal atom site and h the hollow center of a hexagon. This notation follows the publication of Yu et al. [Yu17]. In literature, different notations are used. An overview is given in the supplementary of [Ros20]. The relevant high symmetry points H^h_h, H^M_h and H^X_h for H-type and R^h_h, R^M_h and R^X_h for R-type bilayers are depicted in Fig 2.16.
Recently, it was shown, that the moiré pattern in TMDCs changes around the high symmetry points for small twist angle deviations from 0° and 60° [Ros20, Wes20]. This will be discussed in the next section.

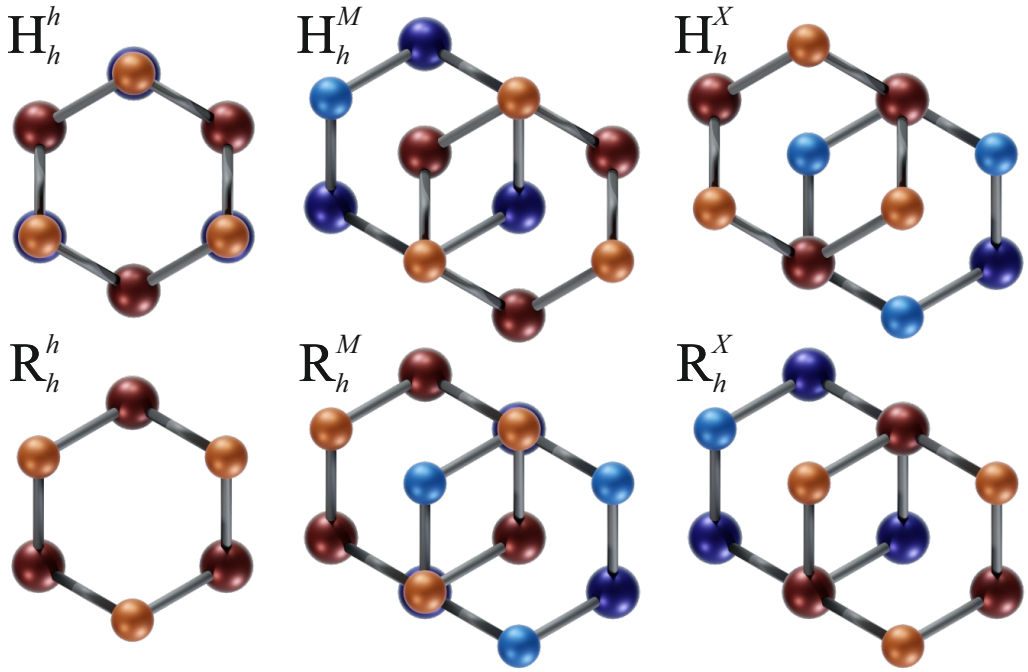

Figure 2.16 | Top view of the high symmetry stacking configurations in TMDC bilayers. The top layer is depicted in red (metal atoms) and orange (chalcogen atoms). The bottom layer is depicted in blue (metal atoms) and turquoise (chalcogen atoms). In the R_h^h-stacking configuration the bottom layer is not visible, because it is precisely underneath the top layer.

2.5.2 Atomic reconstruction

Atomic reconstruction describes the spatial rearrangement in bilayers with a twist angle close to 0° or 60°. This leads to the formation of domains, in which high symmetry stacking orders are reconstructed. It was already observed for graphene bilayers [Ald13, Yoo19], hBN bilayers [Ni19] and graphene-hBN heterobilayers [Woo14]. Carr et al. showed by calculating stacking energies, that atomic reconstruction can occur in TMDC bilayers [Car18], which was confirmed by DFT calculations [Ros20, Wes20, Woź20, Ena20] and classical modelling [Mai20]. Recent publications also confirm atomic reconstruction for TMDC homo- [Wes20] and heterobilayers [Ros20, Wes20] experimentally.

Atomic reconstruction occurs for small twist angle deviations δ from perfect R-type or H-type stacking. Here, the twist angle will be described as $\theta = 0° \pm \delta$ for R-type and $\theta = 60° \pm \delta$ for H-type structures. As discussed in section 2.5.1, moiré patterns emerge for twisted bilayers, which feature high symmetry points (depicted in Fig 2.16). The calculated stacking energies, see Fig 2.17a and d, show the energetically favourable stacking configurations [Ros20]. R_h^X and R_h^M are the energetically lowest configurations for R-type bilayers and H_h^h is the lowest for H-type bilayers. Therefore, atoms around

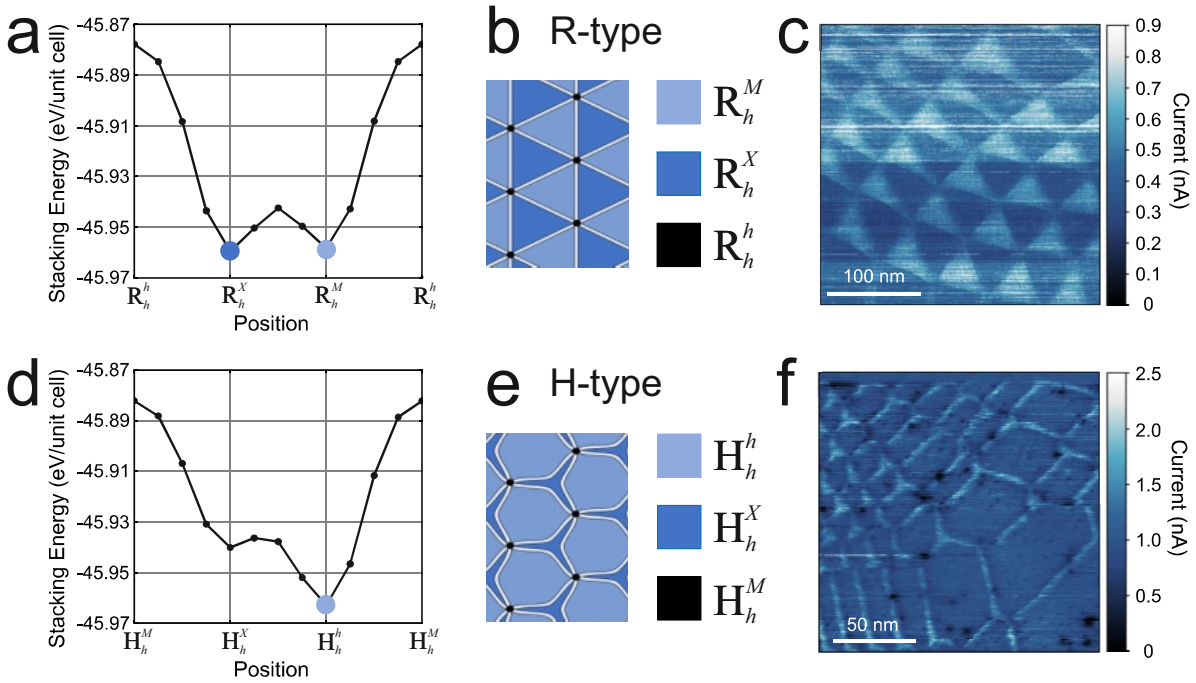

Figure 2.17 | Calculated stacking energy for different positions in the moiré lattice for **a** R-type and **d** H-type bilayers (adapted from [Ros20]). Corresponding reconstructed domains for **b** R-type and **e** H-type bilayers [Woź20]. CAFM measurements of **c** R-type ($\delta \approx 0.4°$) and **f** H-type ($\delta \approx 0.5°$) reconstructed bilayers [Ros20].

these points rearrange in the corresponding stacking order and form reconstructed domains with narrow domain walls in between. The periodicity of the high symmetry points in the moiré pattern determines the shape of the reconstructed domains. For R-type bilayers triangles with alternating R_h^X- and R_h^M-stacking form (see Fig 2.17b) and for H-type bilayers hexagons with R_h^h-stacking form (see Fig 2.17e) [Car18]. Conductive atomic force microscopy (CAFM) [Ros20] and transmission electron microscopy (TEM) [Ros20, Wes20] clearly show the reconstructed domains for R-type (CAFM shown in Fig 2.17c) and H-type stacking (CAFM shown in Fig 2.17f) and confirm the theoretical calculations. Also Raman measurements can verify atomic reconstruction, which is part of this work and shown in chapter 4.3.1 [Hol20]. The reconstructed domains are linked to the moiré lattice via the high symmetry points. Therefore, the domain size depends on the moiré period and the twist angle. For larger twist angle deviations δ from $0°/60°$ the domains get smaller and the domain walls take proportionately more space. Therefore the reconstruction is not energetically favourable any more and a moiré pattern forms. In the literature different values for when reconstruction takes place, ranging from $\delta < 1°$ [Ros20] to $\delta < 3°$ [Wes20], are given. The possible domain size ranges from 10 nm to 100 nm [Ros20]. Overall atomic reconstruction is an important aspect, that

has to be taken into account for bilayers with small twist angle deviations from 0° or 60°.

2.5.3 Rigid-layer Raman modes

As described in section 2.3.2, Raman scattering is a powerful tool to measure phonons. The Raman active modes in TMDCs are the A_{1g}, the E_{1g} and two E_{2g} modes [Ver70]. These are all intralayer modes which appear in a monolayer, but also in multilayers, where some of them are dependent on the layer number. An overview over intralayer Raman modes is given in [Sai16].
Here, the focus is on rigid-layer Raman modes in bilayers. There are two characteristic interlayer modes which only appear in multilayer but not in monolayer TMDCs. One exhibits a shearing motion between the layers (interlayer shear mode ISM) and one a breathing motion (interlayer breathing mode IBM). These modes are dependent on the layer number and are depicted for bilayers in Fig 2.18a and b. Further details for ISMs and IBMs in multilayer TMDCs are described in [Lia17].

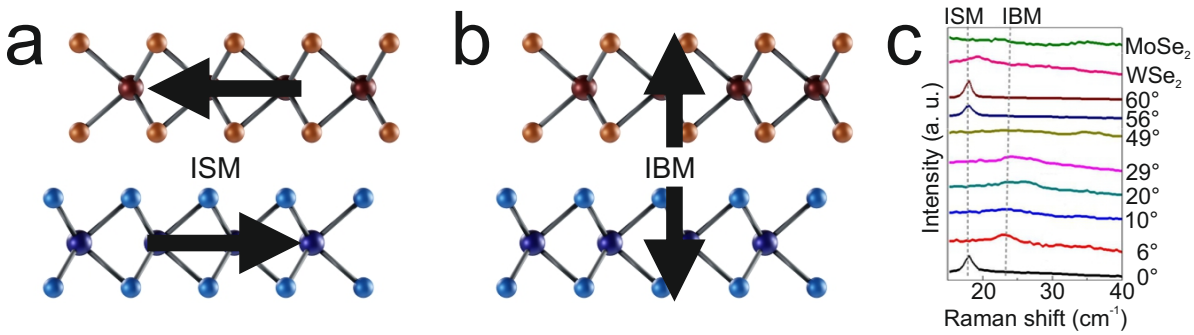

Figure 2.18 | Schematic illustration of **a** the ISM and **b** the IBM. **c** Low frequency Raman measurements in monolayer $MoSe_2$ and WSe_2 and $MoSe_2$-WSe_2 heterostructures. For monolayers no interlayer Raman modes are visible. The twist angle θ of the heterostructures is listed (adapted from [Nay17]).

The first ISM in TMDCs was measured in a natural MoS_2 multilayer by Plechinger et al. [Ple12]. Since then the ISM and IBM has been studied for all the classical TMDC materials and many more [Lia17]. For the distinction between ISM and IBM the polarization of the light can be used. In a cross-polarized setup, i.e. the sample is excited with linearly polarized light and the Raman signal is detected with a linear polarizer perpendicular to the incident laser light, only the ISM is visible. For co polarization, i.e. the sample is excited with linearly polarized light and the Raman signal is detected with a linear polarizer parallel to the incident laser light, both, ISM and IBM are

visible [Zha13b, Zha13a]. In a cross-polarized setup the Raleigh scattered laser light is additionally suppressed in contrast to a co-polarized setup.

Due to the interlayer character of the shear and breathing modes, these modes are influenced by the twist angle in artificial bilayers. The restoring force which drives the IBM is provided by the van der Waals force and therefore is only weakly dependent on the twist angle. However, the restoring force of the ISM is strongly affected by the atomic registry of the layers. For twist angles $\theta \neq 0°/60°$, where a moiré pattern forms, there is no long range atomic registry. Therefore, the ISM is strongly suppressed. Only for R- and H-type stacking the ISM is visible. This is experimentally confirmed for both, twisted homobilayers [Lui15, Pur15, Pur16, Hua16, Lin18] and heterobilayers [Lui15, Zha16, Nay17]. Fig 2.18c shows Raman spectra of the ISM and IBM for different twist angles in a $MoSe_2$-WSe_2 heterostructure. Since the effect of atomic reconstruction was only recently discovered, it was not considered in publications for interlayer Raman modes up to now. This was investigated within the scope of this work and is discussed in chapter 4.3.1.

2.5.4 Moiré phonons

The basics for this chapter are explained in section 2.5.1. Most importantly, the twist angle in a bilayer introduces a new periodicity via the moiré superlattice. Therefrom originates a backfolding of the phonon dispersion, which was already investigated for many different materials [Hol76, Tim82, Soo85, Tan04]. Lin et al. discovered folded phonons in twisted bilayer MoS_2. The following paragraph will explain the details, based on their publication [Lin18]. Since the phonon dispersion is folded by the moiré superlattice, these phonons are called moiré phonons.

Here, the folding will be explained for folded acoustic phonons in a twisted TMDC homobilayer with twist angle $\theta \neq 0°/60°$. Due to the moiré superlattice in a twisted bilayer a new periodicity emerges, which is described by the reciprocal lattice vector $\mathbf{g}$ of the moiré supercell (see section 2.5.1). In Fig 2.19a the dispersion for longitudinal acoustic (LA) and transversal acoustic (TA) phonons along $\mathbf{g}$ is shown. Due to the new periodicity (illustrated by the dashed line) the phonons at $\mathbf{g}$ can be folded back to the zone center Γ of the Brillouin zone. In Raman spectroscopy (see section 2.3.2) typically only phonons at Γ can be seen. So no acoustic phonons are visible because of their marginal Raman shift at Γ. However, the folded acoustic phonons at Γ are at higher Raman shifts and can be detected. By a variation of the twist angle θ the periodicity and therefore the energy of the folded phonon changes. The Raman shift of the folded

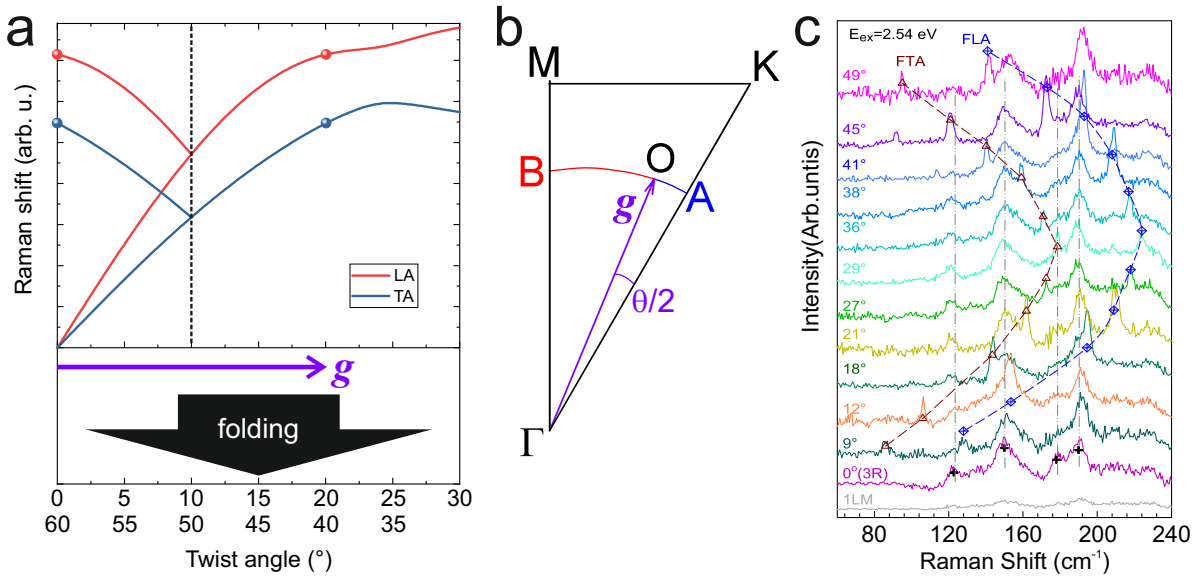

Figure 2.19 | a Phonon dispersion of longitudinal acoustic (LA) and transversal acoustic (TA) phonons along the reciprocal lattice vector **g** of the moiré supercell. The folding is illustrated for a twist angle $\theta = 20°$ and the general dependency on the twist angle $0° \leq \theta \leq 60°$ is given below (phonon dispersion calculated by B. Peng, as described in Ref [Pen16]). **b** Interpolation schematic in reciprocal space with reciprocal lattice vector **g** of the moiré supercell and corresponding twist angle θ (adapted from [Lin18]). **c** Raman measurements on twisted bilayer MoS_2 with laser energy $E_{ex} = 2.54\,\text{eV}$. The twist angles for the different samples are denoted. Folded longitudinal acoustic (FLA) phonons and folded transversal acoustic (FTA) phonons are marked (adapted from [Lin18]).

moiré phonons as a function of the twist angle is given by the moiré period in reciprocal space (see Fig 2.19a):

$$|\mathbf{g}| = \frac{8\pi}{\sqrt{3}a} \sin(\theta/2)$$

a denotes the lattice constant of the monolayer. Interlayer coupling and lattice reconstruction can lead to a frequency renormalization of the moiré phonons [Lam20, Qua21]. Therefore, the backfolding is an approximation. With varying twist angle the reciprocal lattice vector **g** of the moiré lattice changes its direction. The phonon dispersion along **g** can be calculated by the interpolation of the conventional phonon dispersion along Γ-K and Γ-M. The phonon frequency $\omega(\vec{\Gamma O})$ at the point O is given by:

$$\omega(\vec{\Gamma O}) = \omega(\mathbf{g}) = \frac{\overline{AO}}{\overline{AB}}\omega(\vec{\Gamma B}) + \frac{\overline{BO}}{\overline{AB}}\omega(\vec{\Gamma A})$$

$\left|\vec{\Gamma A}\right| = \left|\vec{\Gamma B}\right| = |\mathbf{g}|$, $\overline{AO} = |\mathbf{g}| \frac{\theta \cdot \pi}{360°}$, $\overline{BO} = |\mathbf{g}| \left(\frac{\pi}{6} - \frac{\theta \cdot \pi}{360°}\right)$ and $\overline{AB} = \frac{\pi}{6} |\mathbf{g}|$. The corresponding points in the Brillouin zone are depicted in Fig 2.19b. Fig 2.19c shows the measurement of moiré phonons on MoS_2 bilayers with varying twist angles. The moiré phonons exhibit a resonance behaviour to the C exciton and are not visible in regions of atomic reconstruction.
In this work, the moiré phonons for different materials are further investigated (see chapter 4.3.2).

2.6 Heterostructures

TMDCs and van der Waals materials in general are perfectly suitable for building heterostructures. The easy fabrication by stacking two monolayers on top of each other (see section 3.1) has lead to the comparison of van der Waals heterostructures with lego bricks (see Fig 2.20) [Gei13]. These heterostructures are an essential step for device fabrication [Nov16] and many prototypes have already been constructed [Mak16, Par20, Cho20, Hoa20]. The main advantage to other heterostructures, like quantum wells grown by molecular beam epitaxy (MBE), is that van der Waals materials do not require lattice matching. Due to the weak van der Waals forces between the layers any two-dimensional materials can be stacked onto each other and also the twist angle between the layers is arbitrary. This leads to novel effects, like moiré patterns and atomic reconstruction, which are discussed in section 2.5. The heterostructures used in this work consist of $MoSe_2$ and WSe_2, additionally hBN encapsulation was utilized. While technically the combination of hBN and a TMDC is a heterostructure, for this composition the term heterostructure will not be explicitly used in this work. HBN encapsulation is employed for its homogeneity-enhancing and protective properties and these effects are described in the materials section 2.1.2.

2.6.1 Interlayer excitons

Interlayers excitons (ILEs) are excitons (see section 2.2), where the electron is in one layer and the hole in another layer. Fang et al. [Fan14] and Rivera et al. [Riv15] first discovered ILEs in TMDCs and since then they have been investigated in many different material combinations. While in this section ILEs in heterobilayers will be described, it should be noted, that also in homobilayers [Aro17] and multilayers [Sur18] ILEs were observed.
To determine the relative offset of the band structure of two different materials, the

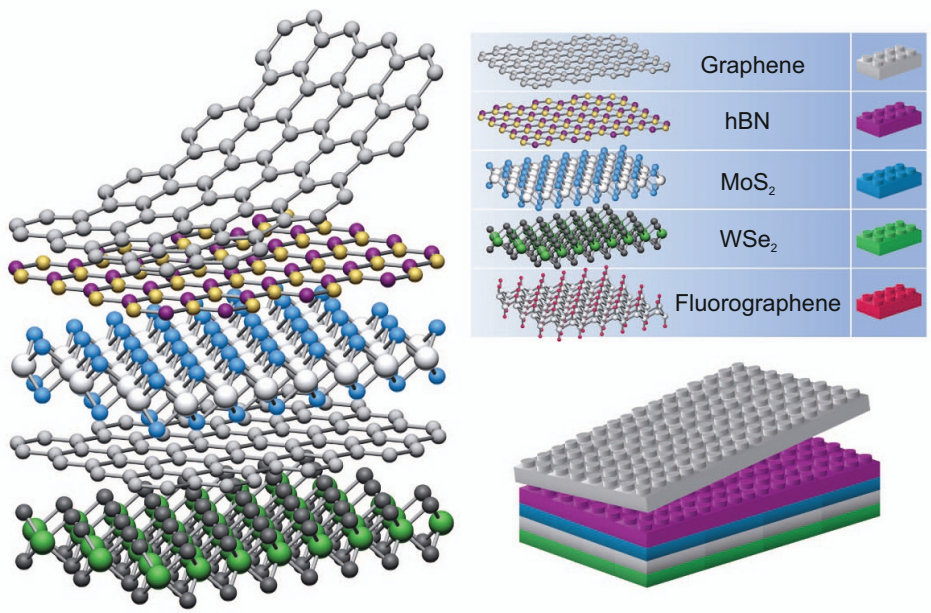

Figure 2.20 | Illustration of the fabrication possibilities for van der Waals heterostructures by comparing them to lego bricks [Gei13].

Anderson rule can be applied [And60]. This estimates the band structure by aligning the vacuum levels of the two materials and comparing their electron affinities. For most of the classical TMDCs this yields a type II band alignment [Kan13, Lia13, Wil17]. In contrast to type I and type III alignment, type II band alignment features a staggered gap, i.e. a bandgap between the valence band of one material and the conduction band of the other material. As an example the band structure for a $MoSe_2$-WSe_2 heterostructure is schematically depicted in Fig 2.21a. The electrons and holes relax to the energetically most favourable point, namely the electrons to the conduction band of $MoSe_2$ and the holes to the valence band of WSe_2. This ultrafast relaxation process happens on a timescale of a few picoseconds [Hon14, Mer19].

Due to the relaxation of the charge carriers the intralayer exciton PL is quenched, while a new feature appears in the PL spectrum at lower energies, the interlayer exciton (see Fig 2.21b and Fig 2.22b). Because of the spatial charge separation, the ILE has a dipole moment perpendicular to the sample plane and exhibits a relatively long lifetime in the nanosecond regime [Riv15, Nag17b]. Choi et al. even found a lifetime dependence on the interlayer twist angle θ [Cho21]. This can be explained by the structure of the ILE in reciprocal space. To observe the ILE optically, like it is shown in Fig 2.21b, the corresponding transition in K-space has to be direct. As illustrated in Fig 2.22a this is only the case for $\theta = 0°/60°$. Consequently, in PL measurements the ILE transition can only be observed for nearly aligned ($\theta \approx 0°/60°$) heterostructures. With increasing

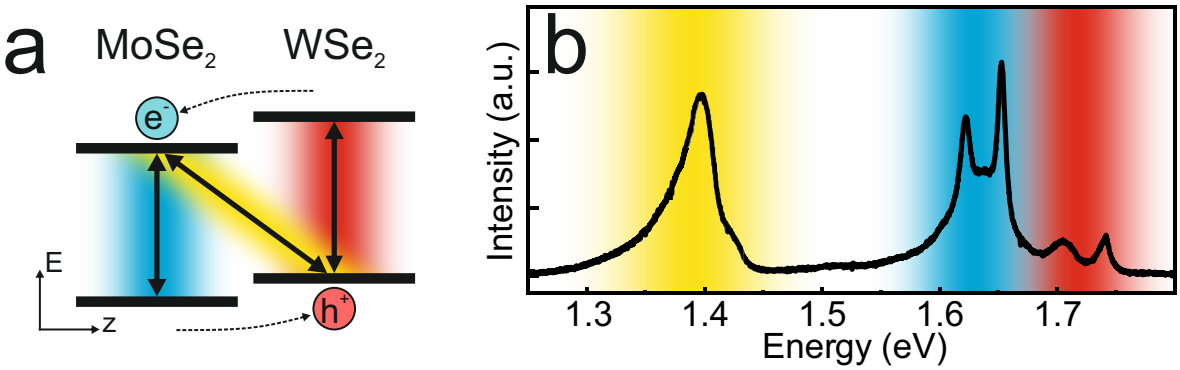

Figure 2.21 | a Schematic type II band alignment of a $MoSe_2$-WSe_2 heterostructure in real space. The intralayer $MoSe_2$ (blue), the intralayer WSe_2 (red) and the interlayer (yellow) transition is marked. **b** PL spectrum of a $MoSe_2$-WSe_2 heterostructure. The peaks are assigned to the transitions in the schematic on the left side by the corresponding colour (adapted from [Riv15]).

twist angle deviation δ from 0°/60° the ILE lifetime increases, because its transition is more and more indirect in reciprocal space. It has to be noted, that for R-type heterostructures the direct transition in reciprocal space is, similar to the monolayer, from the K^+ (K^-) valley of the valence band of one material to the K^+ (K^-) valley of the conduction band of the other material. However, for H-type structures the direct transition is from the K^+ (K^-)valley of the former to the K^- (K^+) valley of the latter. The subsequent consequences are discussed below. For misaligned heterostructures ($\delta \gtrsim 6°$) the ILE PL is strongly suppressed (see Fig 2.22b) [Nay17].

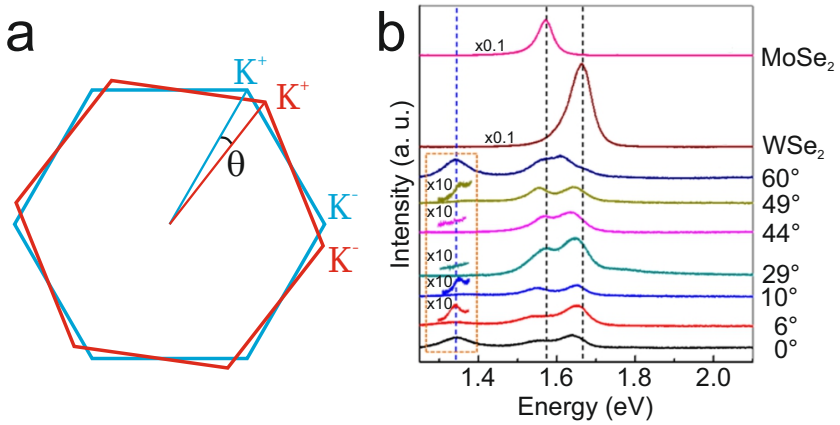

Figure 2.22 | a Twist angle dependent reciprocal space of a TMDC heterostructure with K^+ and K^- points. **b** PL spectra of $MoSe_2$, WSe_2 and $MoSe_2$-WSe_2 heterostructures with their twist angle θ listed on the right side. Scaling of individual curves is denoted. The interlayer transition (blue dashed line) and the intralayer transitions (black dashed lines) are marked. (adapted from [Nay17]).

In a MoS_2-WSe_2 heterobilayer also K-space indirect Γ-K ILE were observed [Kun18]. This is possible via room temperature measurements, where phonons can enable the indirect transition. For this material combination also the K-K direct transition could be observed at lower energies [Kar19]. Furthermore, intrinsic stacking effects, as discussed in section 2.5, have to be taken into account. On the one hand, for misaligned heterostructures a moiré pattern forms, which leads to a potential landscape in the order of 100 meV for ILEs [Yu17, Yua20]. On the other hand, for aligned structures with low twist angle deviation atomic reconstruction takes place. Therefore, for twist angle deviations $\delta < 4°$ from $0°/60°$ the heterostructure is, due to the reconstruction, perfectly aligned (perfect R-/H-type) and the corresponding transition direct in reciprocal space. The reconstruction enables the calculation of the optical selection rules. Atomic reconstruction leads to different domains (see Fig 2.17) with different lattice orientation between the layers, as described in section 2.5.2. For these high symmetry stacking domains (see Fig 2.16) the dipole selection rules were calculated for a $MoSe_2$-WSe_2 heterostructure [Woź20]. These differ substantially from the selection rules for intralayer excitons and are depicted in Fig 2.23. In contrast to intralayer transitions in monolayers, also spin-flip transitions are accessible via circularly polarized light. The corresponding transitions and relative oscillator strengths are given in table 2.4. Compared to intralayer transitions ILE have a vanishing oscillator strength [Gil18] and therefore are not seen in absorption measurements. In PL experiments the intralayer excitons are excited and after population of the ILE via ultrafast charge transfer the ILE PL can be observed.

Due to the optical selection rules different valleys can be separately addressed. In analogy to the intralayer transition in the monolayer, an interlayer valley polarization can be defined (compare to section 2.1.1). Rivera et al. measured a valley polarization of 40 % and a valley polarization lifetime of 40 ns for a $MoSe_2$-WSe_2 heterostructure [Riv16]. Remarkably, due to the dependence of selection rules on real-space crystallographic alignment, a constant valley polarization of the ILEs may manifest itself with opposite circular polarization degrees of the emitted intralayer PL, depending on the distribution of the ILEs in real space.

2.6.2 Interlayer excitons in high magnetic fields

This section is an expansion of section 2.4: "Excitons in high magnetic fields" for the ILE in $MoSe_2$-WSe_2 heterostructures. Nagler et al. reported a giant effective g factor in a $MoSe_2$-WSe_2 heterostructure, which is four times as large as the intralayer g factor

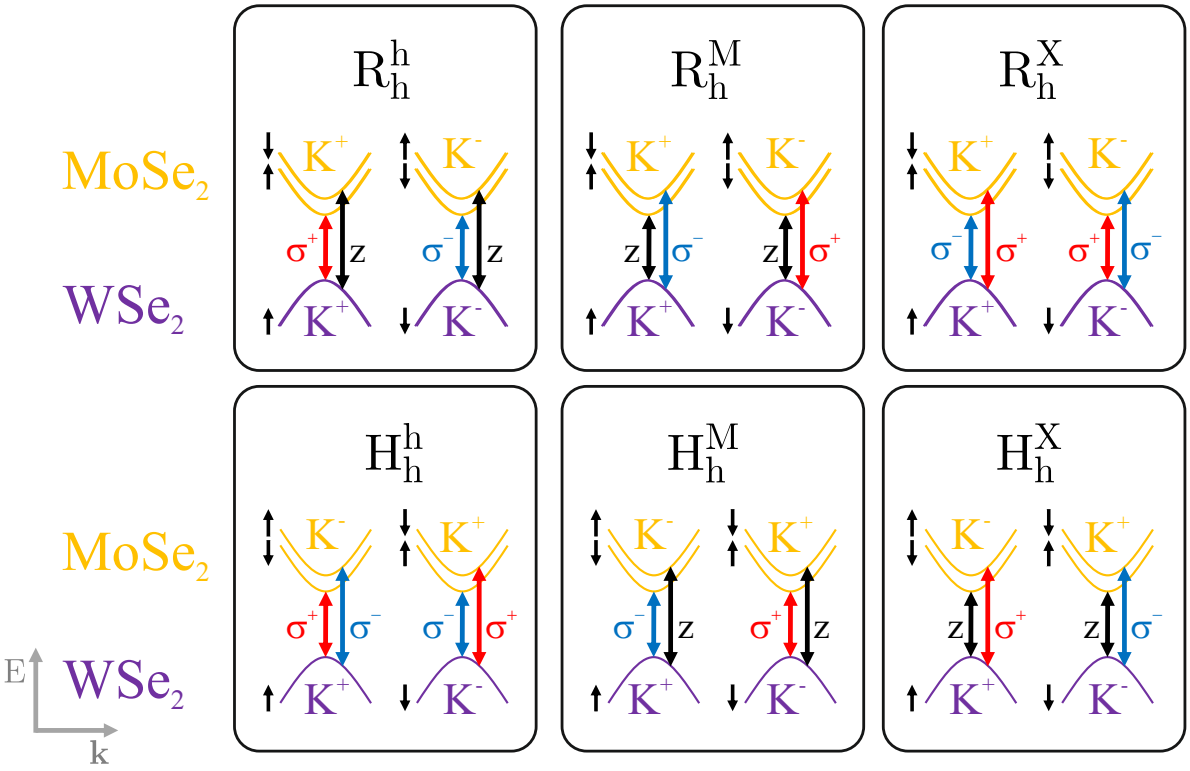

Figure 2.23 | Band structure schematic of a $MoSe_2$-WSe_2 heterostructure in reciprocal space. The electron of the ILE is located in the conduction band of $MoSe_2$ (yellow) while the hole is located in the valence band of WSe_2 (purple). The spin of a band is indicated by small black arrows. Dipole-allowed optical transitions are depicted by double arrows, corresponding to σ^+ (red), σ^- (blue) or z (black) polarized light (adapted from [Woź20]).

of the classical TMDCs [Nag17a]. To explain this, the g factor is calculated in analogy to the monolayer g factor [Woź20]. In contrast to the monolayer, in an $MoSe_2$-WSe_2 heterobilayer the intravalley transition occurs between the K^+ and the K^- valley for H-type structures. For R-type heterostructures it is always between the same valleys. Additionally the intervalley g factor, which is the effective g factor measured in experiment, depends fundamentally on the selection rules. As described in section 2.6.1 (see Fig 2.23), for $MoSe_2$-WSe_2 these selection rules differ depending on the stacking configuration substantially from the ones for intralayer excitons. Therefore, also the ILE g-factors differ depending on the high-symmetry stacking configuration of the atomic reconstruction domain from monolayer g factors. Calculated and experimental effective g factors are given in table 2.4. The experimental g factors are assigned to the corresponding transitions by the alignment of the heterostructure, the magnitude of the g factor and the intensity of the transition [Woź20].

In analogy to section 2.4 a magnetic field induced valley polarization (see section 2.6.1)

	H_h^h		H_h^M	H_h^X	R_h^h	R_h^M	R_h^X	
Trans.	v→c	v→c+1	v→c	v→c+1	v→c	v→c+1	v→c	v→c+1
g_{eff}^{theo}	-16.67	12.15	16.31	-12.60	-6.15	10.42	6.19	-10.73
g_{eff}^{exp}	-15.89 [Sey19]	10.7 [Wan20d]			-8.5 [Cia19]		6.72 [Sey19]	
	-15.1 [Nag17a]						7.1 [Cia19]	
	-15.2 [Wan20d]							
Int.	0.03	0.34	10^{-4}	0.01	0.12	10^{-7}	0.08	0.05
Spin	↑↓	↑↑	↑↓	↑↑	↑↑	↑↓	↑↑	↑↓

Table 2.4: Calculated and experimental g factors at different high symmetry configurations of a $MoSe_2$-WSe_2 heterostructure. The transition (Trans.) from the valence band (v) to the lowest (c) or second lowest (c+1) conduction band is denoted. The given intensities (Int.) are proportional to the oscillator strength. ↑↑ marks spin-conserving transitions while ↑↓ marks spin-flip transitions. Wang et al. [Wan20d] only measured $\left|g_{eff}^{exp}\right|$ (adapted from [Woź20]).

for the ILE is measured. This polarization features long lifetimes [Jia18] and for high magnetic fields near-unity values were observed [Nag17a].

Chapter 3

Methods

3.1 Sample preparation

In this section, the fabrication and preparation of the samples is described. All used crystals are van der Waals materials and their properties are explained in section 2.1. As already mentioned, the first material only consisting of one layer of atoms was graphene [Nov04]. Shortly after its discovery a multitude of two-dimensional materials have been identified [Nov05]. In this work, artificially grown bulk van der Waals materials, provided by the company *hq graphene*, were used for the sample fabrication. The hBN crystals were synthesized by T. Taniguchi and K. Watanabe (National Institute for Materials Science, Japan).

Exfoliation

The term exfoliation describes the fabrication of an atomically thin layer from bulk material. This is possible due to the weak van der Waals forces between the layers. To prepare monolayers, thin films are carefully peeled off the bulk material with nitto-tape (SPV-224PR, *Nitto Denko Corporation*). Subsequently, these thin TMDC films are partially transferred to a polydimethylsiloxane (PDMS) gel film (WF-20-X4/PF-30-X4, *Teltec GmbH*). This is possible due to the low adhesive properties of the nitto-tape. If the exfoliation was successful, a monolayer of the desired material remains on the PDMS-film. This monolayer can be identified via an optical microscope. The gel film is mounted on a glass slide.

Stamping

Exfoliated monolayers are transferred on a substrate via the stamping process. The microscope setup used for the transfer process is shown in Fig 3.1.

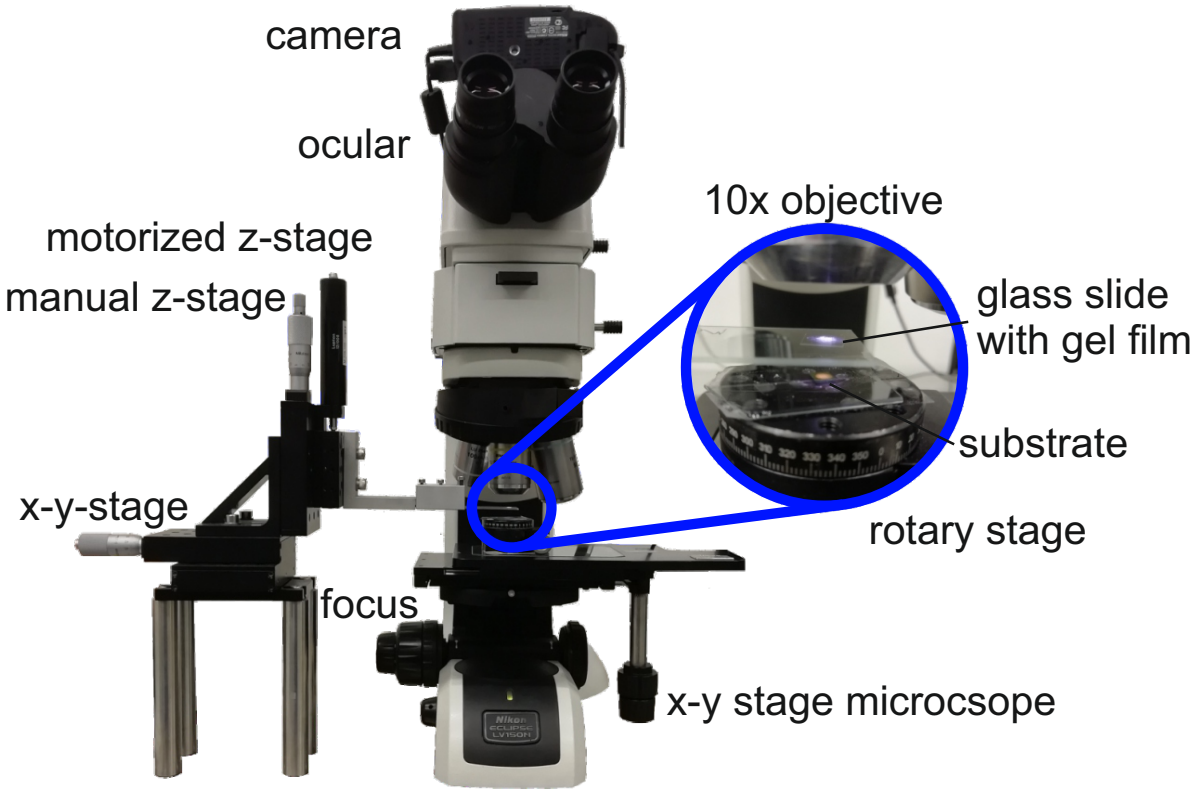

Figure 3.1 | Photograph of the microscope setup for sample transfer. All important components are denoted and the stamping constituents are magnified in the zoom.

In this work, the all-dry viscoelastic stamping developed by A. Castellanos-Gomez [CG14] was utilized. For this method, the monolayer has to be exfoliated onto a transparent PDMS film, which is described above. As a substrate 4.5 mm x 4.5 mm p^{++}-doped silicon wavers capped with a layer of 285 nm amorphous SiO_2 is used. For orientation a coordinate system consisting of gold numbers is imprinted onto the substrate via lithography. The exfoliated monolayer on the PDMS film is placed on a glass slide and mounted upside down into a x-y-z stage. The substrate is fixed onto a rotary stage mounted on the microscope. Via a tenfold amplification objective the stamping process can be monitored with the microscope (see Fig 3.1). By approaching the PDMS film carefully until contact with the substrate is established and then removing it very slowly the monolayer is transferred deterministically to the substrate. The location and orientation can be controlled precisely.

For the stamping the viscoelastic properties of the PDMS film are employed [Mei05]. For fast processes (exfoliation) the gel film behaves like a solid and the monolayer sticks to the film. For slow processes (stamping) the gel film behaves like a liquid with negligible adhesion and the monolayer transfers to the substrate.

Multilayer sample fabrication

While the basic steps are explained above there are advanced methods for the fabrication of multilayers. To produce hetero- or homobilayers the second monolayer is transferred via viscoelastic stamping on top of an already transferred monolayer. By repeating the process multiple times multilayer fabrication or hBN encapsulation can be achieved. If the alignment between the layers is of interest, prominent edges of the monolayers are used to estimate the crystallographic directions and therefore determine the twist angle of the structure [Guo16]. This can be checked additionally via SHG spectroscopy (see section 2.3.3). It has to be noted, that with this method the twist angle can only be adjusted with an arbitrariness of 60°. As the alignment of the edges is done by eye, there is always an error to consider, depending on the quality of the edges of the material.

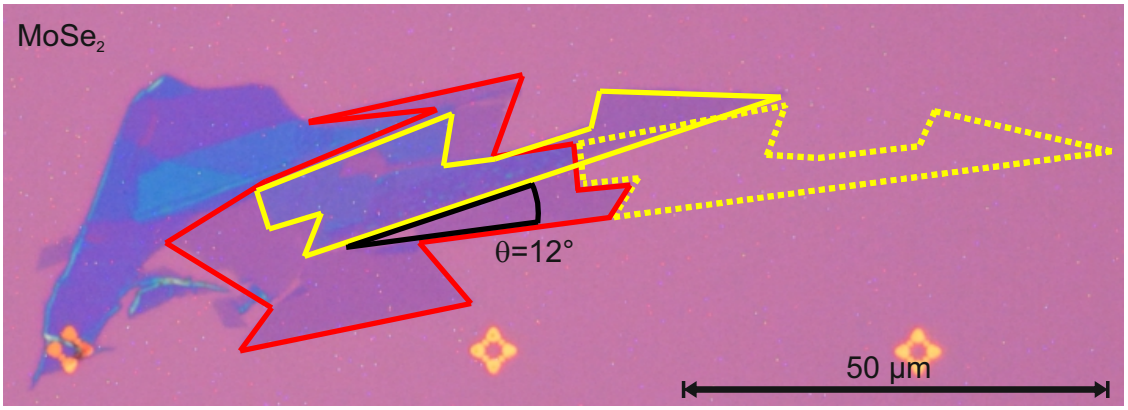

Figure 3.2 | Homobilayer $MoSe_2$ with bottom layer marked in red, top layer marked in yellow and its twist angle θ. The yellow dotted line shows the initial position of the top layer before tearing.

For stacking monolayers with a precise twist angle on top of each other, a variant of the method by Kim et al. [Kim16] is used, which will be called tear and stack method. This method utilizes the viscoelastic properties of the gel film and works for the fabrication of twisted homobilayers. When the first monolayer is halfway transferred the PDMS film is moved upwards abruptly. Thereby, the monolayer is torn apart and the remaining part on the PDMS film is used as the second monolayer as shown in Fig 3.2. The advantage

of the method is the precise control over the twist angle of the homobilayer, as the orientation between the layers is always exactly known.

Two heterostructure samples were fabricated similar to the tear and stack method. For these a monolayer $MoSe_2$ is transferred on a substrate (see Fig 3.3a). Subsequently, a monolayer WSe_2 is halfway stamped onto it, aligning the cleaved edges (see Fig 3.3b). The WSe_2 monolayer is then torn apart, twisted by 60° and the remaining part is transferred onto the $MoSe_2$ monolayer. Therefore, despite the arbitrariness of 60°, the produced heterostructure has an H-type (60° twist angle) and a R-type (0° twist angle) region. The finished sample is shown in Fig 3.3c.

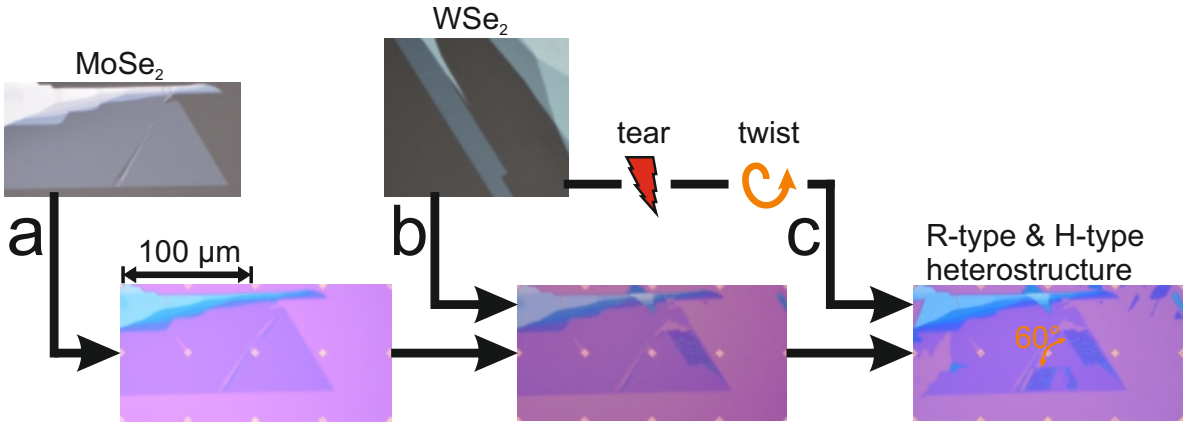

Figure 3.3 | a Monolayer $MoSe_2$ on PDMS film and transferred onto the substrate. **b** Monolayer WSe_2 on PDMS film and partly transferred onto the monolayer $MoSe_2$. The remaining part of the monolayer WSe_2 is torn, twisted by 60° and transferred onto the monolayer $MoSe_2$. **c** The finished R-type and H-type $MoSe_2$-WSe_2 heterostructure is shown. The scale bar applies to all pictures. Different colours are due to different illumination.

Most of the multilayer samples were annealed at 400 K for at least 1 h. Because of the fabrication in ambient atmosphere adsorbates adhere to the monolayer surfaces [Pür19]. The annealing leads to the formation of bubbles all over the sample. Therefore, the adsorbates accumulate into these bubbles and in between good contact of the two layers is established. These spots can be accessed via the μm spot size of the experimental setup, which is described in the next section.

The physics department of the university of Regensburg promotes collaboration and exchange in current research. As a consequence of fruitful cooperations, some of the samples used in this work were fabricated by my colleagues M. Kempf, P. Nagler, P. Parzefall, M. Scheuck, K. Lin, J. Bauer and L. Bauriedl.

3.2 Experimental setup and methods

3.2.1 Experimental setup

The experimental setup, in which the Raman and PL experiments were conducted, is shown in Fig 3.4.

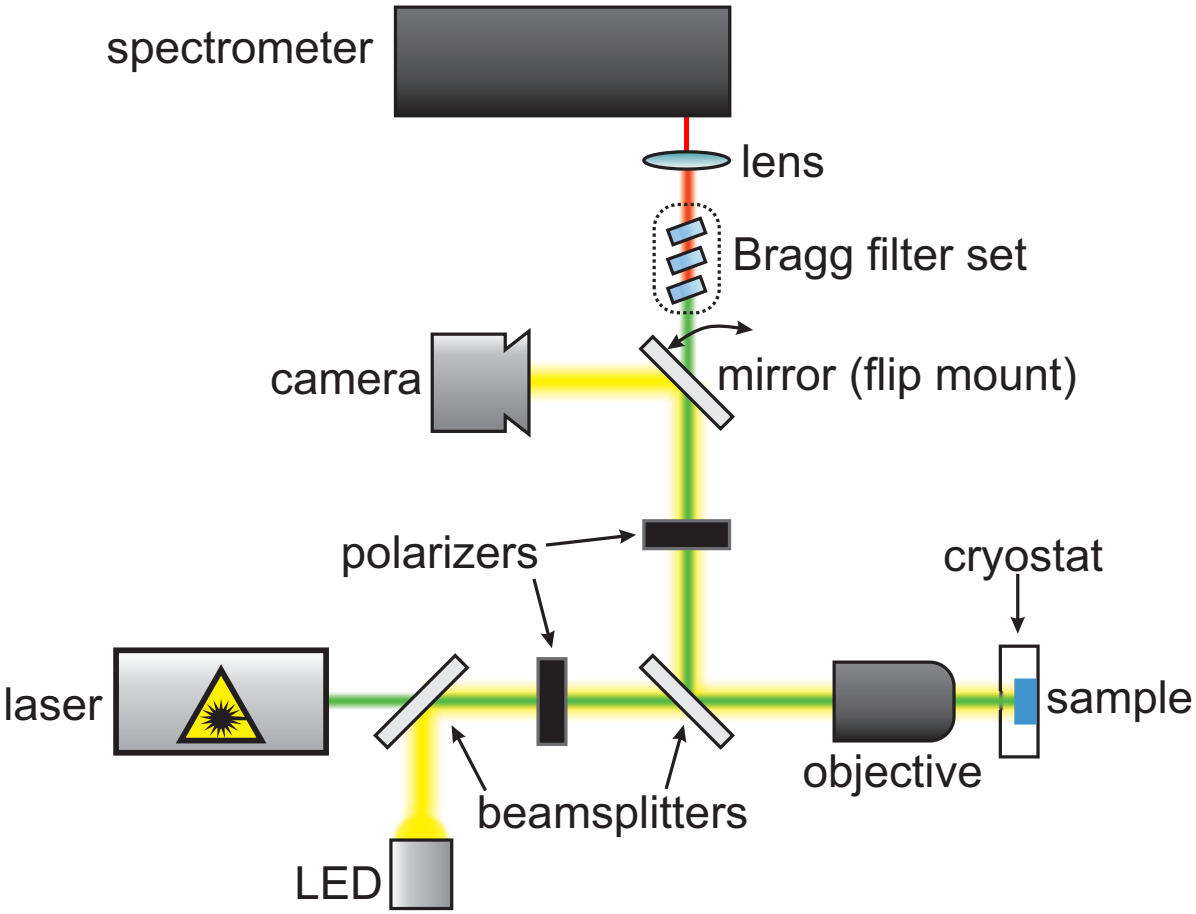

Figure 3.4 | Schematic of the experimental setup.

As an excitation source, a diode-pumped, continuous wave laser with a wavelength of 532 nm is used. The laser beam is focused via a 100x objective (*Nikon* Plan SLWD, NA 0.7) onto the sample with an estimated spot size of $\sim 1\,\mu m^2$. The sample is mounted on an automated x-y stage with a step size of ~ 100 nm. Optionally, a cryostat (*CryoVac GmbH* KONTI) can be integrated into the setup. This allows to cool the sample to a nominal temperature of 4 K. The backscattered laser light is filtered via a set of Bragg filters (*OptiGrate* BNF-532-OD3-11M). Alternatively it can also be filtered by a longpass filter. Afterwards, the light is collimated by a lens and focused into the spectrometer (*Teledyne Princeton Instruments* Acton SP 2750). The spectrometer features three

gratings with 150 grooves/mm, 600 grooves/mm and 1800 grooves/mm. For detection a back-illuminated, Peltier-cooled charge-coupled device (CCD) (*Teledyne Princeton Instruments* 100BR eXcelon) is used.
To get optical access and determine the measurement spot on the sample a light emitting diode (LED) and a camera are integrated into the beam path. The polarization of the light can be adjusted for excitation and detection via the polarizers marked in Fig 3.4. For circular polarization a linear polarizer and a quarter-wave plate are utilized. For linear polarization only the former is used.

3.2.2 Experimental methods

The theory for every experimental method is explained in section 2.3 and the experimental setup for optical measurements is described in section 3.2.1. Here, the important details and variations for the experimental methods are specified. To give a complete overview over every method, a few points may be redundant to the above mentioned sections.
For all optical experiments a CCD camera is used to detect the signal. Especially for long integration times, there is a high probability for cosmic rays to saturate a few random pixels on the CCD. Those were removed from the spectra by hand and appear as gaps in the measurement curves.

Photoluminescence spectroscopy

The conducted PL measurements are all measured with a continuous wave laser with a wavelength of 532 nm at low temperatures, i.e. nominally 4 K. Optionally, circular polarization in excitation and detection can be applied, which will be denoted as $\sigma^{\pm}$. For easier handling, the elastically scattered laser light is usually filtered by a longpass filter and not by the Bragg filters. While all PL experiments are preformed with the 150 grooves/mm grating of the spectrometer, the integration time of the CCD and the laser power are adjusted to the particular measurement.
In the setup in Regensburg automated PL scans over a sample are possible. For this, PL spectra over the desired area are recorded and fitted by a Gaussian fit via a LabVIEW application. The intensity, full width at half maximum (FWHM) and the peak position are extracted and can be plotted as a two-dimensional real-space map of the sample.
Photoluminescence experiments were also conducted at the High Field Magnet Laboratory in Nijmegen. The details are described in section 3.3.

Raman spectroscopy

For the Raman measurements, like in the PL experiments, a continuous wave laser with a wavelength of 532 nm is used. Additionally, a bandpass is utilized to filter secondary modes of the laser and the elastically scattered light is filtered by a Bragg filter set. For the measurement of the interlayer shear mode, a cross-polarized setup is used, i.e. the sample is excited with linearly polarized light and the Raman signal is detected with a linear polarizer perpendicular to the incident laser light (see section 2.5.3). All other Raman experiments are conducted in an unpolarized setup, i.e. there is no analysing polarizer in the beam path and all Raman active modes are visible. For a better resolution the 1800 grooves/mm grating is used and all measurements are performed at room temperature. The integration time of the CCD and the laser power are adjusted to the particular measurement.

Second harmonic generation

In this work, second harmonic generation measurements are used to determine the crystallographic directions of the sample (see section 2.3.3). All SHG measurements were conducted by Michael Kempf and Philipp Parzefall. The experimental setup is similar to the Raman setup. For excitation a pulsed titanium:sapphire laser with a wavelength of 800 nm, 100 fs pulses and a repetition rate of 80 MHz is used. To measure the parallel polarized intensity a linear polarizer is used for excitation and detection. The angular dependency is measured via a rotatable half-wave plate between the sample and the linear polarizer.

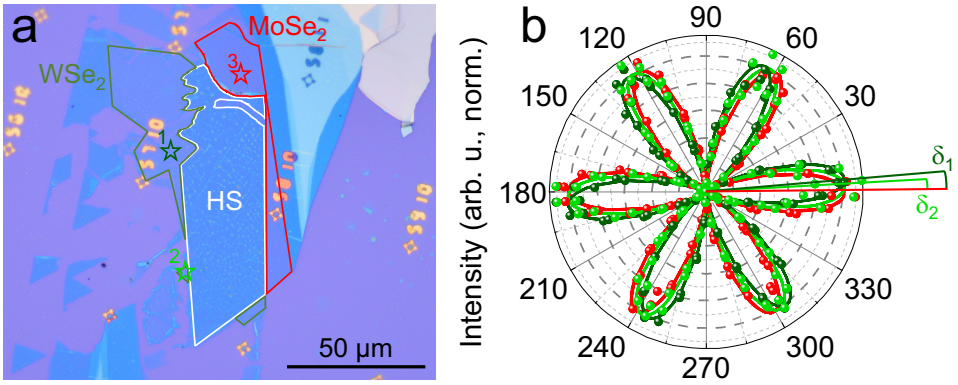

Figure 3.5 | a Microscope image of a $MoSe_2$-WSe_2 heterostructure (HS). SHG measurement spots are marked by stars. **b** Angle-resolved SHG intensities of the corresponding spots in **a**. The twist angle is extracted by fitting the experimental data.

The error of an SHG measurement consists of the instrumental error, the fitting error and the error from a possible intrinsic twist of the measured monolayer. The intrinsic twist of a WSe_2 monolayer on a $MoSe_2$ monolayer is illustrated in Fig 3.5. It shows, that two different measurement spots (1, 2) yield different twist angle deviations δ_1 and δ_2 with respect to the $MoSe_2$ monolayer (3). Therefore, the error for the twist angle determined by SHG cannot be neglected and will always be denoted. Typical errors are in the range of $\pm 2°$. A detailed error analysis of the conducted SHG measurements can be found in the master thesis of Philipp Parzefall [Par21a].

3.3 Experimental setup at the High Field Magnet Laboratory in Nijmegen

The measurements in high magnetic fields were conducted at the High Field Magnet Laboratory (HFML) in Nijmegen (Netherlands). The facility belongs to the European Field Magnet Laboratory (EFML) and features multiple magnet systems with fields up to 37.5 T.

Constant high magnetic fields are enabled by a Bitter magnet. The core element consists of a resistive electro magnet and is depicted in Fig 3.6. For optical experiments the used magnet features a wide bore of 50 mm. Electric currents in the order of 20 kA and a corresponding power consumption of 17 MW allow maximum fields of up to 30 T. Due to its resistive nature, the coils of the magnet have to be cooled. This is possible via water cooling through holes in the conducting plates (see Fig 3.6a). Two high pressure pumps ensure a constant water flow with a flow rate of 140 l/s. Nevertheless, at high magnetic fields the magnet can only be operated for a limited time.

The sample is mounted in a bath cryostat and cooled via helium exchange gas to a temperature of 4 K. The cryostat, which can be seen in Fig 3.6b, is installed in the 50 mm bore of the magnet and features a built-in 40x objective with a spot size of $\sim 4\,\mu$m and a piezoelectrically controlled x-y-z stage. All measurements in this work were conducted with the magnetic field perpendicular to the sample plane (Faraday geometry).

The optical setup is one floor above the magnet and analogue to the setup described in section 3.2.1. Via an approximately 5 m long beam path between the floors the sample can be optically accessed. As an excitation source a 640 nm diode laser is used in continuous wave mode. For time-resolved PL measurements in high magnetic fields the setup is further modified. The laser diode is operated in pulsed mode with a repetition

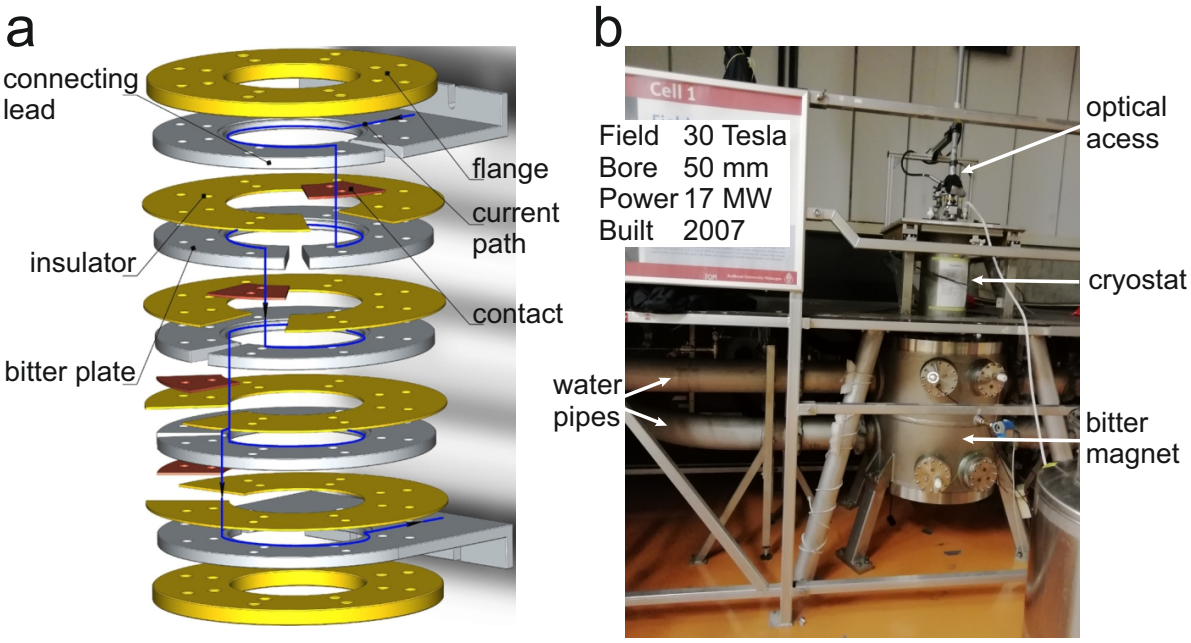

Figure 3.6 | a Schematic of a Bitter magnet (adapted from [Zai14]). **b** Picture of the magnet.

rate of 1 MHz, a pulse length of 90 ps and a wavelength of 640 nm. The signal is filtered by a suitable bandpass and detected by an avalanche photodiode (APD).

Chapter 4

Experimental results

4.1 Air tightness of hBN encapsulation

For many van der Waals structures stability in ambient conditions is crucial, especially for prototypes and future devices. Oxidation of unstable materials in air limits the research possibilities [Gei13, Cao15, Fav15, Ye16, Sun17]. Light, e.g. a laser beam, even enhances the oxidation effect [Li19]. Typically, hBN encapsulation (see section 2.1.2) is used to protect the sample surface and suppress oxidation.

In this thesis the air tightness of hBN encapsulation was systematically investigated and the results are published in [Hol19]. We find that full encapsulation, i.e. embedding the van der Waals material between two thin sheets of hBN, is air tight and prevents oxidation. However, half-encapsulation, i.e. capping the sample only with hBN from the top, in combination with the commonly used SiO_2 substrates is not air tight. The material degrades over time, especially when exposed to light.

For probing the sample degradation experimentally $NbSe_2$ was used. This superconducting TMDC oxidizes in air and is therefore suitable for the measurements. Its properties are further described in section 2.1.3. The samples were produced by L. Bauriedl applying the pick up method [Wan13, Zom14]. As a substrate p^{++}-doped silicon wafers with 285 nm SiO_2 on top were used. Fig 4.1 shows bilayer $NbSe_2$ partly covered by hBN before and after the illumination with laser light on the spots A, B and C. The sample was exposed to a laser beam with a wavelength of 532 nm, a spot size of approximately $1\,\mu m^2$ and a power of $8\,\mu W$ for 10 s. This exposure is not sufficient to conduct Raman measurements. Nevertheless, in the microscope image taken after the illumination (Fig 4.1b) a degradation can clearly be seen on all measurement spots. We attribute this to oxidation. The complementary atomic force microscopy (AFM) picture (Fig 4.1c)

indicates no thickness alteration of the spots A and B on the bare $NbSe_2$. On the hBN covered spot C a bulge appears in the topography. Therefore, the light-induced oxidation of $NbSe_2$ under ambient conditions is verified, even if it is covered by hBN.

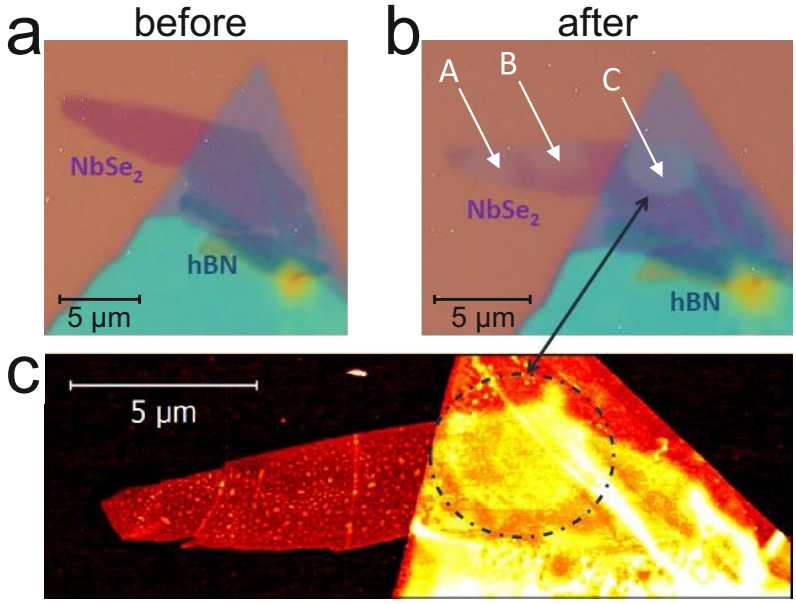

Figure 4.1 | Microscope image of a bilayer $NbSe_2$ partly covered by hBN **a** before and **b** after the illumination with laser light on the spots A, B and C. The sample was exposed to a laser beam with a wavelength of 532 nm, a spot size of approximately 1 μm^2 and a power of 8 μW for 10 s. **c** AFM image of the sample after the illumination with laser light.

Protecting TMDCs with a thin film of hBN on the top of the sample is a commonly employed technique [Xi16, Par19]. As the measurements shown above indicate, half-encapsulation is not sufficient. For a systematic comparison, two samples, one fully encapsulated and one half-encapsulated, are first measured in vacuum, where no oxidation occurs. While preventing oxidation by a vacuum environment is an apparent solution that is commonly utilized [Xi15, He16], it is not always suitable, especially when thinking of devices. After the first measurement, Raman measurements are repeatedly conducted over time. By tracking the intensity of the A_{1g} and the E^1_{2g} modes any sample degradation is monitored. For every measurement an integration time of 300 s and a laser with a wavelength of 532 nm, a spot size of approximately 1 μm^2 and a power of 2.5 mW was used.

A microscope picture of the first investigated sample is shown in Fig 4.2a. It shows a few-layer $NbSe_2$ flake fully-encapsulated in hBN. The encapsulation is illustrated in the schematic image Fig 4.2b. Fig 4.2c shows the first Raman measurement in vacuum and three consecutive measurements immediately after venting. There is a slight decrease of the intensity of the Raman modes between the measurement in vacuum and the

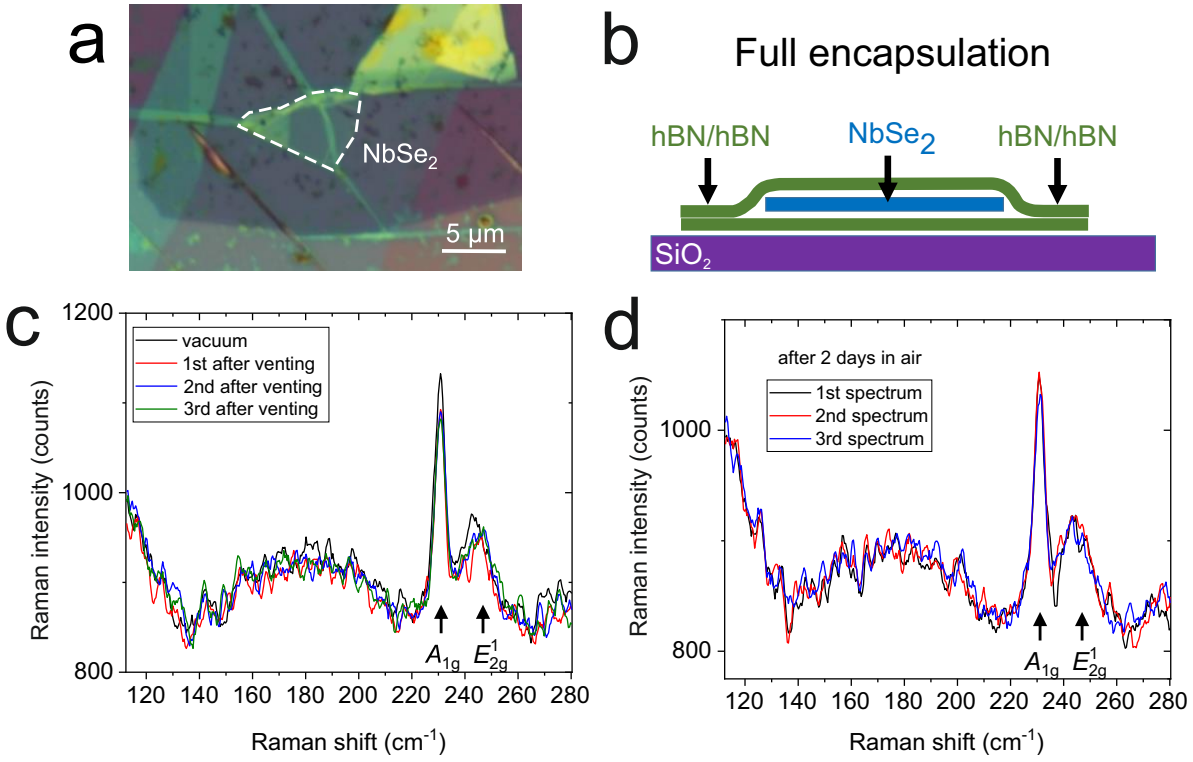

Figure 4.2 | a Microscope image and **b** schematic sketch of the few-layer $NbSe_2$ sample fully-encapsulated in hBN. **c** Raman spectra of the A_{1g} and the E^1_{2g} mode in vacuum and immediately after venting the chamber. **d** Raman spectra of the A_{1g} and the E^1_{2g} mode after two days in air. No significant oxidation is observed.

ones in ambient conditions. We attribute this to an imperfect refocusing after venting the vacuum chamber. After two days in air, the sample is measured again, which is shown in Fig 4.2d. Here, also no decrease of the amplitude of the Raman peaks can be determined. Additional measurements after three weeks reproduce this spectra without any decrease in intensity. Therefore, we conclude that full encapsulation in hBN is air tight and prevents oxidation.

The second sample is a half-encapsulated few-layer $NbSe_2$ flake. Microscope pictures before and after the measurements are shown in Fig 4.3a and a schematic image is depicted in Fig 4.3b. As shown in Fig 4.3c the Raman modes indicate no significant decrease for the first measurements after venting with respect to the measurement in vacuum. Only the third measurement shows a slight decrease. After two days in air, every consecutive measurement exhibits a substantial decrease of the Raman intensity. Therefore, we conclude, that half encapsulation is not sufficiently air tight and the material degrades by oxidation. This can also be seen in the microscope image after the measurements (Fig 4.3a). Due to the roughness of the SiO_2 oxygen molecules diffuse

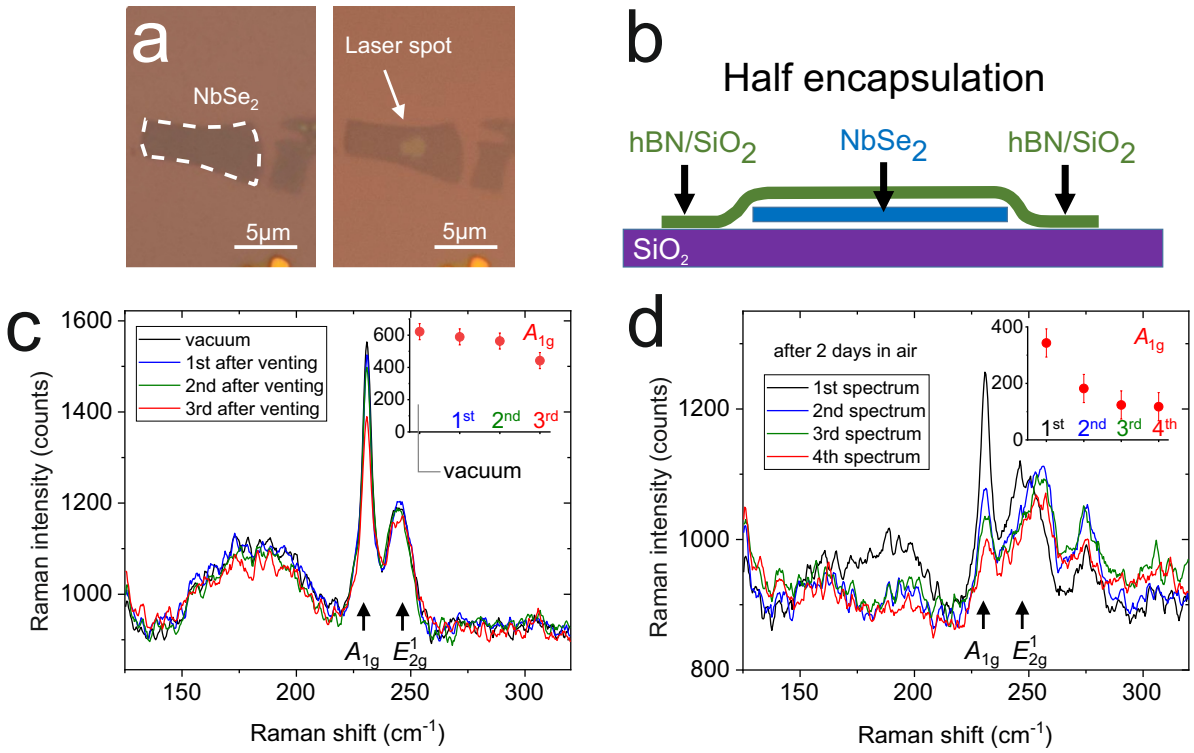

Figure 4.3 | a Microscope image of the few-layer $NbSe_2$ sample half-encapsulated in hBN before (left) and after (right) the measurements. The edges of the top hBN flake lie outside the picture frame. **b** Schematic picture of the sample. **c** Raman spectra of the A_{1g} and the E^1_{2g} mode in vacuum and immediately after venting the chamber. **d** Raman spectra of the A_{1g} and the E^1_{2g} mode after two days in air. The insets show the intensity of the A_{1g} mode.

slowly in between the SiO_2-hBN interface and the sample oxidizes. For a sufficient protection in ambient conditions samples should be fully-encapsulated or always be kept in an oxygen free environment.

4.2 Interlayer excitons in high magnetic fields

The basics of interlayer excitons in the presence of magnetic fields are explained in section 2.6.2. For the experiments in high magnetic fields several $MoSe_2$-WSe_2 heterostructures were fabricated by M. Kempf and myself. Additionally, four of them were encapsulated in hBN. For PL measurements only aligned heterostructures are suitable because for misaligned structures the ILE transition is momentum forbidden. Therefore, all the samples feature small twist angle deviations from 0°/60° and undergo atomic reconstruction (see section 2.5.2).

We find characteristic ILE emission peaks for R- and H-type heterobilayers. Thus, we can distinguish between the two stacking orientations by energetic position, spectral

linewidth and g factor of the interlayer transition. Additionally, we report a negative magnetic quadratic shift for an energetically higher-lying ILE in R-type structures. At the end of this chapter, the temporal dynamics of the ILE valley polarization in magnetic fields are discussed.

The studied R- and H-type heterostructures are also investigated by Raman spectroscopy, which is presented in section 4.3.1. The results of the PL and Raman measurements complement each other. All experiments in magnetic fields were conducted at the High Field Magnet Laboratory in Nijmegen (see section 3.3). A continuous wave laser with a wavelength of 640 nm, a laser power ranging from 50 μW to 200 μW and an integration time ranging from 0.5 s to 30 s was used. The laser power and integration time are adjusted based on the signal quality. Experimental details for time-resolved measurements are given in section 4.2.4. The results will be published in [Hol21a] and [Hol21b].

4.2.1 Characterization of H- and R-type interlayer excitons

For aligned $MoSe_2$-WSe_2 heterostructures with good contact between the layers an interlayer exciton can be measured. Its emission is at a lower energy than the intralayer excitons and it can only be detected in the heterostructure part of the samples and not on the monolayers. We observe two different interlayer exciton spectra. Fig 4.4a shows one spectrum, where a pronounced ILE emission is measured at about 1400 meV. We denote this ILE-1. On the contrary, Fig 4.4b shows a spectrum with two emission peaks at about 1360 meV (ILE-2) and 1450 meV (ILE-3). All ILE peaks reveal a blueshift with increasing excitation density. This can be explained by the repulsive dipole-dipole interaction between the aligned dipole moments of the ILEs and is a clear signature for the interlayer character [Riv15, Nag17b, Mil17]. The spectral linewidth of ILE-1 is always significantly smaller than the one of ILE-2 and the peak intensity of ILE-3 is smaller than the intensity of ILE-1 and ILE-2. On every sample we either observe ILE-1 or ILE-2 in combination with ILE-3. Two samples were fabricated by tearing and twisting the upper layer (see Fig 4.4c) and thus feature a region with R-type stacking and one with H-type stacking. The fabrication is described in section 3.1. For these samples we see all three ILEs, ILE-1 in one region and ILE-2 and ILE-3 in the other region. Therefore, we conclude that the two different behaviours of the ILE can be attributed to the two stacking orientations.

Typical helicity-resolved photoluminescence spectra of the ILEs are presented in Fig 4.5. The samples are excited by linearly polarized light. For the measurements without

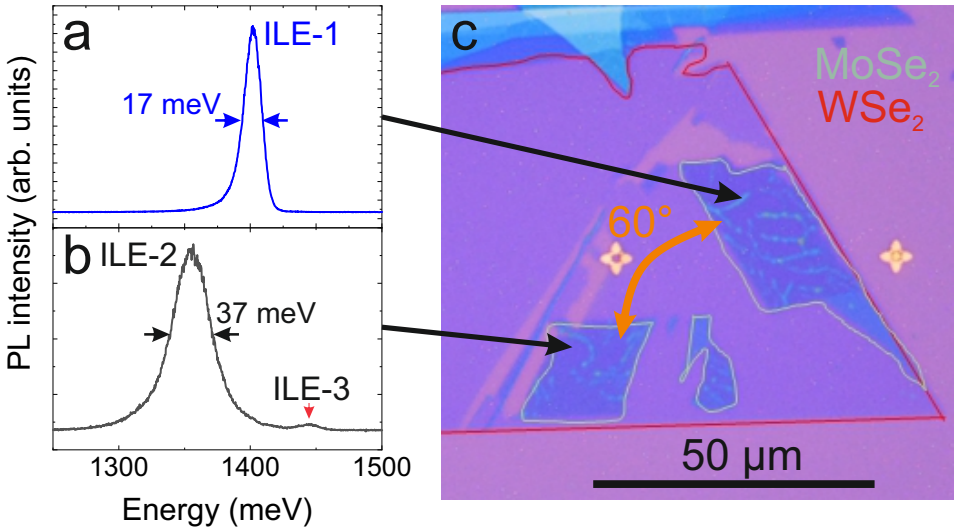

Figure 4.4 | a Photoluminescence spectrum of one region of the H-/R-type $MoSe_2$-WSe_2 heterostructures which shows ILE-1. **b** Photoluminescence spectrum of the other region of the H-/R-type $MoSe_2$-WSe_2 heterostructures which shows ILE-2 and ILE-3. **c** Optical microscope image of the H-/R-type $MoSe_2$-WSe_2 heterostructure fabricated as described in section 3.1.

magnetic field no difference between the intensities or energetic positions for the different polarizations can be seen. This is expected as the different valleys are degenerate. The magnetic field perpendicular to the sample plane lifts the degeneracy. For ILE-1 (Fig 4.5a) the σ^+ component shifts to lower energies, while the σ^- component shifts to higher energies. Due to the energetic splitting the intensities of the peaks change, which leads to a pronounced circular polarization. For ILE-2 (Fig 4.5b) the σ^- polarized component remains at approximately the same energetic position as at 0 T, while the σ^+ component shifts to higher energies. The splitting is opposite and less pronounced than for ILE-1 and also the polarization is smaller. For ILE-3 (Fig 4.5c) a completely different behaviour at 30 T is observed. Both polarization components shift to slightly lower energies and no splitting occurs. Nevertheless, a circular polarization forms. The polarization of the ILEs and its temporal dynamics are discussed in section 4.2.4 in detail.

Fig 4.6 shows the splitting of the σ^+ and σ^- polarized ILE components. The energetic positions are determined by fitting the helicity-resolved PL spectra. As described in section 2.4 an effective g factor can be extracted. For ILE-1 we find a g factor $g_{eff} = -14.4$. This is in good agreement with previous studies on H-type heterostructures [Nag17a, Sey19]. The fit for ILE-2 yields an effective g factor $g_{eff} = +4.4$, which is in qualitative accordance with findings on R-type $MoSe_2$-WSe_2 bilayers [Sey19, Cia19]. Although the intralayer exciton is strongly quenched, we can extract a g factor $g_{eff} = -4.4$ for the $MoSe_2$ intralayer exciton in good agreement with previous experimental

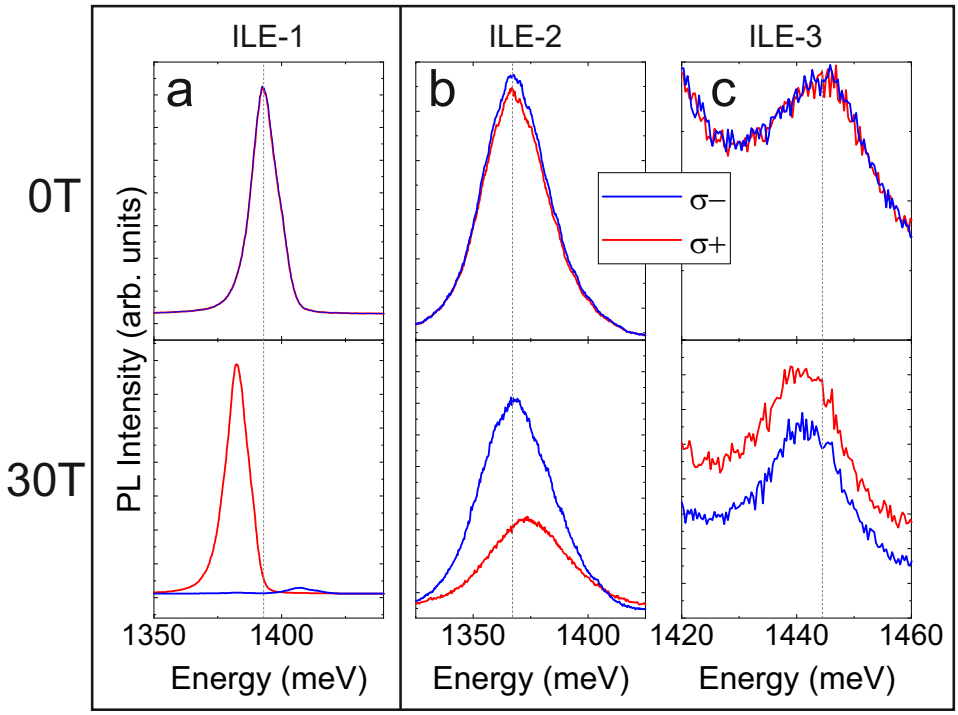

Figure 4.5 | Helicity-resolved photoluminescence spectra of **a** ILE-1, **b** ILE-2 and **c** ILE-3 measured under linear excitation. The upper panels show measurements at 0 T and the lower panels at 30 T. Vertical lines serve as guide to the eye and show the energetic position of the ILEs at 0 T. ILE-1 is observed in H-type heterostructures, while ILE-2 and ILE-3 occur in R-type structures.

and theoretical studies (see section 2.4).

By comparing multiple samples we find effective g factors between −14.2 and −16.8 for ILE-1 and g factors between +2.5 and +5 for ILE-2. Therefore, we can identify the stacking orientation by the different ILEs. ILE-1 features a large negative g factor and appears in H-type heterostructures, while ILE-2 exhibits a smaller, positive g factor and occurs in R-type structures. ILE-3 is only observed in conjunction with ILE-2. This identification is even possible without magnetic field due to the distinct emission energies and spectral linewidths of the ILEs.

The circularly polarized components of ILE-3 reveal no splitting in magnetic fields up to 30 T. In Fig 4.6 multiple datasets for ILE-3 for non-encapsulated and encapsulated samples are shown. The g factor is estimated by an upper boundary of $|g_{eff}| < 1$, which is indicated by the grey-shaded area. To our knowledge such small g factors have not been reported in TMDCs for intralayer ($|g_{eff}| \approx 4$, see section 2.4) or interlayer excitons ($|g_{eff}| > 6$, see section 2.6.2).

Comparing the experimental results to the theoretical calculations presented in section 2.6.2 we can assign the ILEs to the high symmetry stackings present for atomic

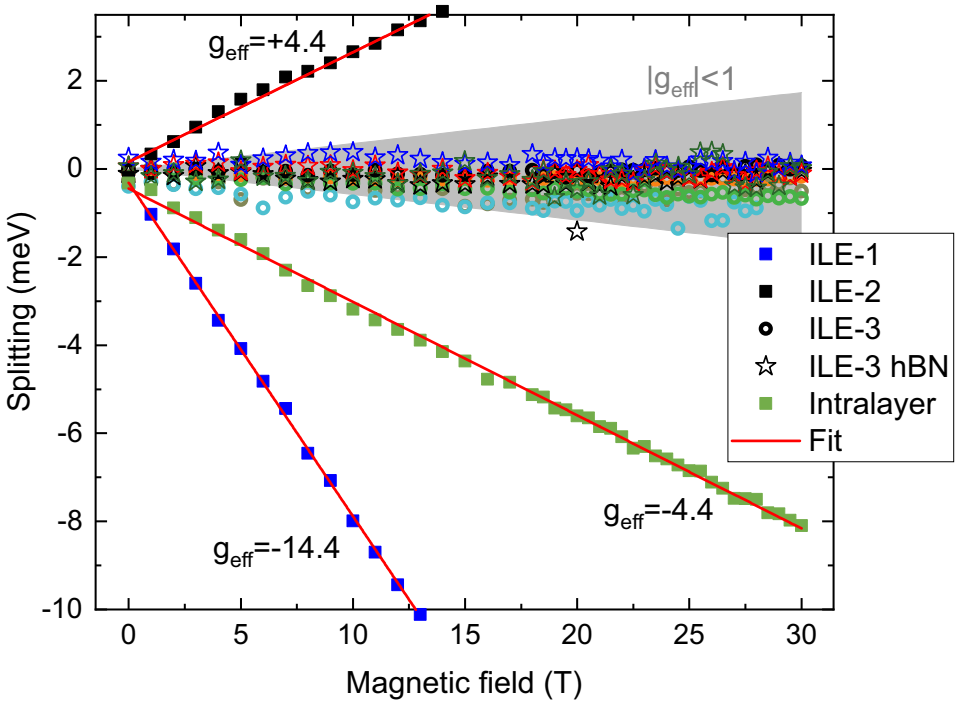

Figure 4.6 | Splitting of the different ILEs as a function of the magnetic field. For ILE-3 multiple datasets of encapsulated (stars) and non-encapsulated (circles) samples are depicted, which all lie within the grey-shaded region corresponding to an effective g factor $|g_{eff}| < 1$. Red lines represent linear fits for the splitting of ILE-1, ILE-2 and the $MoSe_2$ intralayer exciton.

reconstruction. We assign ILE-1 to the spin-conserving transition of the H_h^X stacking configuration. The following reasons corroborate this assignment. The calculated, effective g factor of the H_h^X configuration ($g_{eff}^{theo} = -12.6$) is in qualitative agreement with the measured g factors. In this stacking configuration the transition metal atoms of the upper and lower layer lie directly on top of each other. This configuration favours the ultrafast charge transfer from the intralayer to the interlayer excitons. Additionally, this transition has a sizeable oscillator strength in contrast to other transitions. We assign ILE-2 to the spin-conserving transition of the R_h^X stacking configuration. For this transition the value of the theoretical effective g factor ($g_{eff}^{theo} = +6.19$) is the best match to the experimental values. Also the oscillator strength is comparatively large and it is a band edge transition, which is favoured in PL experiments. The transition metal atoms of the upper and lower layer lie on top of each other for the R_h^h stacking and not in the R_h^X stacking. After the charge transfer from intralayer excitons to the R_h^h configuration the charges relax subsequently to the R_h^X stacking region.

For ILE-3 an effective g factor $|g_{eff}| < 1$ is observed. In the calculations no direct transition features such small g factors. Therefore, T. Woźniak and J. Kunstmann calculated the g factors of indirect transitions in analogy to [Woź20]. As the selection

rules for momentum indirect transitions are not known, these effective g factors are only valid with respect to their magnitude $|g_{eff}|$. The values are given in table 4.1. By comparing the magnitudes only the $\Gamma/\Sigma^{\pm}$ transition features a small g factor. Therefore, we propose the $\Gamma/\Sigma^{\pm}$ transition as an option for ILE-3.

transition	K^+/K^-	K^+/Σ^-	K^+/Σ^+	Γ/K^+	Γ/Σ^+
$\lvert g_{eff}^{theo} \rvert$	17.4	13.8	9.9	5.6	2.0

Table 4.1: Transitions and corresponding absolute values for the effective ILE g factors of R-type $MoSe_2$-WSe_2 heterostructures. X/Y denotes the transition from the valence band of WSe_2 at X to the conduction band of $MoSe_2$ at Y. The sign reversed combinations are counterparts to the given transitions.

4.2.2 Anomalous behaviour of the valley splitting

The valley splitting and corresponding effective g factors are discussed in the previous section 4.2.1. Here, we identify an anomalous behaviour of the valley splitting of ILE-1 in H-type and ILE-2 in R-type $MoSe_2$-WSe_2 heterostructures. This is shown in Fig 4.7. As described in section 2.4 the splitting is expected to be linear. For the H-type sample a nonlinear behaviour is observed at 23.8 T, 24.6 T and 25.2 T. Due to the broader linewidth of ILE-2, the dataset for the R-type structure is noisier. Nevertheless, a nonlinear behaviour is found at 23.2 T. Additional deviations from the linear behaviour may occur at 19 T and 26.5 T. These anomalies were measured on multiple samples and different measurement days. A systematic error of the setup can be excluded as the valley splitting of the intralayer exciton, which is tracked simultaneously, shows a strictly linear behaviour.

The origin of this anomalous behaviour remains unclear. A possible explanation could be given by band crossings, which was investigated by P. Nagler in his doctoral thesis [Nag18]. As the magnetic field increases, the bands shift and the upper conduction band in the K^+ valley aligns with the lower conduction band of the K^- valley. However, this occurs at far lower energies and therefore does not explain the behaviour. Delhomme et al. observe a similar feature for H-type $MoSe_2$-WSe_2 heterostructures [Del20] and assign it to resonant behaviour with the E'' phonons of $MoSe_2$ and WSe_2. This model fits relatively good for the H-type structure. For this work this explanation is not suitable as the investigated R-type heterostructures reveal an anomaly at about the same magnetic field value. Due to the different g factors this corresponds to a completely different energetic splitting and does not match with the suggested phonons. Therefore,

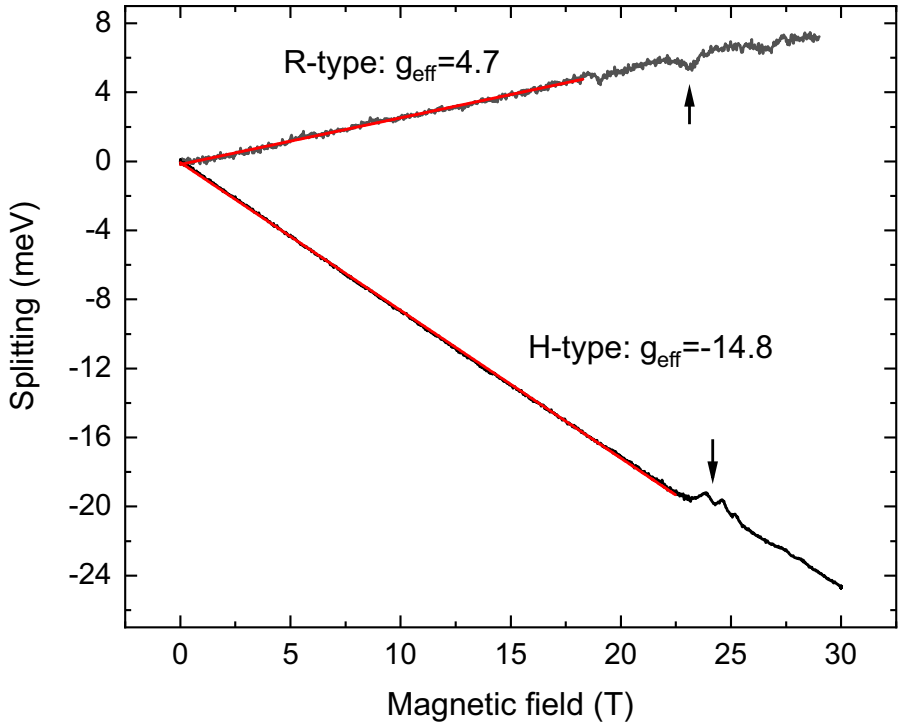

Figure 4.7 | Valley splitting for an R-type and an H-type $MoSe_2$-WSe_2 heterostructure as a function of magnetic field. The effective g factor is extracted from the linear fits (red lines). Anomalous behaviour is marked by the arrows.

the origin of the anomalous behaviour is not yet known and further experiments and calculations are required to provide an explanation.

4.2.3 Negative quadratic magnetic shift

Another unexpected phenomenon occurs for the quadratic energy shift in magnetic field. For the investigated R-type $MoSe_2$-WSe_2 heterobilayers we find a negative quadratic shift for ILE-3. Generally, the quadratic contribution to the energy shift is expected to be positive. It is called diamagnetic shift and further described in section 2.4.

A positive diamagnetic shift is indeed observed for ILE-1, ILE-2 and the $MoSe_2$ intralayer exciton as depicted in Fig 4.8. Due to the large spectral linewidth of ILE-1 and ILE-2, no clear quadratic behaviour of the energetic shift in magnetic field can be extracted. Nevertheless, a positive shift is confirmed and estimated by the blue-black region. The intralayer exciton of $MoSe_2$ shows a clear positive diamagnetic shift, in agreement with previous results on TMDCs [Sti16, Ple16, Zip18]. For ILE-3 we find a negative quadratic magnetic shift. A quadratic shift of $(-2.8 \pm 0.6)10^{-3}$ meV T^{-2} for non-encapsulated and $(-4.5 \pm 0.7)10^{-3}$ meV T^{-2} for encapsulated heterostructures is extracted by the parabolic

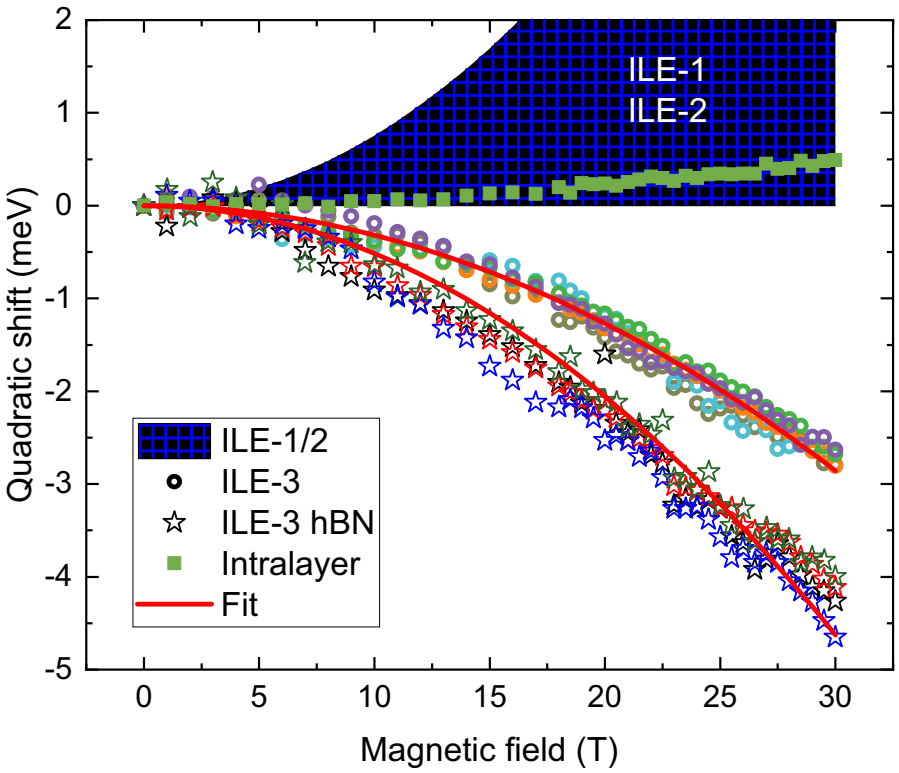

Figure 4.8 | Quadratic shift for the different ILEs of $MoSe_2$-WSe_2 heterostructures as a function of magnetic field. The blue-black region estimates the quadratic shift for ILE-1 and ILE-2. The negative quadratic shift for ILE-3 is fitted by a quadratic fit (red lines). It is stronger for hBN-encapsulated samples.

fit shown in Fig 4.8. Currently, a qualitative theoretical explanation is developed and will be published in [Hol21b].

4.2.4 Dynamics of the interlayer exciton valley polarization

In this section time-resolved measurements of the ILE valley polarization of $MoSe_2$-WSe_2 heterostructures in magnetic field are presented. We find a slow build-up of the polarization in the order of 100 ns for all ILEs.

In contrast to the relaxation time, the temporal evolution of the valley polarization is vastly different. ILE-1 shows an initial positive polarization, which increases in magnetic field up to nearly unity for 30 T. For ILE-1 there is a direct correspondence between the measured circular polarization of the emission and the valley polarization. ILE-2 also exhibits an initial positive polarization. Over time, the polarization is inverted and for the highest magnetic fields we find a polarization of -40%. In contrast to ILE-1, the ILE-2 emission is composed of contributions from two different stacking regions, which have different selection rules. In the time after optical excitation, interlayer excitons

relax from the R_h^h stacking to the energetically favourable R_h^X stacking region. Due to the change of the stacking region, the helicity of the emitted light for a given valley polarization is reversed. ILE-3 shows an initial, positive valley polarization, which decays to zero. The behaviour of the polarization is qualitatively explained by the g factors of the respective ILEs.

The time-resolved measurements in magnetic fields were conducted in the High Field Magnet Laboratory in Nijmegen (see section 3.3). A pulsed laser with a wavelength of 640 nm was utilized. All measurements were performed with linear excitation. An integration time ranging from 120 s to 600 s and a laser power ranging from 3.4 μW to 9.2 μW were used depending on the PL intensity. The signal was filtered by a suitable bandpass and detected by an APD.

ILEs in TMDC heterostructures feature very long lifetimes in contrast to intralayer excitons. Due to the spatial separation of electrons and holes, the Coulomb interaction is reduced and the lifetime increases [Pal15, Sch16a]. Time- and polarization-resolved PL measurements of the ILE at 0 T are shown in Fig 4.9a. The lifetime is fitted via a biexponential fit. For all ILEs the short lifetime is in the order of 30 ns and the long lifetime in the order of 200 ns. The biexponential decay may stem from a scattering between dark and bright excitons [Zha15, Cho21].

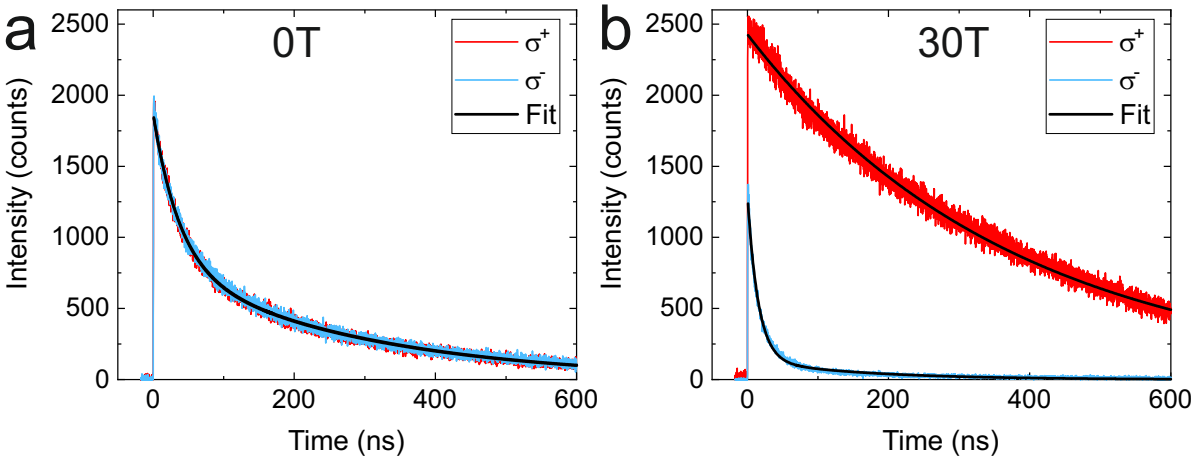

Figure 4.9 | Time- and polarization-resolved PL spectra at **a** 0 T and **b** 30 T of ILE-1 of an H-type $MoSe_2$-WSe_2 heterostructure measured under linear excitation. The black curves represent biexponential fits to the spectra. Due to the degeneracy of the valleys at 0 T the curves overlap in **a**.

Here, we are interested in the valley polarization. At 0 T the valleys are degenerate and there is no polarization. When a magnetic field is applied, the degeneracy of the valleys is lifted. Therefore, one valley is energetically more favourable than the other and a polarization arises (see section 2.4). This is shown in Fig 4.9b. The splitting

between the valleys is quantified by the g factor. For the measured H-type $MoSe_2$-WSe_2 heterostructure with a g factor $g \approx -14$ the σ^+ polarized transition shifts to lower energies while the σ^- polarized transition shifts to higher energies. Consequently, intervalley scattering leads to an increased intensity for the σ^+ polarized transition and a decreased intensity for the σ^- polarized transition.

The circular polarization degree is calculated by the difference of the intensities of σ^+ and σ^- polarized light divided by their sum, as described in section 2.1.1. Positive polarization represents a stronger intensity of the σ^+ polarized transition, while negative polarization implies a stronger intensity of the σ^- polarized transition. For ILE-1 the circularly polarized transitions are assigned to the H_h^X stacking configuration. Therefore, the measured circular polarization is equivalent to the valley polarization of ILE-1. Time-resolved polarization measurements at different magnetic fields are depicted in Fig 4.10a for ILE-1 of an H-type $MoSe_2$-WSe_2 heterostructure. Evidently, for 0 T there is no valley polarization. When a magnetic field is applied, an initial valley polarization, which slowly increases to its final value is observed. At the highest magnetic fields the valley polarization is close to unity, which corroborates measurements reported for an H-type $MoSe_2$-WSe_2 heterostructure [Nag17a]. This build-up of the polarization is fitted by the following formula:

$$P(t) = P_f + (P_i - P_f) \exp\left(-\frac{t}{\tau}\right)$$

Here, $P(t)$ is the time-resolved circular polarization, $P_i = P(0)$ its initial value and $P_f = P(\infty)$ its final value. t is the time and τ the relaxation time of the polarization. The results of the fits are presented in Fig 4.10b and c. The initial polarization P_i stems from the intralayer excitons. Since they feature a g factor of about -4 they exhibit a positive valley polarization in magnetic fields. The ILEs form via ultrafast charge transfer out of the intralayer excitons and adopt their polarization. Due to the far larger absolute value of the ILE-1 g factor ($|g| \approx 14$), the valley polarization increases over time to a final value P_f. With increasing magnetic field the polarization overall increases and the relaxation time decreases. For the highest magnetic fields the polarization is close to unity and the relaxation time declines to 28 ns. The anomaly discussed in section 4.2.2 is visible in Fig 4.10b and c at 24.3 T.

For R-type structures a different behaviour is observed. Fig 4.11 shows the time-resolved circular polarization of ILE-2 in magnetic field. We find an inversion of the circular polarization. After an initial positive value, the polarization relaxes to negative values.

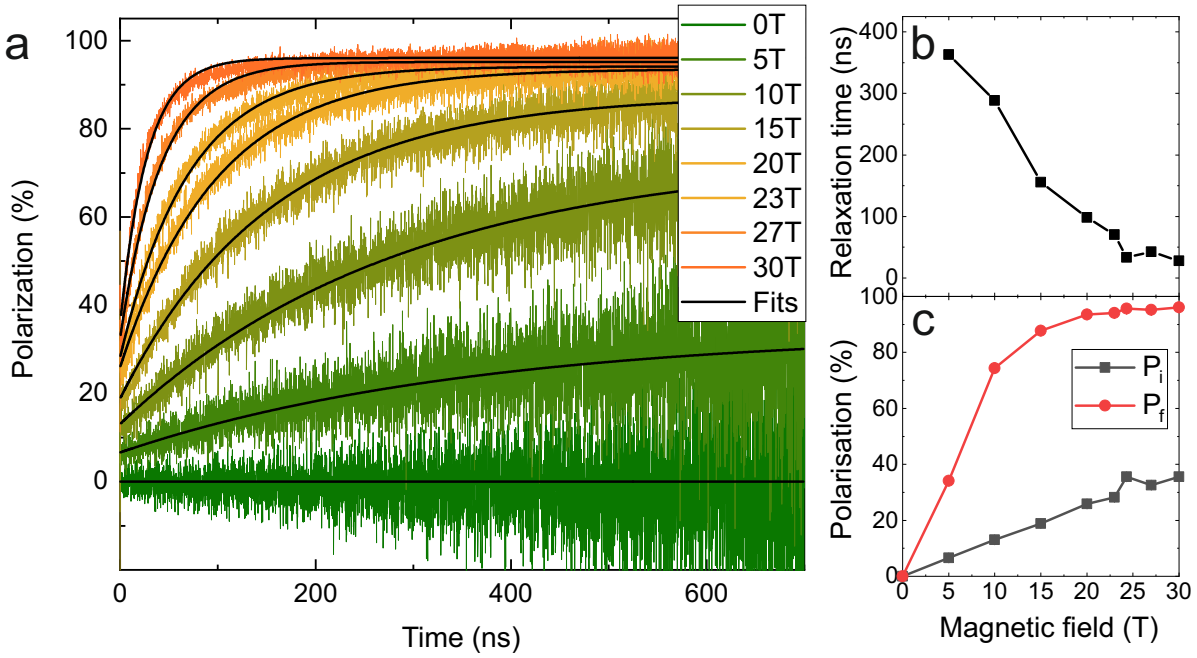

Figure 4.10 | a Time-resolved circular polarization of ILE-1 of an H-type $MoSe_2$-WSe_2 heterostructure at different magnetic field values. The measurements were performed under linear excitation and the curves are fitted exponentially (black lines). **b** Relaxation time as a function of magnetic field extracted from fitting the circular polarisation. **c** Initial P_i and final P_f polarization as a function of magnetic field obtained from fitting the circular polarization. The anomaly discussed in section 4.2.2 is visible in the fit results **b** and **c**. For better clarity it is not shown in **a**.

For ILE-2 the electrons and holes first relax to the R_h^h and subsequently to the R_h^X stacking configuration. Therefore, the measured circular polarization is not the valley polarization, but the combination of the valley polarization of excitons at the R_h^h and R_h^X stacking. The initial positive polarization originates from the valley polarization of the intralayer excitons, analogous to ILE-1. The ultrafast charge transfer creates ILEs at the R_h^h stacking configuration. This configuration features a negative g factor and therefore we observe a positive circular polarization. Subsequently, the ILE relax to the energetically favourable R_h^X stacking. Since the g factor of this stacking is positive, it shows an opposite circular polarization, i.e. a negative one. The experimental measurement shows the overall circular polarization of the interlayer PL. Therefore, we first observe a positive circular polarization which relaxes to negative values over time. The monoexponential fit cannot simulate this behaviour correctly, but indicates general tendencies. The initial circular polarization increases slightly, while the absolute value of the final polarization increases with rising magnetic field up to a value of 40%. The relaxation time declines with increasing magnetic field to a value of 66 ns for 27.5 T.

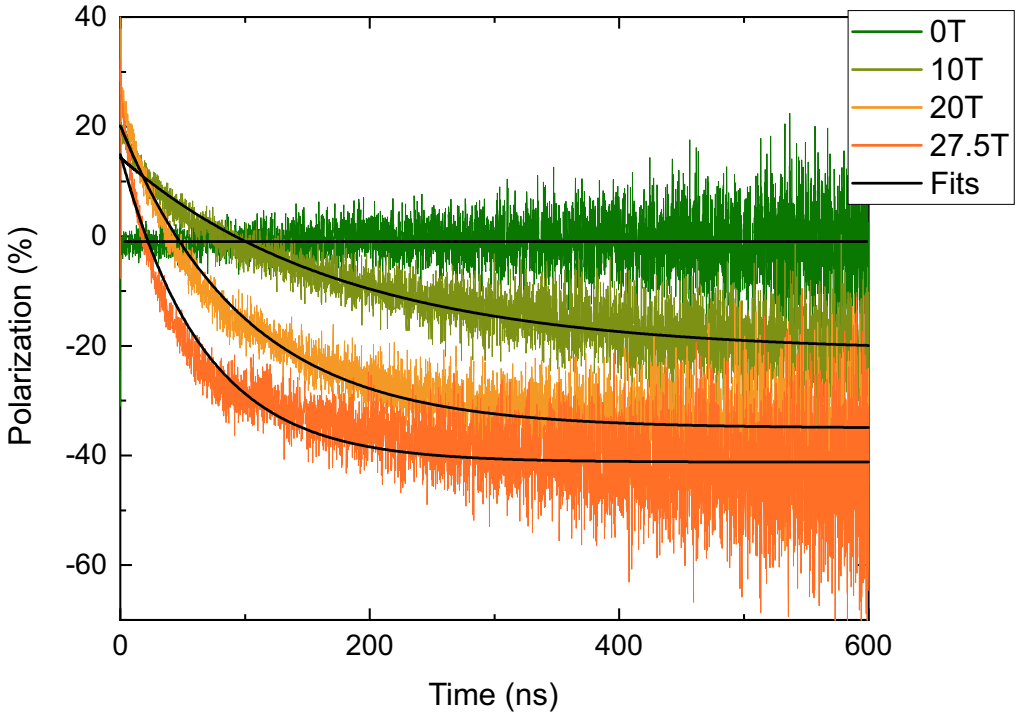

Figure 4.11 | Time-resolved circular polarization of ILE-2 of an R-type $MoSe_2$-WSe_2 heterostructure at different magnetic field values. The measurements were performed under linear excitation and the curves are fitted exponentially (black lines).

Furthermore, time-resolved PL experiments for ILE-3 were conducted. For measurements in magnetic fields ranging from 5 T to 30 T we find an initial positive circular polarization, which decays to zero. Exemplarily, the polarization for 0 T and 30 T is shown in Fig 4.12. The initial polarization is transferred from the intralayer excitons, analogous to ILE-1 and ILE-2. Due to the low g factor ($g < 1$) of ILE-3 the polarization decays to zero. Since the PL intensity of this peak is lower than of ILE-1 and ILE-2, the signal to noise ratio is worse. Therefore, the fits show only the general tendencies. For measurements in magnetic field an initial valley polarization $P_i \approx 10\%$ and a final polarization of $P_f \approx 0$ can be extracted. The relaxation time is in the order of 50 ns. In section 4.2.1 the $\Gamma/\Sigma^{\pm}$ transition was proposed as a candidate for ILE-3. The measured circular polarization is equivalent to the valley polarization of this transition.

In summary, we measure the temporal behaviour of the circular polarization for ILE-1, ILE-2 and ILE-3 in H-type and R-type $MoSe_2$-WSe_2 heterostructures. As a result, the differences in the temporal evolution of the valley polarization can be explained qualitatively by the different g factors of the ILEs. Corresponding theoretical calculations are currently performed and will be published with the presented experimental data in [Hol21a]. Due to the spatial separation of electron and holes, ILEs exhibit long valley

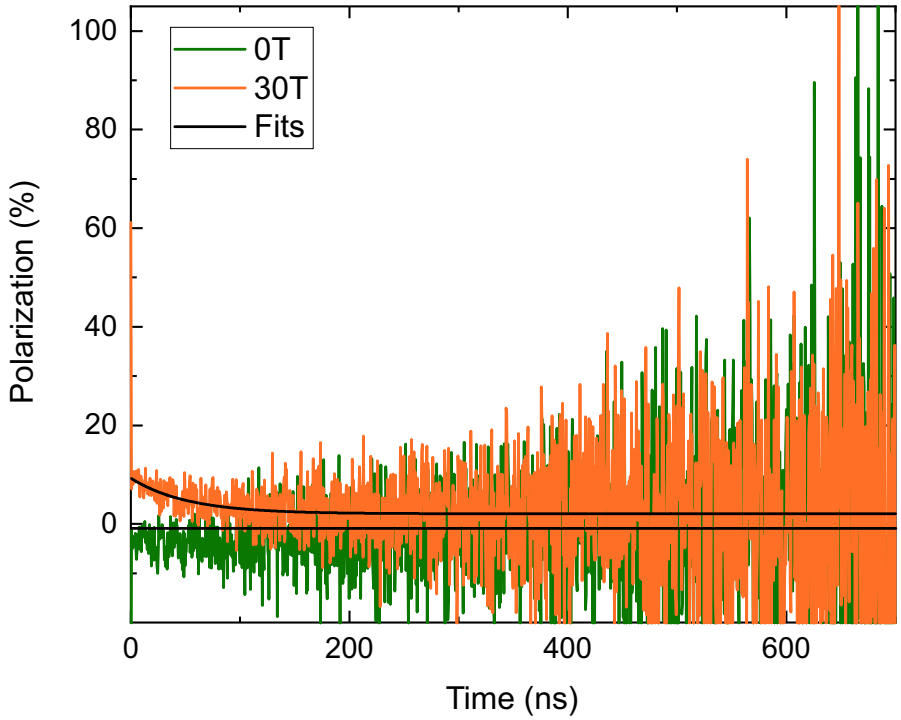

Figure 4.12 | Time-resolved circular polarization of ILE-3 of an R-type $MoSe_2$-WSe_2 heterostructure at 0 T and 30 T. The measurements were performed under linear excitation and the curves are fitted exponentially (black lines).

polarization lifetimes. Therefore, ILEs are a promising candidate for future valleytronics devices.

4.3 Characterization of twisted bilayers via Raman spectroscopy

With the discovery of superconductivity in "magic-angle" graphene [Cao18] the research interest in twisted bilayer structures increased remarkably. As a consequence a similar phenomenon was discovered for twisted bilayer WSe_2 [Wan20b]. In this work, twisted TMDC bilayers are further investigated via Raman spectroscopy. As introduced in section 2.5, the twist angle between the two layers will be denoted as $0° \leq \theta \leq 60°$. While for misaligned structures moiré lattices emerge (see section 2.5.1), for small twist angle deviations δ from 0° or 60° atomic reconstruction (see section 2.5.2) takes place. In this case, the twist angle will be denoted as $\theta = 0°/60° \pm \delta$ for R-/H-type bilayers. For the experiments multiple samples were fabricated. A series of 15 twisted $MoSe_2$ homobilayers was produced by M. Scheuck and a series of 16 twisted WSe_2 homobilayers

was made by J. Bauer and K. Lin making use of the tear and stack method (see section 3.1). Therefore, the twist angle of these samples is precisely known. Over 30 $MoSe_2$-WSe_2 heterobilayers were fabricated by M. Kempf, P. Nagler, P. Parzefall and myself. For these heterostructures the twist angle is determined by SHG measurements, which comes along with comparatively large errors in the range of $\pm 2°$ depending on the specific samples. R- and H-type heterobilayers are distinguished by the ILE photoluminescence signal as described in section 4.2.1.

4.3.1 Atomic reconstruction in H- and R-type heterobilayers

In this section the results of low-frequency Raman measurements on atomically reconstructed $MoSe_2$-WSe_2 heterobilayers are presented, which are published in [Hol20]. We find, that the interlayer shear mode occurs only in H- and R-type heterostructures with a twist angle deviation $\delta < 4°$, which are atomically reconstructed. We can further distinguish between H- and R-type bilayers by the position and intensity of the ISM. A shift of the shear mode between H- and R-type structures was also reported for $MoSe_2$ and WSe_2 homobilayers [Pur15]. Furthermore, we reproduce these measurements in hBN-encapsulated heterostructures. Altogether, we propose Raman spectroscopy as a facile and powerful tool to identify commensurate stacking configurations. In contrast to AFM or TEM this method is contactless and non-invasive.

As described in section 2.5.3 the interlayer shear and breathing modes are well known for TMDC multilayers. While the IBM is only weakly dependent on the twist angle, the ISM is strongly suppressed for misaligned bilayers caused by the lack of a long range atomic registry in the moiré pattern. For R- and H-type stacking the ISM is visible [Nay17]. We investigated multiple samples by low-frequency Raman spectroscopy. An exemplary sample picture of a heterostructure with an R-type and an H-type region is shown in section 3.1. Further measurements on additional samples (not shown) corroborate the presented results. Fig 4.13 shows low-frequency Raman measurements on several samples.

All measurements were conducted in a cross-polarized setup with a laser wavelength of 532 nm, a laser power of 2.5 mW and a spot size of approximately 1 μm. For each sample several spots were measured. The Raman shift is determined precisely by comparing the Stokes and Anti-Stokes peak. To ensure the quantitative comparability all spectra are normalized to the sum of the intensities of the A_1' intralayer optical phonon modes of $MoSe_2$ and WSe_2. As can be seen in Fig 4.13a, for the R- and H-type structures an ISM is observed while for the not aligned heterostructures with larger twist angle deviations

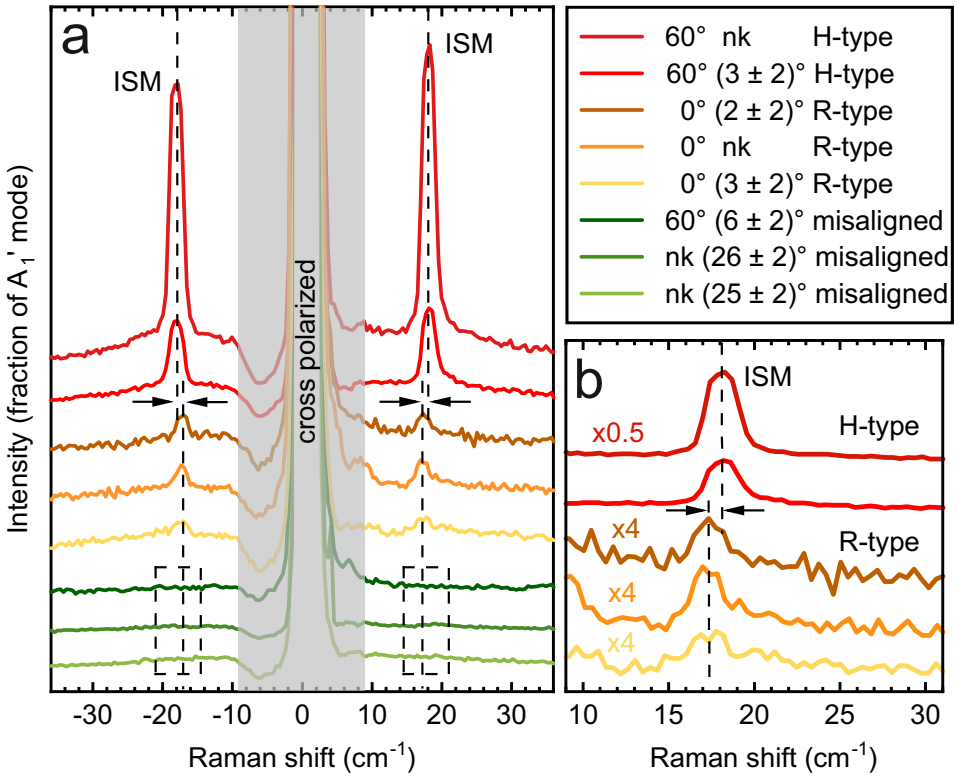

Figure 4.13 | a Cross-polarized low-frequency Raman spectra of $MoSe_2$-WSe_2 heterostructures with different twist angles. The by SHG-measurements determined twist angle deviation δ from 0°/60° together with its error is given on the right-hand side. nk means not known. The ISM is only visible for aligned structures. **b** Close-up of the Stokes region for the R- and H-type samples with renormalized curves as indicated. The ISM of H-type structures is at slightly higher energies than the ISM of R-type structures.

from 0°/60° no ISM is visible. We attribute this to the effect of atomic reconstruction. For samples with twist angle deviation $\delta < 4°$ atomic reconstruction takes place, the crystal lattices rearrange in a high symmetry stacking and therefore the ISM emerges. Fig 4.13b shows a close-up of the measurements of the aligned heterostructures. A clear difference between R-type and H-type samples is detected. The energetic position of the ISM of the H-type structures is at $(18.0 \pm 0.1)\,\mathrm{cm}^{-1}$, while the position of the ISM of the R-type samples lies at $(17.4 \pm 0.1)\,\mathrm{cm}^{-1}$. Also for H-type bilayers the intensity of the ISM is five to ten times larger than the one for R-type samples owing to the smaller interlayer bond polarizability for the R-type configuration [Pur15]. These results were reproduced for $MoSe_2$-WSe_2 heterostructures encapsulated in hBN, which is shown in Fig 4.14. Since the hBN lattice is completely incommensurate with the $MoSe_2$ and the WSe_2 lattices, the ISM is undisturbed. Therefore, this technique allows for contactless determination of the stacking configuration of encapsulated and non-encapsulated aligned heterostructures.

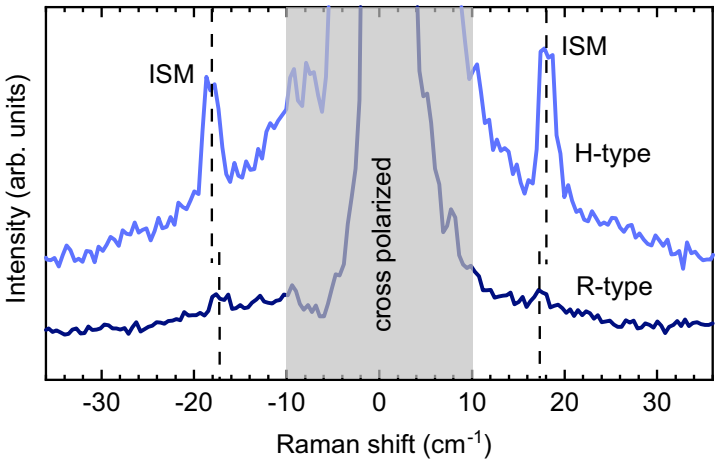

Figure 4.14 | Cross-polarized low-frequency Raman spectra of an H-type (light blue) and and R-type (dark blue) $MoSe_2$-WSe_2 heterostructure encapsulated in hBN.

4.3.2 Moiré phonons in misaligned homo- and heterobilayers

Moiré phonons are acoustic phonons folded by the moiré superlattice, as described in section 2.5.4. Lin et al. discovered moiré phonons in twisted MoS_2 homobilayers in 2018 [Lin18] and coined their name. Within the framework of this thesis, we measured moiré phonons for twisted $MoSe_2$ and WSe_2 homobilayers and even twisted $MoSe_2$-WSe_2 heterobilayers. The results are published in [Par21b] for $MoSe_2$ and $MoSe_2$-WSe_2 and will be published in [Lin21] for WSe_2.

All measurements were conducted in an unpolarized setup configuration. For each sample several spots were measured and Raman peaks were identified by comparing Stokes and Anti-Stokes spectra. A laser wavelength of 532 nm, a typical laser power of 2.5 mW, a typical integration time of 60 s and a spot size of approximately 1 μm were used. The laser power and integration time were slightly adjusted between measurements on different materials. The phonon dispersions were calculated by B. Peng, as described in Ref [Pen16]. Fig 4.15 shows moiré phonons in twisted $MoSe_2$ and WSe_2 homobilayers. For the $MoSe_2$ bilayers longitudinal acoustic (red arrows) and transverse acoustic (blue arrows) phonons can be identified in samples with twist angles from 5° to 29° (see Fig 4.15a). Fig 4.15b shows a comparison between the experimental results and the calculated phonon dispersion. For this, the dispersion was interpolated as described in section 2.5.4. The estimated error of the twist angle θ is $\pm 1°$ and stems from the tear and stack fabrication method. The error of the Raman shift is below the symbol size. We find a very good agreement between the experimental results and the theoretical calculation.

The twisted WSe_2 homobilayers are analysed analogously and the results are presented

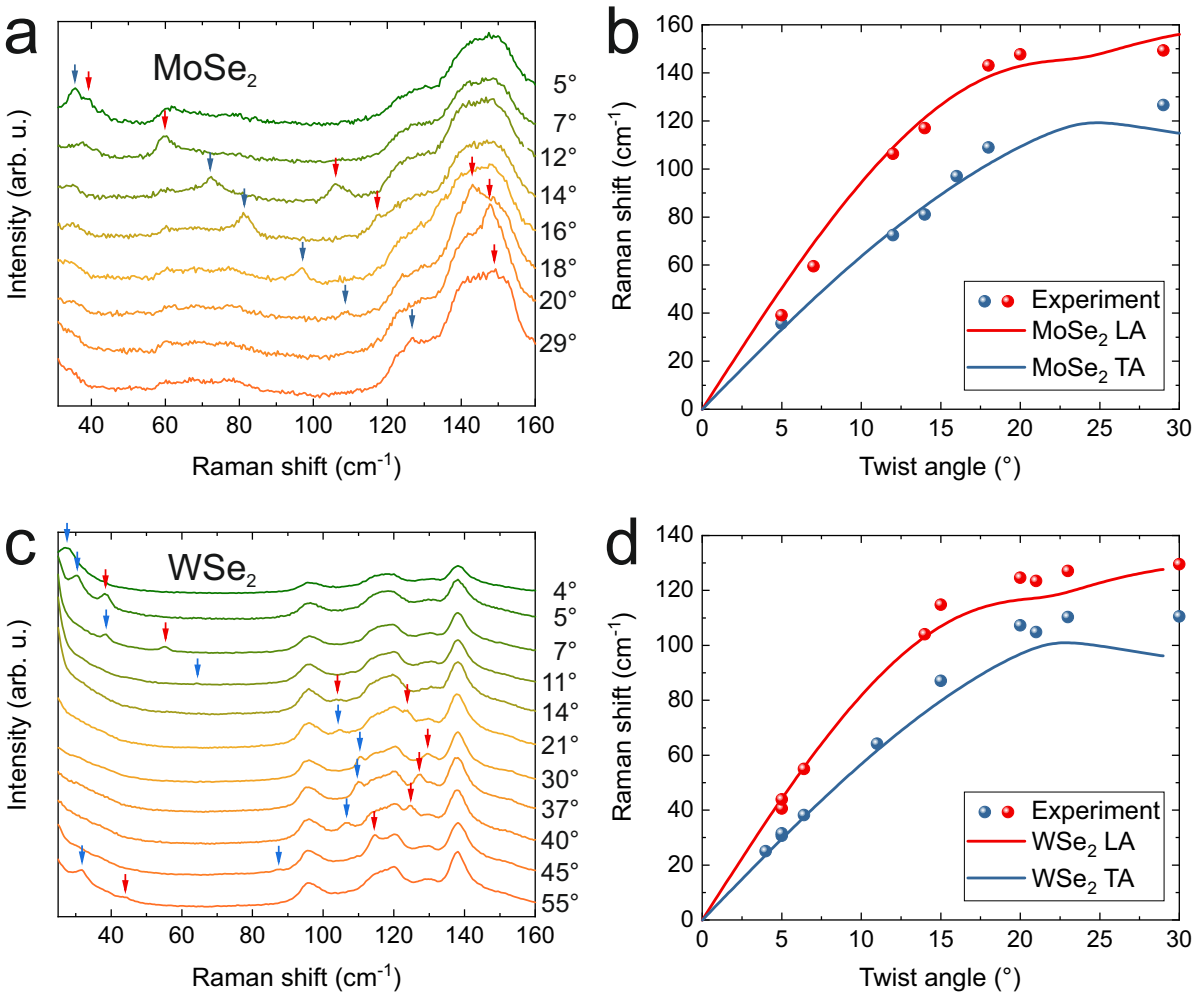

Figure 4.15 | Unpolarized Raman spectra of twisted **a** $MoSe_2$ and **c** WSe_2 homobilayers. The twist angle θ is given on the right side. The arrows mark the assignment to longitudinal (red) and transverse (blue) folded acoustic phonons. Comparison of the experimental measurements of **b** $MoSe_2$ and **d** WSe_2 to the calculated longitudinal (LA, red) and transverse (TA, blue) folded acoustic phonon branches.

in Fig 4.15c and d. Here, samples with twist angles ranging from 4° to 55° were investigated. Due to the symmetry of the material, moiré phonon frequencies of samples with twist angles bigger than 30° are equivalent to samples with twist angle $60° - \theta$. Therefore Fig 4.15d shows only twist angles up to 30°. Also for the WSe_2 homobilayers we find a very good agreement between experiment and theory.

In the following, the results on $MoSe_2$-WSe_2 heterobilayers will be presented. Fig 4.16a shows exemplary Raman spectra of the longitudinal (red arrows) and transverse (blue arrows) folded acoustic phonons of $MoSe_2$. We are able to identify moiré phonons of $MoSe_2$ or WSe_2 on 12 samples. For three samples, three moiré phonons are observed and for one sample even four folded acoustic phonons are identified. Fig 4.16b shows

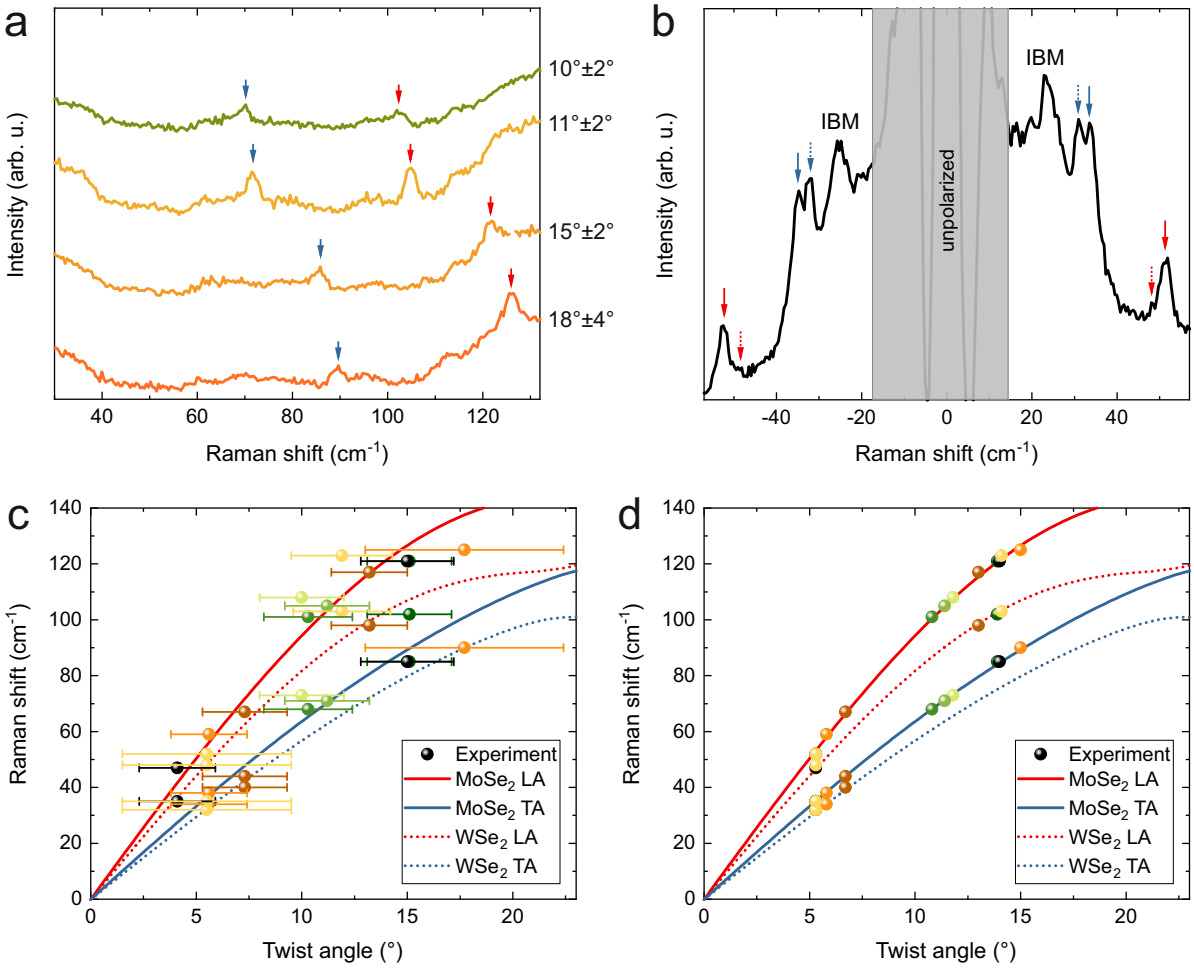

Figure 4.16 | a Unpolarized Raman spectra of twisted $MoSe_2$-WSe_2 heterobilayers with their respective twist angle θ determined by SHG. **b** Unpolarized low-frequency Raman spectra of a twisted $MoSe_2$-WSe_2 heterobilayer with twist angle $\theta = 5° \pm 3°$. Arrows mark moiré phonon modes as indicated in the key below. **c** Comparison of the experimental measurements to the calculated folded acoustic phonons. The twist angle is determined by SHG. Different colours indicate different samples. **d** Reevaluation of **c** by shifting experimental values within the SHG error margin for the best fit.

a spectrum were both, longitudinal (red arrows) and transverse (blue arrows) folded acoustic phonons of $MoSe_2$ and longitudinal (red dotted arrows) and transverse (blue doted arrows) folded acoustic phonons of WSe_2 can be seen. The longitudinal acoustic phonon of WSe_2 is barely visible. Nevertheless, this mode is confirmed in measurements on different spots, where the other phonons are less pronounced. In Fig 4.16c a summary of all identified moiré phonons is shown in comparison to the theoretically calculated phonon branches. Different colours indicate different samples. As the tear and stack method is not viable for heterostructures the twist angle θ is measured via SHG. This yields a rather large error depending on the sample (see section 3.2.2) and is indicated

in Fig 4.16c by the error bars. To achieve a more precise determination of the twist angle the experimental values are shifted within the SHG twist angle error margin for the best fit to the theoretical phonon dispersion. The results are shown in Fig 4.16d. We find a nearly perfect agreement between the experimental data and the theoretical calculations. Therefore, this method can be used to determine the relative twist angle very accurately at the precise position of the measurement. It has to be noted, that due to the limited accuracy of DFT calculations, there may still be an uncertainty in the absolute value of the twist angle.

4.3.3 Interlayer breathing mode in twisted Tungsten Diselenide bilayers

While the interlayer shear mode exhibits a strong dependence on the twist angle in bilayer TMDCs and even vanishes for large twist angle deviations δ from $0°/60°$, the interlayer breathing mode is only weakly dependent on the twist angle (see section 2.5.3). Nevertheless, this dependence is confirmed by calculations [Mai20] and experimental results [Pur16, Qua21]. In contrast to the shear mode the breathing mode is visible for all twist angles. This facilitates the investigation of misaligned bilayers via the IBM.
Here, we investigate the interlayer breathing mode in twisted bilayer WSe_2. We can distinguish the behaviour of the IBM in regions of atomic reconstruction, large moiré period and small moiré period. The results will be published in [Lin21]. The WSe_2 samples are also examined for moiré phonons, which is presented in section 4.3.2 and the results complement each other. For each sample several spots were measured and Raman peaks were identified by comparing Stokes and Anti-Stokes spectra. A laser with a wavelength of 532 nm, a laser power of 2.5 mW and a spot size of approximately 1 μm was used. The integration time for unpolarized measurements is set to 60 s, while for cross-polarized measurements an integration time of 180 s was used. Fig 4.17a shows unpolarized Raman measurements of all investigated samples. The interlayer breathing mode is marked by asterisks. To distinguish between IBM and ISM the unpolarized Raman spectra are compared to the cross-polarized spectra, which are shown in Fig 4.17b. As discussed in section 2.5.3, the breathing mode is forbidden in cross-polarized configuration and therefore we can differentiate between IBM and ISM. Additional peaks in the $\theta = 4°$, $5°$, $7°$ and $55°$ samples belong to moiré phonons and are discussed in section 4.3.2.
In Fig 4.18 the behaviour of the interlayer breathing mode with respect to the twist angle θ is shown. The error from fitting the peak position is smaller than the data points

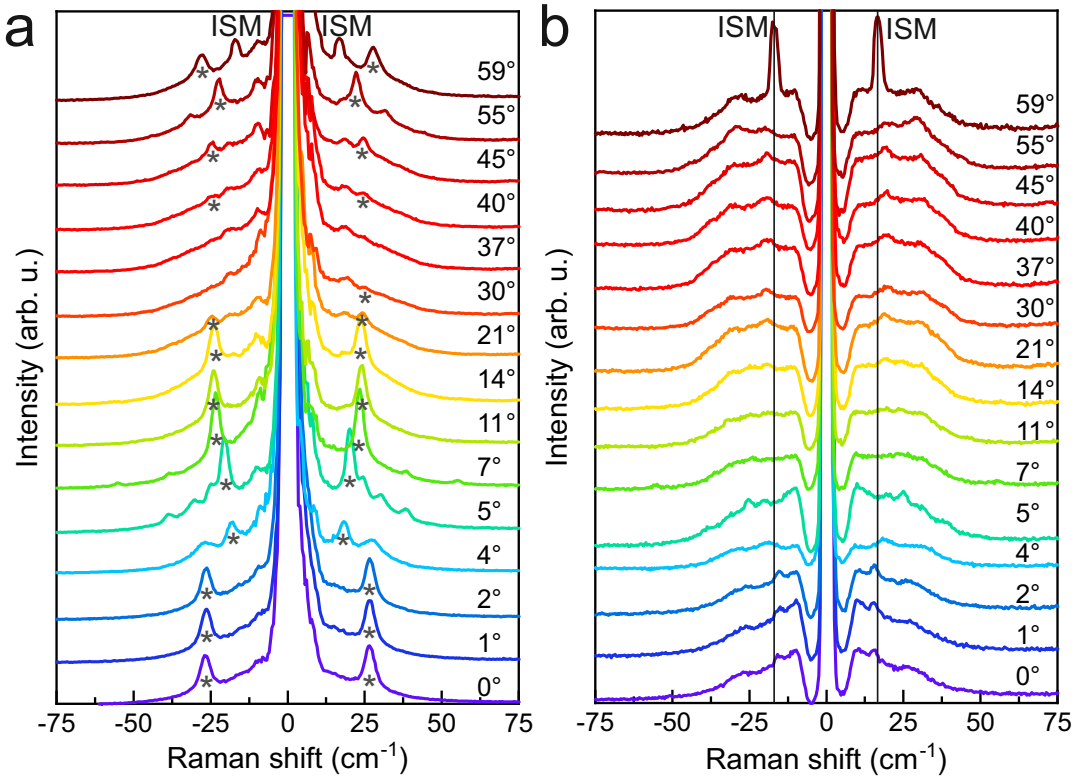

Figure 4.17 | a Unpolarized and **b** cross-polarized low-frequency Raman spectra of twisted WSe_2 homobilayers. The twist angle θ is denoted and the interlayer shear mode and interlayer breathing mode (asterisks) are marked. In cross-polarization the IBM is optically forbidden.

and the estimated twist angle error for the tear and stack method is 1°. For small twist angle deviations $\delta < 4°$ from 0°/60° the IBM frequency is constant. While for the H-type structures the IBM is identical to 2H natural bilayers of WSe_2, the breathing mode for R-type bilayers appears at slightly lower energies. For misaligned structures with a large moiré period the IBM shows a significant twist angle dependence, while for small moiré periods ($15° < \theta < 45°$) the IBM frequency remains nearly constant. Most interestingly, the twist-angle dependence is in very good agreement with the calculated moiré period. We attribute the constant IBM for R- and H-type heterobilayers to atomic reconstruction. In this region no change is expected and the frequency difference between R- and H-type bilayers coincides with the Raman shift of the ISM (see 4.3.1). For misaligned homobilayers a moiré pattern forms. Therefore, the interlayer distance varies and the layers are not perfectly flat any more but exhibit a corrugation [Uch14]. This enables a mixing of the in- and out-of-plane displacement modes and changes the frequency of the IBM. As an additional consequence, the IBM is not completely suppressed in cross-polarization, which can be seen in Fig 4.17b for $\theta = 4°, 5°$. For twist angles between 15° and 45° the moiré period is smaller and almost constant throughout the angle range.

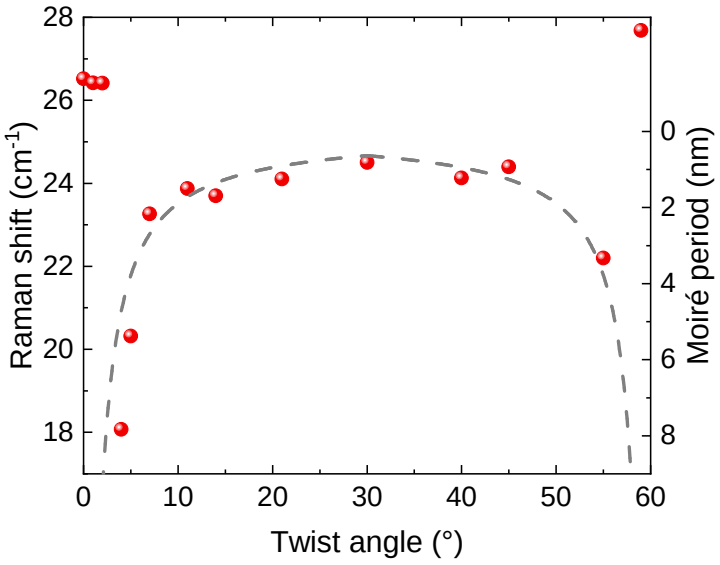

Figure 4.18 | Interlayer breathing mode extracted from the spectra in Fig 4.17a in dependency of the twist angle. The grey dotted line depicts the calculated moiré period scaled to show similarities to the IBM behaviour. For 0°/60° the IBM is shifted due to atomic reconstruction.

Therefore, the IBM is nearly constant in this region. The twist angle dependency of the interlayer breathing mode thus allows the characterization of individual domains over large scale areas of the sample. This is presented in the next section.

4.3.4 Large-scale mapping via hyperspectral Raman imaging

In the last sections different methods of determining the lattice arrangement in twisted bilayers are discussed. While in section 4.3.1 the interlayer shear mode is shown as a tool to determine atomic reconstruction, section 4.3.2 demonstrates precise twist angle identification of misaligned bilayers via moiré phonons. Additionally, section 4.3.3 presents a method to investigate both, atomically reconstructed areas and moiré lattices by the frequency of the interlayer breathing mode. These methods can be used to generate large-scale maps of twisted bilayer samples via hyperspectral Raman imaging. In this section, two examples will be given. The breathing mode of a WSe_2 homobilayer with a twist angle of $\theta = 5°$ is scanned over a large sample area exceeding $1000\,\mu m^2$. We find regions of atomic reconstruction, regions with loose contact between the layers and moiré regions with an intrinsic twist in the investigated sample area. The results will be published in [Lin21]. A $MoSe_2$-WSe_2 heterobilayer with twist angle $\theta = 5° \pm 3°$ was

investigated by single measurements over the whole sample. On the one hand we find regions of atomic reconstruction via the interlayer shear mode, while on the other hand moiré phonons allow a precise twist angle determination in misaligned regions. This is confirmed by the photoluminescence of the interlayer exciton. The presented results are published in [Par21b]. Both samples have twist angles of approximately 5° as this is the most interesting angle region for the investigation of twisted bilayers. While this angle is close to the threshold of atomic reconstruction, the moiré period is also varying significantly and correlated phenomena were reported [Wan20b]. All measurements were conducted with a laser wavelength of 532 nm, a typical laser power of 2.5 mW and a spot size of approximately 1 μm.

WSe_2 homobilayer

The WSe_2 homobilayer was produced by the tear and stack method with a twist angle of $\theta = 5°$ and an uncertainty of 1°. Measurements on this sample are also shown in section 4.3.3. Due to the good signal quality of the interlayer breathing mode, we could scan the sample automatically with an integration time of 10 s per spot.

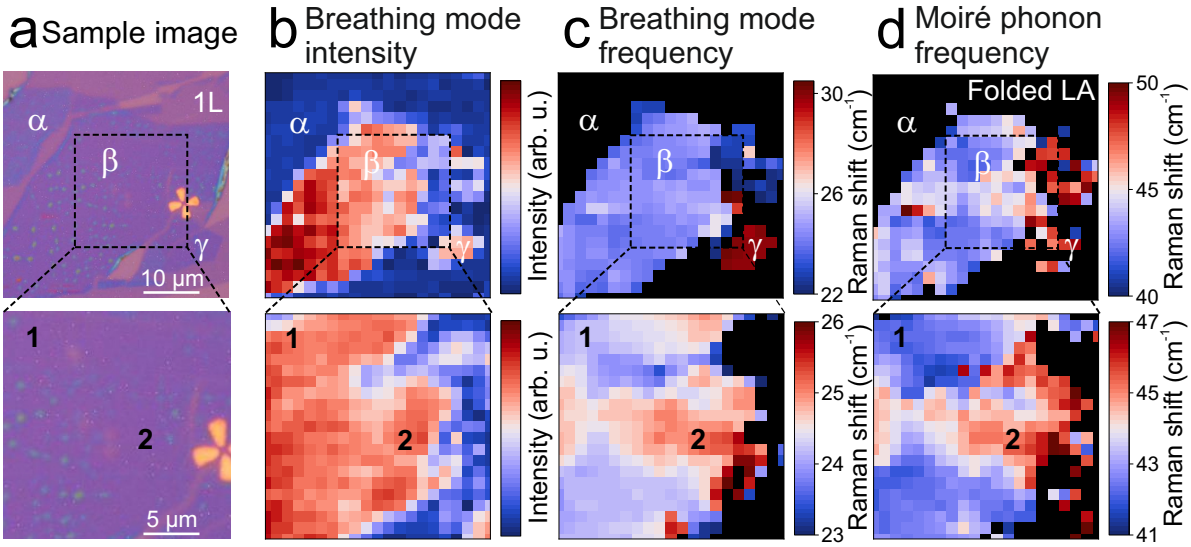

Figure 4.19 | a Microscope image of a 5° twist angle WSe_2 homobilayer with different regions α, β and γ. 1L marks a monolayer region. **b** Spatially-resolved interlayer breathing mode intensity. **c** Spatially-resolved interlayer breathing mode frequency. **d** Spatially-resolved folded longitudinal acoustic phonon frequency.
Region α is assigned to loose contact, β to a moiré pattern and γ to atomic reconstruction. The lower panels show a close-up corresponding to the marked region β with different domains 1 and 2. An intrinsic twist is indicated by the frequency change.

Fig 4.19a shows a microscope image of the scanned area with different bilayer regions

α, β and γ. A rough scan was conducted over the whole area with a step size of 2 μm. A more detailed scan for the β region shown in the close-up (lower panels of Fig 4.19) with a step size of 1 μm shows two domains 1 and 2 in this region. The low-frequency Raman spectra are evaluated by fitting the interlayer breathing mode and the moiré phonons and the results are shown in the upper panels of Fig 4.19 for the rough scan and in the lower panels of Fig 4.19 for the more detailed scan.
Although region α is a bilayer region neither a breathing mode nor moiré phonons can be measured. This region shows the same behaviour as the monolayer regions. We attribute the absence of any Raman signal to loose contact between the layers. In region γ also no moiré phonons are visible, but an IBM can be seen. The IBM is shifted to higher energies to a frequency close to 30 cm^{-1} and therefore we attribute this region to atomic reconstruction. The strong shift is consistent with the IBM behaviour found in section 4.3.3. In region β the breathing mode is at normal frequencies for misaligned WSe_2 homobilayers and also the moiré phonons can be seen. Thus, we attribute this region to the formation of a moiré lattice. Typical spectra for each region are shown in Fig 4.20a.

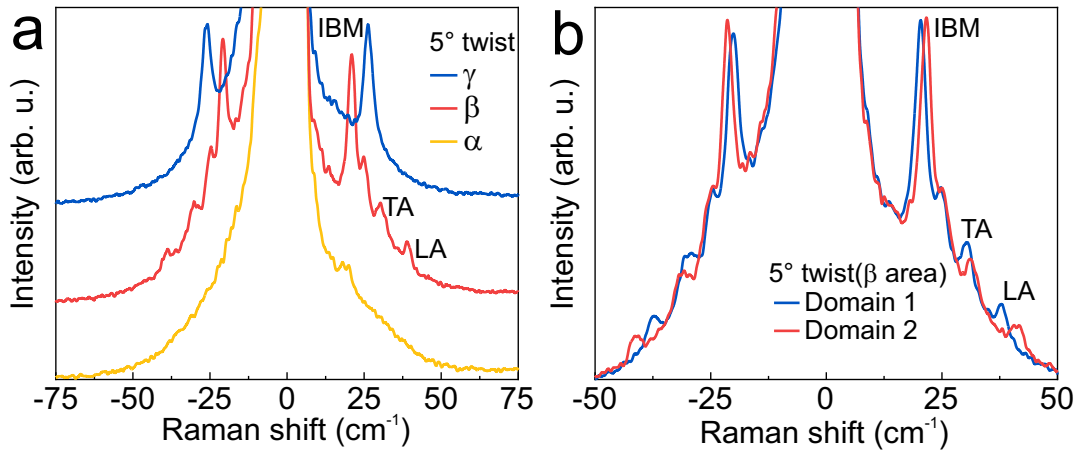

Figure 4.20 | a Low-frequency Raman spectra of a 5° twist angle WSe_2 homobilayer with different regions α, β and γ marked in Fig 4.19. **b** Corresponding Raman spectra from domain 1 and 2 of region β.

In the close-up (lower panels of Fig 4.19) we can identify two different domains in region β. A frequency difference for both, the breathing mode and the moiré phonons is observed between domain 1 and 2. Due to the lower signal intensity, the moiré phonon frequencies shown in Fig 4.19d are significantly noisier. The shift can be clearly seen in the low-frequency Raman spectra shown in Fig 4.20b. The frequency difference between the folded longitudinal acoustic phonons of domain 1 and 2 is about 3.5 cm^{-1}. This corresponds to a variation of $\sim 0.4°$ in the twist angle around the nominal value

of 5° according to the calculated dispersion from section 4.3.2.
In summary, we are able to characterize different regions in the twisted WSe_2 bilayer via hyperspectral Raman imaging. We identify regions of atomic reconstruction, regions with loose contact between the layers and moiré regions with an intrinsic twist in the investigated sample area. The intrinsic twist of this homobilayer can be quantified via the calculated moiré phonon dispersion to ±0.4°.

$MoSe_2$-WSe_2 heterobilayer

As heterostructures cannot be produced by the tear and stack method we rely on SHG measurements for the twist angle determination. The investigated $MoSe_2$-WSe_2 heterobilayer features a twist angle deviation of $\theta = 5° \pm 3°$ from 60°. The big uncertainty arises from an intrinsic twist in the sample. This is further discussed in section 3.2.2, where SHG measurements on this specific sample are shown in Fig 3.5. Additional measurements on this sample are also discussed in section 4.3.1 and 4.3.2.

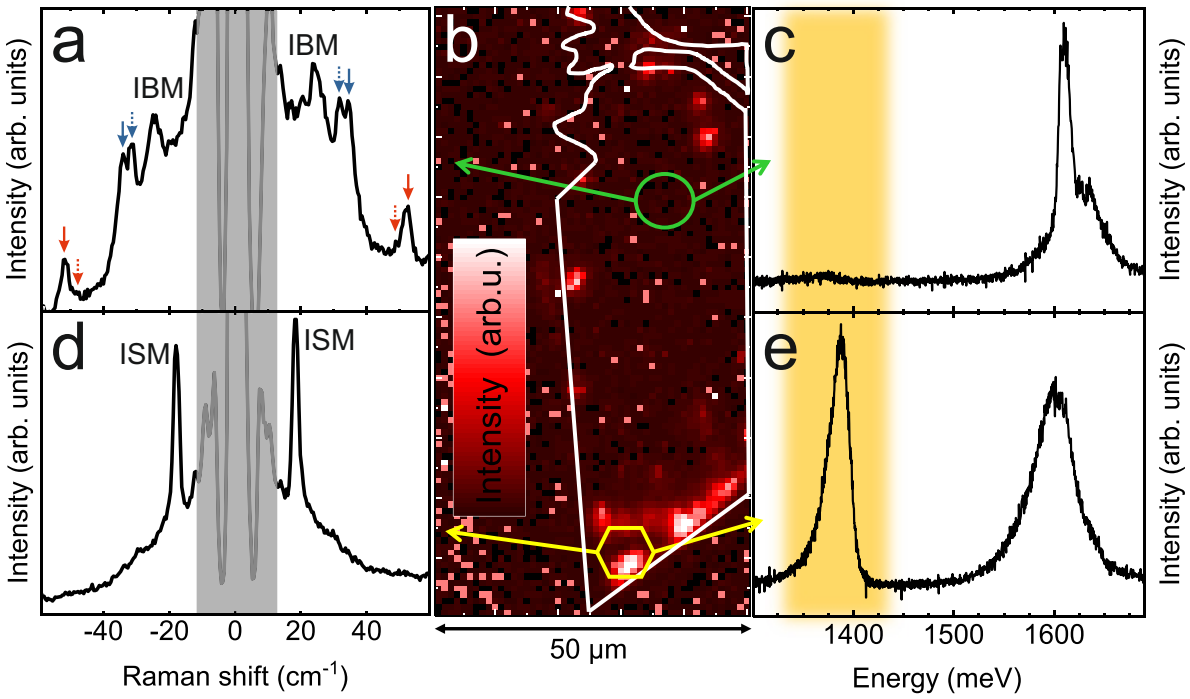

Figure 4.21 | a Unpolarized low-frequency Raman spectrum of the area indicated by the green circle. Moiré phonons are marked by arrows. **b** Spatially-resolved interlayer exciton PL intensity of the 55° ± 3° twist angle $MoSe_2$-WSe_2 heterostructure. **c** Low-temperature PL spectrum of the area indicated by the green circle. **d** Unpolarized low-frequency Raman spectrum of the area indicated by the yellow hexagon. **e** Low-temperature PL spectrum of the area indicated by the yellow hexagon. The yellow-shaded region marks the interlayer exciton.

To achieve a satisfying signal quality, integration times of at least 60 s are required. Therefore, the mapping of the sample was done by hand via recording single spectra at specific spots over the whole heterostructure area instead of an automated scan. We find two different regions. In one region low-frequency Raman measurements show moiré phonons, as depicted in Fig 4.21a. This phenomenon is already discussed in section 4.3.2 and allows us to identify this region as a moiré lattice with precise relative twist angle determination. In the other region we find a pronounced interlayer shear mode and no moiré phonons (see Fig 4.21d). Therefore, we attribute this region to atomic reconstruction, as discussed in section 4.3.1. These results are corroborated by low-temperature photoluminescence measurements of the interlayer exciton. Fig 4.21b shows a spatially-resolved PL intensity map of the interlayer exciton. Two exemplary spots for a region with moiré lattice (green circle) and atomic reconstruction (yellow hexagon) are shown. In the area which shows the ISM a twist angle $\theta < 4°$ and atomic reconstruction is expected. Due to the lattice rearrangement the interlayer exciton transition is direct in momentum space and therefore bright. This can be seen in Fig 4.21e. For the region where a moiré lattice forms, the interlayer exciton is momentum forbidden and therefore its PL strongly suppressed, which is shown in Fig 4.21c.

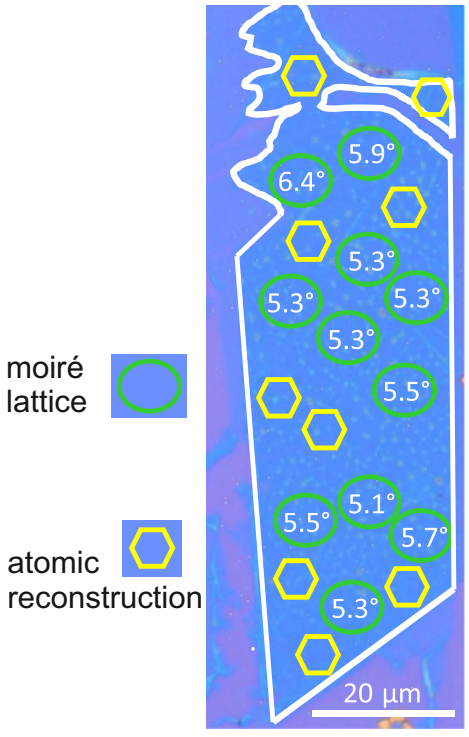

Figure 4.22 | Microscope image of the 55° ± 3° twist angle $MoSe_2$-WSe_2 heterostructure. Regions of atomic reconstruction (yellow hexagons) are marked. For regions associated to a moiré lattice (green circles) the relative twist angle is denoted.

Fig 4.22 presents the resulting map. We can identify different regions of atomic reconstruction via the interlayer shear mode. Furthermore, moiré phonons allow for a precise relative twist angle determination in regions with a moiré lattice, which show a twist angle variation of about 1° over the whole sample. Therefore, low-frequency Raman measurements can be used as a non-invasive, contactless method to characterize the lattice configuration of twisted homo- and heterobilayers.

Chapter 5

Conclusion

In the framework of this thesis van der Waals heterostructures are investigated by optical spectroscopy. The research on two-dimensional materials has been booming since the first successful exfoliation of graphene in 2004 [Nov04] and the discovery of many more van der Waals materials afterwards [Nov05]. In this work the main focus lies on $MoSe_2$-WSe_2 heterobilayers, but also $MoSe_2$ and WSe_2 homobilayers and hBN encapsulation are studied. The samples are investigated by Raman and photoluminescence (PL) spectroscopy. The relevant theoretical background and the experimental setups for this thesis are presented in chapters 2 and 3, respectively. In the following, a summary of the experimental results, which are presented in chapter 4, will be given.

In section 4.1 the air tightness of hBN encapsulation is investigated. Many van der Waals materials are sensitive to oxygen and degrade under ambient conditions. The oxidation is even enhanced by light, e.g. a laser [Li19]. Therefore, we systematically study the air tightness of hBN, which is commonly utilized as a protective layer. The van der Waals superconductor $NbSe_2$, which is unstable in air, is used to track the oxidation via Raman spectroscopy. We compare half-encapsulated samples and fully-encapsulated samples on a SiO_2 substrate. Half encapsulation denotes the capping of the sample with hBN from the top, while full encapsulation implies the protection of the sample from the top and the bottom by two hBN layers. We observe a degradation of the half-encapsulated sample by photooxidation after two days in air. The measurements on the fully-encapsulated sample show no degradation of the $NbSe_2$ and verify the air tightness of full hBN encapsulation. For a sufficient protection in ambient atmosphere, samples should either be fully-encapsulated or always be kept in an oxygen free environment.

In section 4.2 interlayer excitons (ILEs) are investigated by PL spectroscopy in high magnetic fields. We identify three different ILEs in aligned $MoSe_2$-WSe_2 heterostructures. For misaligned bilayers with a twist angle $\theta \neq 0°/60°$ no ILE PL is visible. Only for atomically reconstructed samples with twist angles close to 0° (R-type) or 60° (H-type) ILEs emerge. ILE-1 appears in H-type structures and features an energetic position of about 1400 meV and a g factor of about -15. ILE-2 only occurs in R-type heterostructures and exhibits a broader spectral linewidth than ILE-1, an energetic position of about 1360 meV and a g factor of about $+3.5$. ILE-3 appears in conjunction with ILE-2 and features an energetic position of about 1400 meV, a g factor of $g < 1$ and a lower intensity than ILE-1 and ILE-2. Therefore, we can distinguish between H- and R-type stacking by the distinct features of the ILEs. We assign ILE-1 to the spin-conserving transition of the H_h^X stacking and ILE-2 to the spin-conserving transition of the R_h^X configuration at the K point of the Brillouin zone. For ILE-3 we propose an indirect transition from Γ to $\Sigma^{\pm}$. The assignment of the transition is based on the experimental results in conjunction with theoretical calculations provided by our collaboration partners.

For high magnetic fields a yet unexplained anomaly occurs. We report a nonlinear behaviour of the valley splitting at about 24 T for ILE-1 in H-type samples and ILE-2 in R-type samples. Since the g factors for ILE-1 and ILE-2 are very different, this behaviour cannot be explained by a resonant tuning of, e.g. the ILE valley splitting, or a phonon resonance. For ILE-3 we observe a negative quadratic shift with increasing magnetic field. While ILE-1 and ILE-2 show an expected positive diamagnetic shift, ILE-3 shifts in the opposite direction. This effect is even stronger in hBN-encapsulated samples. To explain and understand the physical origin of these effects further experiments and theoretical studies are required.

Additionally, the temporal dynamics of the ILE valley polarization in high magnetic fields are studied. We find an initial polarization for all ILEs, that relaxes to its final value on a timescale of about 100 ns. The results can be explained by the magnitude of the g factor and the formation of the respective ILEs. ILE-1 features an initial positive polarization that increases over time. The initial polarization is adopted from the intralayer excitons. They exhibit a g factor of about -4 and the corresponding positive polarization is transferred by the formation of ILEs. Since the absolute value of the g factor of ILE-1 is far higher, the valley polarization rises. The measured circular polarization of ILE-2 starts at an initial positive value and declines down to a negative value

of -40%. ILE-2 is assigned to the R_h^X stacking configuration with a g factor of about $+6$. Nevertheless, it is formed by ultrafast charge transfer from the intralayer excitons to the R_h^h configuration with a g factor of about -6 and subsequent relaxation to the R_h^X stacking. At the beginning, the measurement shows a positive polarization corresponding to the R_h^h ILEs. As the charges relax to the R_h^X configuration the polarization reverses to negative values. ILE-3 features an initial positive polarization, which slowly decays to zero. The initial polarization stems from the intralayer excitons and due to the low g factor $g < 1$ the valley polarization of ILE-3 declines to zero. In the field of valleytronics ILEs are a promising candidate for future devices. The long lifetime of the valley polarization is a crucial prerequisite for the construction of prototypes that utilize the valley pseudospin. Therefore, it is important to understand the physical origin of the valley polarization.

In section 4.3 twisted bilayers are investigated via Raman spectroscopy. For these experiments a twist angle series of $MoSe_2$, WSe_2 and $MoSe_2$-WSe_2 bilayers has been fabricated. Recently it was shown, that these structures either atomically reconstruct ($\theta \approx 0°/60°$) or form a moiré lattice ($\theta \neq 0°/60°$), depending on the twist angle θ [Ros20, Wes20]. Raman spectroscopy is a unique tool to study artificial bilayers. On the one hand, low-frequency Raman scattering provides new insight by measuring the shear and breathing mode. These interlayer modes are strongly dependent on the twist angle and corresponding lattice rearrangements. On the other hand, moiré phonons emerge. These Raman modes occur due to the backfolding of acoustic phonons in the moiré superlattice and are therefore sensitive to the moiré period and the twist angle. We find atomic reconstruction for a twist angle deviation $\delta < 4°$ from $0°/60°$. In misaligned samples a moiré lattice forms.

For $MoSe_2$-WSe_2 heterostructures the interlayer shear mode (ISM) only occurs in atomically reconstructed samples. We observe a difference in intensity and energetic position of the ISM of H-type and R-type heterostructures. For H-type bilayers the Raman shift of the ISM is at $(18.0 \pm 0.1)\,\mathrm{cm}^{-1}$, while for R-type structures the ISM is at $(17.4 \pm 0.1)\,\mathrm{cm}^{-1}$. The intensity of the ISM is more pronounced in H-type heterostructures and in misaligned bilayers the ISM is not visible. These results are confirmed for hBN-encapsulated samples. Therefore, low-frequency Raman scattering provides a non-invasive, contactless method to identify the stacking configuration of encapsulated and non-encapsulated heterostructures. The Raman spectra of H-type bilayers indicate a dependence of the ISM intensity on the twist angle. To validate this effect a larger

number of samples and further measurements are required.

For misaligned bilayers a moiré pattern emerges. This introduces a new periodicity, which enables backscattering of the acoustic phonons. Therefore, these folded acoustic phonons corresponding to non-zero wavevectors can be measured by Raman spectroscopy and are called moiré phonons. The measurements show longitudinal and transversal folded acoustic phonons, whose energetic position is dependent on the moiré period and the twist angle. By comparing the moiré phonons of $MoSe_2$ and WSe_2 homobilayers to the calculated phonon dispersion, we find very good agreement between theory and experiment. For $MoSe_2$-WSe_2 heterostructures longitudinal and transversal folded acoustic phonons of both, $MoSe_2$ and WSe_2, are measured. The relative twist angle at the exact position of the measurement ca be determined precisely via the calculated phonon dispersions.

The results obtained from the measurements of the moiré phonons are corroborated by the interlayer breathing mode (IBM) in WSe_2 homobilayers. In contrast to the ISM, the IBM does not vanish in misaligned structures but shows a dependency on the twist angle similar to the moiré period. Via hyperspectral Raman imaging a map of a WSe_2 homobilayer sample with a twist angle of $5° \pm 1°$ is generated. We identify different regions that are distinguishable by the IBM and the moiré phonons. One bilayer region shows no IBM and no moiré phonons, which is attributed to loose contact between the layers. The second region manifests an IBM at higher frequencies and no moiré phonons. We assign this behaviour to atomic reconstruction. The third region exhibits both, the IBM and moiré phonons and is attributed to the formation of a moiré lattice. We report an intrinsic twist in the third region, which is mapped via the phonon frequencies.

Combining the measurement results of the ISM, moiré phonons and PL experiments we map an H-type $MoSe_2$-WSe_2 heterostructure with a twist angle deviation of $5° \pm 3°$ from 60°. The uncertainty of the twist angle stems from an intrinsic twist of the bilayer and the error of the second harmonic generation (SHG) measurements. This sample is particularly interesting because the threshold of atomic reconstruction lies in its twist angle range. Over the whole sample area we identify two different regions. In one region we observe moiré phonons and the IBM. Therefore, we assign this region to the formation of a moiré lattice. The relative twist angle is determined precisely via the moiré phonon frequency. In this region no ILE PL is visible due to the momentum mismatch in misaligned structures. In the other region we observe only the ISM in Raman measurements. Therefore, in this region atomic reconstruction takes place. Due to the rearrangement of the lattices the ILE is direct in reciprocal space and its PL can thus be measured in region two. This example shows the applicability of the method. Low-

frequency Raman measurements are a non-invasive, powerful tool to locally characterize the lattice configuration of twisted homo- and heterobilayers.

In conclusion, this work provides new insight into the physics of interlayer excitons. Especially the spatial separation of electrons and holes and the long lifetimes make them a promising platform for future applications and devices. Therefore, it is important to investigate the physical origin of the interlayer exciton transition and the corresponding valley polarization. The conducted experiments improve the understanding but also raise new questions. Furthermore, low-frequency Raman spectroscopy of the interlayer shear mode and moiré phonons presents a new method to characterize twisted bilayers. Via hyperspectral Raman imaging regions of atomic reconstruction or the formation of a moiré lattice can be determined. This is an essential information regarding twisted bilayers. Moreover, these structures demonstrate interesting physical phenomena like the aforementioned interlayer excitons, moiré phonons, moiré excitons and electronic phase transitions. Therefore, Raman spectroscopy provides a non-invasive, contactless technique with a broad area of application.

Bibliography

[Aiv15] G. Aivazian, Z. Gong, A. M. Jones, R. L. Chu, J. Yan, D. G. Mandrus, C. Zhang, D. Cobden, W. Yao, and X. Xu, *Magnetic control of valley pseudospin in monolayer WSe_2*, Nature Physics **11**, 148 (2015).

[Ald13] J. S. Alden, A. W. Tsen, P. Y. Huang, R. Hovden, L. Brown, J. Park, D. A. Muller, and P. L. McEuen, *Strain solitons and topological defects in bilayer graphene*, Proceedings of the National Academy of Sciences of the United States of America **110**, 11256 (2013).

[Ale19] E. M. Alexeev, D. A. Ruiz-Tijerina, M. Danovich, M. J. Hamer, D. J. Terry, P. K. Nayak, S. Ahn, S. Pak, J. Lee, J. I. Sohn, M. R. Molas, M. Koperski, K. Watanabe, T. Taniguchi, K. S. Novoselov, R. V. Gorbachev, H. S. Shin, V. I. Fal'ko, and A. I. Tartakovskii, *Resonantly hybridized excitons in moiré superlattices in van der Waals heterostructures*, Nature **567**, 81 (2019).

[Ali14] N. Alidoust, G. Bian, S. Y. Xu, R. Sankar, M. Neupane, C. Liu, I. Belopolski, D. X. Qu, J. D. Denlinger, F. C. Chou, and M. Z. Hasan, *Observation of monolayer valence band spin-orbit effect and induced quantum well states in MOX_2*, Nature Communications **5** (2014).

[And60] R. L. Anderson, *Germanium-Gallium Arsenide Heterojunctions*, IBM Journal of Research and Development **4**, 283 (1960).

[Aro17] A. Arora, M. Drüppel, R. Schmidt, T. Deilmann, R. Schneider, M. R. Molas, P. Marauhn, S. Michaelis De Vasconcellos, M. Potemski, M. Rohlfing, and R. Bratschitsch, *Interlayer excitons in a bulk van der Waals semiconductor*, Nature Communications **8** (2017).

[Aro19] A. Arora, M. Koperski, A. Slobodeniuk, K. Nogajewski, R. Schmidt, R. Schneider, M. R. Molas, S. M. De Vasconcellos, R. Bratschitsch, and M. Potemski, *Zeeman spectroscopy of excitons and hybridization of electronic states in few-layer WSe_2, $MoSe_2$ and $MoTe_2$*, 2D Materials **6** (2019).

[Ash17] M. Ashton, J. Paul, S. B. Sinnott, and R. G. Hennig, *Topology-Scaling Identification of Layered Solids and Stable Exfoliated 2D Materials*, Physical Review Letters **118**, 1 (2017).

[Bis11] R. Bistritzer and A. H. MacDonald, *Moiré bands in twisted double-layer graphene*, Proceedings of the National Academy of Sciences of the United States of America **108**, 12233 (2011).

[Boy20] R. Boyd, *Nonlinear Optics*, Academic Press (2020).

[Bro72] R. A. Bromley, R. B. Murray, and A. D. Yoffe, *The band structures of some transition metal dichalcogenides. III. Group VIA: trigonal prism materials*, Journal of Physics C: Solid State Physics **5**, 759 (1972).

[Cad17] F. Cadiz, E. Courtade, C. Robert, G. Wang, Y. Shen, H. Cai, T. Taniguchi, K. Watanabe, H. Carrere, D. Lagarde, M. Manca, T. Amand, P. Renucci, S. Tongay, X. Marie, and B. Urbaszek, *Excitonic linewidth approaching the homogeneous limit in MoS_2-based van der Waals heterostructures*, Physical Review X **7**, 1 (2017).

[Cao12] T. Cao, G. Wang, W. Han, H. Ye, C. Zhu, J. Shi, Q. Niu, P. Tan, E. Wang, B. Liu, and J. Feng, *Valley-selective circular dichroism of monolayer molybdenum disulphide*, Nature Communications **3** (2012).

[Cao15] Y. Cao, A. Mishchenko, G. L. Yu, E. Khestanova, A. P. Rooney, E. Prestat, A. V. Kretinin, P. Blake, M. B. Shalom, C. Woods, J. Chapman, G. Balakrishnan, I. V. Grigorieva, K. S. Novoselov, B. A. Piot, M. Potemski, K. Watanabe, T. Taniguchi, S. J. Haigh, A. K. Geim, and R. V. Gorbachev, *Quality Heterostructures from Two-Dimensional Crystals Unstable in Air by Their Assembly in Inert Atmosphere*, Nano Letters **15**, 4914 (2015).

[Cao18] Y. Cao, V. Fatemi, S. Fang, K. Watanabe, T. Taniguchi, E. Kaxiras, and P. Jarillo-Herrero, *Unconventional superconductivity in magic-angle graphene superlattices*, Nature **556**, 43 (2018).

[Car17] S. Carr, D. Massatt, S. Fang, P. Cazeaux, M. Luskin, and E. Kaxiras, *Twistronics: Manipulating the electronic properties of two-dimensional layered structures through their twist angle*, Physical Review B **95**, 1 (2017).

[Car18] S. Carr, D. Massatt, S. B. Torrisi, P. Cazeaux, M. Luskin, and E. Kaxiras, *Relaxation and domain formation in incommensurate two-dimensional heterostructures*, Physical Review B **98**, 1 (2018).

[Cas16] G. Cassabois, P. Valvin, and B. Gil, *Hexagonal boron nitride is an indirect bandgap semiconductor*, Nature Photonics **10**, 262 (2016).

[CG14] A. Castellanos-Gomez, M. Buscema, R. Molenaar, V. Singh, L. Janssen, H. S. Van Der Zant, and G. A. Steele, *Deterministic transfer of two-dimensional materials by all-dry viscoelastic stamping*, 2D Materials **1**, 1 (2014).

[Che14] A. Chernikov, T. C. Berkelbach, H. M. Hill, A. Rigosi, Y. Li, O. B. Aslan, D. R. Reichman, M. S. Hybertsen, and T. F. Heinz, *Exciton binding energy and nonhydrogenic Rydberg series in monolayer WS_2*, Physical Review Letters **113**, 1 (2014).

[Che20] X. Chen, C. Liu, and S. Mao, *Environmental Analysis with 2D Transition-Metal Dichalcogenide-Based Field-Effect Transistors*, Nano-Micro Letters **12**, 95 (2020).

[Cho20] M. Choi, S. R. Bae, L. Hu, A. T. Hoang, S. Y. Kim, and J. H. Ahn, *Full-color active-matrix organic light-emitting diode display on human skin based on a large-Area MoS_2 backplane*, Science Advances **6**, 1 (2020).

[Cho21] J. Choi, M. Florian, A. Steinhoff, D. Erben, K. Tran, D. S. Kim, L. Sun, J. Quan, R. Claassen, S. Majumder, J. A. Hollingsworth, T. Taniguchi, K. Watanabe, K. Ueno, A. Singh, G. Moody, F. Jahnke, and X. Li, *Twist Angle-Dependent Interlayer Exciton Lifetimes in van der Waals Heterostructures*, Physical Review Letters **126**, 47401 (2021).

[Cia19] A. Ciarrocchi, D. Unuchek, A. Avsar, K. Watanabe, T. Taniguchi, and A. Kis, *Polarization switching and electrical control of interlayer excitons in two-dimensional van der Waals heterostructures*, Nature Photonics **13**, 131 (2019).

[Cou17] E. Courtade, M. Semina, M. Manca, M. M. Glazov, C. Robert, F. Cadiz, G. Wang, T. Taniguchi, K. Watanabe, M. Pierre, W. Escoffier, E. L. Ivchenko,

P. Renucci, X. Marie, T. Amand, and B. Urbaszek, *Charged excitons in monolayer WSe_2: Experiment and theory*, Physical Review B **96**, 1 (2017).

[Dal15] S. Dal Conte, F. Bottegoni, E. A. Pogna, D. De Fazio, S. Ambrogio, I. Bargigia, C. D'Andrea, A. Lombardo, M. Bruna, F. Ciccacci, A. C. Ferrari, G. Cerullo, and M. Finazzi, *Ultrafast valley relaxation dynamics in monolayer MoS_2 probed by nonequilibrium optical techniques*, Physical Review B - Condensed Matter and Materials Physics **92**, 1 (2015).

[Dea10] C. R. Dean, A. F. Young, I. Meric, C. Lee, L. Wang, S. Sorgenfrei, K. Watanabe, T. Taniguchi, P. Kim, K. L. Shepard, and J. Hone, *Boron nitride substrates for high-quality graphene electronics*, Nature Nanotechnology **5**, 722 (2010).

[Dei20] T. Deilmann, P. Krüger, and M. Rohlfing, *Ab Initio Studies of Exciton g Factors: Monolayer Transition Metal Dichalcogenides in Magnetic Fields*, Physical Review Letters **124**, 226402 (2020).

[Del20] A. Delhomme, D. Vaclavkova, A. Slobodeniuk, M. Orlita, M. Potemski, D. M. Basko, K. Watanabe, T. Taniguchi, D. Mauro, C. Barreteau, E. Giannini, A. F. Morpurgo, N. Ubrig, and C. Faugeras, *Flipping exciton angular momentum with chiral phonons in $MoSe_2/WSe_2$ heterobilayers*, 2D Materials **7**, 041002 (2020).

[Dic23] R. G. Dickinson and L. Pauling, *The crystal structure of molybdenite*, Journal of the American Chemical Society **45**, 1466 (1923).

[Ena20] V. V. Enaldiev, V. Zólyomi, C. Yelgel, S. J. Magorrian, and V. I. Fal'ko, *Stacking Domains and Dislocation Networks in Marginally Twisted Bilayers of Transition Metal Dichalcogenides*, Physical Review Letters **124**, 1 (2020).

[Fan14] H. Fang, C. Battaglia, C. Carraro, S. Nemsak, B. Ozdol, J. S. Kang, H. A. Bechtel, S. B. Desai, F. Kronast, A. A. Unal, G. Conti, C. Conlon, G. K. Palsson, M. C. Martin, A. M. Minor, C. S. Fadley, E. Yablonovitch, R. Maboudian, and A. Javey, *Strong interlayer coupling in van der Waals heterostructures built from single-layer chalcogenides*, Proceedings of the National Academy of Sciences of the United States of America **111**, 6198 (2014).

[Fav15] A. Favron, E. Gaufrès, F. Fossard, A. L. Phaneuf-Laheureux, N. Y. Tang, P. L. Lévesque, A. Loiseau, R. Leonelli, S. Francoeur, and R. Martel, *Photooxidation and quantum confinement effects in exfoliated black phosphorus*, Nature Materials **14**, 826 (2015).

[För20] J. Förste, N. V. Tepliakov, S. Y. Kruchinin, J. Lindlau, V. Funk, M. Förg, K. Watanabe, T. Taniguchi, A. S. Baimuratov, and A. Högele, *Exciton g-factors in monolayer and bilayer WSe_2 from experiment and theory*, Nature Communications **11**, 1 (2020).

[Gei13] A. K. Geim and I. V. Grigorieva, *Van der Waals heterostructures*, Nature **499**, 419 (2013).

[Gil18] R. Gillen and J. Maultzsch, *Interlayer excitons in $MoSe_2/WSe_2$ heterostructures from first principles*, Physical Review B **97**, 1 (2018).

[Guo16] Y. Guo, C. Liu, Q. Yin, C. Wei, S. Lin, T. B. Hoffman, Y. Zhao, J. H. Edgar, Q. Chen, S. P. Lau, J. Dai, H. Yao, H. S. Wong, and Y. Chai, *Distinctive in-Plane Cleavage Behaviors of Two-Dimensional Layered Materials*, ACS Nano **10**, 8980 (2016).

[He16] R. He, J. Van Baren, J. A. Yan, X. Xi, Z. Ye, G. Ye, I. H. Lu, S. M. Leong, and C. H. Lui, *Interlayer breathing and shear modes in $NbSe_2$ atomic layers*, 2D Materials **3**, 1 (2016).

[Her12] K. Hermann, *Periodic overlayers and moiré patterns: Theoretical studies of geometric properties*, Journal of Physics Condensed Matter **24** (2012).

[Hic64] W. T. Hicks, *Semiconducting Behavior of Substituted Tungsten Diselenide and Its Analogues*, Journal of The Electrochemical Society **111**, 1058 (1964).

[Hoa20] A. T. Hoang, A. K. Katiyar, H. Shin, N. Mishra, S. Forti, C. Coletti, and J. H. Ahn, *Epitaxial growth of wafer-scale molybdenum disulfide/graphene heterostructures by metal-organic vapor-phase epitaxy and their application in photodetectors*, ACS Applied Materials and Interfaces **12**, 44335 (2020).

[Hol76] J. A. Holy, M. V. Klein, W. L. McMillan, and S. F. Meyer, *Raman-Active Lattice Vibrations of the Commensurate Superlattic in 2H-$TaSe_2$*, Physical Review Letters **37**, 1145 (1976).

[Hol19] J. Holler, L. Bauriedl, T. Korn, A. Seitz, F. Özyigit, M. Eichinger, C. Schüller, K. Watanabe, T. Taniguchi, C. Strunk, and N. Paradiso, *Air tightness of hBN encapsulation and its impact on Raman spectroscopy of van der Waals materials*, 2D Materials **7**, 015012 (2019).

[Hol20] J. Holler, S. Meier, M. Kempf, P. Nagler, K. Watanabe, T. Taniguchi, T. Korn, and C. Schüller, *Low-frequency Raman scattering in WSe_2 - $MoSe_2$ heterobilayers: Evidence for atomic reconstruction*, Applied Physics Letters **117** (2020).

[Hol21a] J. Holler, M. Selig, F. Katsch, M. Kempf, P. Nagler, J. Zipfel, M. V. Ballottin, A. A. Mitioglu, A. Chernikov, P. C. Christianen, C. Schüller, A. Knorr, and T. Korn, *Preliminary: Valley polarization dynamics of the interlayer exciton in $MoSe_2$-WSe_2 heterostructures*, in preparation (2021).

[Hol21b] J. Holler, T. Woźniak, M. Kempf, M. Högen, P. Nagler, J. Zipfel, M. V. Ballottin, A. A. Mitioglu, A. Chernikov, T. Taniguchi, K. Watanabe, P. C. Christianen, C. Schüller, M. M. Glazov, J. Kunstmann, T. Korn, and A. Chaves, *Negative quadratic magnetic shift of interlayer excitons in van der Waals heterostructures*, in preparation (2021).

[Hon14] X. Hong, J. Kim, S. F. Shi, Y. Zhang, C. Jin, Y. Sun, S. Tongay, J. Wu, Y. Zhang, and F. Wang, *Ultrafast charge transfer in atomically thin MoS_2/WS_2 heterostructures*, Nature Nanotechnology **9**, 682 (2014).

[Hua14] S. Huang, X. Ling, L. Liang, J. Kong, H. Terrones, V. Meunier, and M. S. Dresselhaus, *Probing the interlayer coupling of twisted bilayer MoS_2 using photoluminescence spectroscopy*, Nano Letters **14**, 5500 (2014).

[Hua16] S. Huang, L. Liang, X. Ling, A. A. Puretzky, D. B. Geohegan, B. G. Sumpter, J. Kong, V. Meunier, and M. S. Dresselhaus, *Low-Frequency Interlayer Raman Modes to Probe Interface of Twisted Bilayer MoS_2*, Nano Letters **16**, 1435 (2016).

[Hua17] B. Huang, G. Clark, E. Navarro-Moratalla, D. R. Klein, R. Cheng, K. L. Seyler, D. Zhong, E. Schmidgall, M. A. McGuire, D. H. Cobden, W. Yao, D. Xiao, P. Jarillo-Herrero, and X. Xu, *Layer-dependent ferromagnetism in a van der Waals crystal down to the monolayer limit*, Nature **546**, 270 (2017).

[Jam63] P. B. James and M. T. Lavik, *The crystal structure of $MoSe_2$*, Acta Crystallographica **16**, 1183 (1963).

[Jia18] C. Jiang, W. Xu, A. Rasmita, Z. Huang, K. Li, Q. Xiong, and W. Gao, *Microsecond dark-exciton valley polarization memory in two-dimensional heterostructures*, Nature Communications **9**, 753 (2018).

[Jin17] C. Jin, J. Kim, J. Suh, Z. Shi, B. Chen, X. Fan, M. Kam, K. Watanabe, T. Taniguchi, S. Tongay, A. Zettl, J. Wu, and F. Wang, *Interlayer electron-phonon coupling in WSe_2/hBN heterostructures*, Nature Physics **13**, 127 (2017).

[Jin19] C. Jin, E. C. Regan, A. Yan, M. Iqbal Bakti Utama, D. Wang, S. Zhao, Y. Qin, S. Yang, Z. Zheng, S. Shi, K. Watanabe, T. Taniguchi, S. Tongay, A. Zettl, and F. Wang, *Observation of moiré excitons in WSe_2/WS_2 heterostructure superlattices*, Nature **567**, 76 (2019).

[Kad12] E. S. Kadantsev and P. Hawrylak, *Electronic structure of a single MoS_2 monolayer*, Solid State Communications **152**, 909 (2012).

[Kan13] J. Kang, S. Tongay, J. Zhou, J. Li, and J. Wu, *Band offsets and heterostructures of two-dimensional semiconductors*, Applied Physics Letters **102** (2013).

[Kar19] O. Karni, E. Barré, S. C. Lau, R. Gillen, E. Y. Ma, B. Kim, K. Watanabe, T. Taniguchi, J. Maultzsch, K. Barmak, R. H. Page, and T. F. Heinz, *Infrared Interlayer Exciton Emission in MoS_2/WSe_2 Heterostructures*, Physical Review Letters **123**, 1 (2019).

[Kim16] K. Kim, M. Yankowitz, B. Fallahazad, S. Kang, H. C. Movva, S. Huang, S. Larentis, C. M. Corbet, T. Taniguchi, K. Watanabe, S. K. Banerjee, B. J. Leroy, and E. Tutuc, *Van der Waals Heterostructures with High Accuracy Rotational Alignment*, Nano Letters **16**, 1989 (2016).

[Kor15] A. Kormányos, G. Burkard, M. Gmitra, J. Fabian, V. Zólyomi, N. D. Drummond, and V. Fal'ko, *k.p theory for two-dimensional transition metal dichalcogenide semiconductors*, 2D Materials **2**, 022001 (2015).

[Kuc11] A. Kuc, N. Zibouche, and T. Heine, *Influence of quantum confinement on the electronic structure of the transition metal sulfide TS_2*, Physical Review B **83**, 245213 (2011).

[Kum15] H. Kumar, D. Er, L. Dong, J. Li, and V. B. Shenoy, *Elastic deformations in 2D van der waals heterostructures and their impact on optoelectronic properties: Predictions from a multiscale computational approach*, Scientific Reports **5**, 1 (2015).

[Kun18] J. Kunstmann, F. Mooshammer, P. Nagler, A. Chaves, F. Stein, N. Paradiso, G. Plechinger, C. Strunk, C. Schüller, G. Seifert, D. R. Reichman, and T. Korn,

Momentum-space indirect interlayer excitons in transition-metal dichalcogenide van der Waals heterostructures, Nature Physics **14**, 801 (2018).

[Lam20] M. Lamparski, B. Van Troeye, and V. Meunier, *Soliton signature in the phonon spectrum of twisted bilayer graphene*, 2D Materials **7**, 025050 (2020).

[Leb09] S. Lebègue and O. Eriksson, *Electronic structure of two-dimensional crystals from ab initio theory*, Physical Review B **79**, 115409 (2009).

[Li13] Y. Li, Y. Rao, K. F. Mak, Y. You, S. Wang, C. R. Dean, and T. F. Heinz, *Probing symmetry properties of few-layer MoS_2 and h-BN by optical second-harmonic generation*, Nano Letters **13**, 3329 (2013).

[Li14] Y. Li, A. Chernikov, X. Zhang, A. Rigosi, H. M. Hill, A. M. van der Zande, D. A. Chenet, E.-M. Shih, J. Hone, and T. F. Heinz, *Measurement of the optical dielectric function of monolayer transition-metal dichalcogenides: MoS_2, $MoSe_2$, WS_2, and WSe_2*, Physical Review B **90**, 205422 (2014).

[Li19] Q. Li, Q. Zhou, L. Shi, Q. Chen, and J. Wang, *Recent advances in oxidation and degradation mechanisms of ultrathin 2D materials under ambient conditions and their passivation strategies*, Journal of Materials Chemistry A **7**, 4291 (2019).

[Lia13] Y. Liang, S. Huang, R. Soklaski, and L. Yang, *Quasiparticle band-edge energy and band offsets of monolayer of molybdenum and tungsten chalcogenides*, Applied Physics Letters **103** (2013).

[Lia17] L. Liang, J. Zhang, B. G. Sumpter, Q. H. Tan, P. H. Tan, and V. Meunier, *Low-Frequency Shear and Layer-Breathing Modes in Raman Scattering of Two-Dimensional Materials*, ACS Nano **11**, 11777 (2017).

[Lin18] M. L. Lin, Q. H. Tan, J. B. Wu, X. S. Chen, J. H. Wang, Y. H. Pan, X. Zhang, X. Cong, J. Zhang, W. Ji, P. A. Hu, K. H. Liu, and P. H. Tan, *Moiré phonons in twisted bilayer MoS_2*, ACS Nano **12**, 8770 (2018).

[Lin21] K.-Q. Lin, J. Holler, J. M. Bauer, M. Scheuck, B. Peng, T. Korn, S. Bange, J. M. Lupton, and C. Schüller, *Large-scale mapping of moiré superlattices by hyperspectral Raman imaging*, in press (2021).

[Lui15] C. H. Lui, Z. Ye, C. Ji, K.-C. Chiu, C.-T. Chou, T. I. Andersen, C. Means-Shively, H. Anderson, J.-M. Wu, T. Kidd, Y.-H. Lee, and R. He, *Observation*

of interlayer phonon modes in van der Waals heterostructures, Physical Review B **91**, 165403 (2015).

[Ma18] P. Ma, N. Flöry, Y. Salamin, B. Baeuerle, A. Emboras, A. Josten, T. Taniguchi, K. Watanabe, L. Novotny, and J. Leuthold, *Fast $MoTe_2$ Waveguide Photodetector with High Sensitivity at Telecommunication Wavelengths*, ACS Photonics **5**, 1846 (2018).

[Mai14] C. Mai, A. Barrette, Y. Yu, Y. G. Semenov, K. W. Kim, L. Cao, and K. Gundogdu, *Many-body effects in valleytronics: Direct measurement of valley lifetimes in single-layer MoS_2*, Nano Letters **14**, 202 (2014).

[Mai20] I. Maity, M. H. Naik, P. K. Maiti, H. R. Krishnamurthy, and M. Jain, *Phonons in twisted transition-metal dichalcogenide bilayers: Ultrasoft phasons and a transition from a superlubric to a pinned phase*, Physical Review Research **2**, 13335 (2020).

[Mak10] K. F. Mak, C. Lee, J. Hone, J. Shan, and T. F. Heinz, *Atomically thin MoS_2: A new direct-gap semiconductor*, Physical Review Letters **105**, 2 (2010).

[Mak12] K. F. Mak, K. He, J. Shan, and T. F. Heinz, *Control of valley polarization in monolayer MoS_2 by optical helicity*, Nature Nanotechnology **7**, 494 (2012).

[Mak13] K. F. Mak, K. He, C. Lee, G. H. Lee, J. Hone, T. F. Heinz, and J. Shan, *Tightly bound trions in monolayer MoS_2*, Nature Materials **12**, 207 (2013).

[Mak16] K. F. Mak and J. Shan, *Photonics and optoelectronics of 2D semiconductor transition metal dichalcogenides*, Nature Photonics **10**, 216 (2016).

[Mal13] L. M. Malard, T. V. Alencar, A. P. M. Barboza, K. F. Mak, and A. M. de Paula, *Observation of intense second harmonic generation from MoS_2 atomic crystals*, Physical Review B **87**, 201401 (2013).

[Mei05] M. A. Meitl, Z.-T. Zhu, V. Kumar, K. J. Lee, X. Feng, Y. Y. Huang, I. Adesida, R. G. Nuzzo, and J. A. Rogers, *Transfer printing by kinetic control of adhesion to an elastomeric stamp*, Nature Materials **5**, 33 (2005).

[Men20] L. Mennel, J. Symonowicz, S. Wachter, D. K. Polyushkin, A. J. Molina-Mendoza, and T. Mueller, *Ultrafast machine vision with 2D material neural network image sensors*, Nature **579**, 62 (2020).

[Mer19] P. Merkl, F. Mooshammer, P. Steinleitner, A. Girnghuber, K. Q. Lin, P. Nagler, J. Holler, C. Schüller, J. M. Lupton, T. Korn, S. Ovesen, S. Brem, E. Malic, and R. Huber, *Ultrafast transition between exciton phases in van der Waals heterostructures*, Nature Materials **18**, 691 (2019).

[Mil17] B. Miller, A. Steinhoff, B. Pano, J. Klein, F. Jahnke, A. Holleitner, and U. Wurstbauer, *Long-Lived Direct and Indirect Interlayer Excitons in van der Waals Heterostructures*, Nano Letters **17**, 5229 (2017).

[Mol19] M. R. Molas, A. O. Slobodeniuk, K. Nogajewski, M. Bartos, Bala, A. Babiński, K. Watanabe, T. Taniguchi, C. Faugeras, and M. Potemski, *Energy Spectrum of Two-Dimensional Excitons in a Nonuniform Dielectric Medium*, Physical Review Letters **123**, 1 (2019).

[Moo13] P. Moon and M. Koshino, *Optical absorption in twisted bilayer graphene*, Physical Review B **87**, 205404 (2013).

[Mou18] N. Mounet, M. Gibertini, P. Schwaller, D. Campi, A. Merkys, A. Marrazzo, T. Sohier, I. E. Castelli, A. Cepellotti, G. Pizzi, and N. Marzari, *Two-dimensional materials from high-throughput computational exfoliation of experimentally known compounds*, Nature Nanotechnology **13**, 246 (2018).

[Nag17a] P. Nagler, M. V. Ballottin, A. A. Mitioglu, F. Mooshammer, N. Paradiso, C. Strunk, R. Huber, A. Chernikov, P. C. Christianen, C. Schüller, and T. Korn, *Giant magnetic splitting inducing near-unity valley polarization in van der Waals heterostructures*, Nature Communications **8**, 1 (2017).

[Nag17b] P. Nagler, G. Plechinger, M. V. Ballottin, A. Mitioglu, S. Meier, N. Paradiso, C. Strunk, A. Chernikov, P. C. M. Christianen, C. Schüller, and T. Korn, *Interlayer exciton dynamics in a dichalcogenide monolayer heterostructure*, 2D Materials **4**, 025112 (2017).

[Nag18] P. Nagler, *Exciton spectroscopy of van der Waals heterostructures*, doctoral thesis, Universität Regensburg (2018).

[Nay17] P. K. Nayak, Y. Horbatenko, S. Ahn, G. Kim, J. U. Lee, K. Y. Ma, A. R. Jang, H. Lim, D. Kim, S. Ryu, H. Cheong, N. Park, and H. S. Shin, *Probing Evolution of Twist-Angle-Dependent Interlayer Excitons in $MoSe_2/WSe_2$ van der Waals Heterostructures*, ACS Nano **11**, 4041 (2017).

[Ni19] G. X. Ni, H. Wang, B. Y. Jiang, L. X. Chen, Y. Du, Z. Y. Sun, M. D. Goldflam, A. J. Frenzel, X. M. Xie, M. M. Fogler, and D. N. Basov, *Soliton superlattices in twisted hexagonal boron nitride*, Nature Communications **10**, 1 (2019).

[Nov04] K. S. Novoselov, A. K. Geim, S. V. Morozov, D. Jiang, Y. Zhang, S. V. Dubonos, I. V. Grigorieva, and A. A. Firsov, *Electric Field Effect in Atomically Thin Carbon Films*, Science **306**, 666 (2004).

[Nov05] K. S. Novoselov, D. Jiang, F. Schedin, T. J. Booth, V. V. Khotkevich, S. V. Morozov, and A. K. Geim, *Two-dimensional atomic crystals*, Proceedings of the National Academy of Sciences **102**, 10451 (2005).

[Nov16] K. S. Novoselov, A. Mishchenko, A. Carvalho, and A. H. Castro Neto, *2D materials and van der Waals heterostructures*, Science **353** (2016).

[Pal15] M. Palummo, M. Bernardi, and J. C. Grossman, *Exciton Radiative Lifetimes in Two-Dimensional Transition Metal Dichalcogenides*, Nano Letters **15**, 2794 (2015).

[Par19] N. Paradiso, A.-T. Nguyen, K. Enzo Kloss, and C. Strunk, *Phase slip lines in superconducting few-layer $NbSe_2$ crystals*, 2D Materials **6**, 025039 (2019).

[Par20] S. Park, A. Lee, K. H. Choi, S. K. Hyeong, S. Bae, J. M. Hong, T. W. Kim, B. H. Hong, and S. K. Lee, *Layer-Selective Synthesis of MoS_2 and WS_2 Structures under Ambient Conditions for Customized Electronics*, ACS Nano **14**, 8485 (2020).

[Par21a] P. Parzefall, *Optical characterization of $MoSe_2$-WSe_2 heterobilayer lattices*, master thesis, Universität Regensburg (2021).

[Par21b] P. Parzefall, J. Holler, M. Scheuck, A. Beer, K.-Q. Lin, B. Peng, B. Monserrat, P. Nagler, M. Kempf, T. Korn, and C. Schüller, *Moiré phonons in twisted $MoSe_2$-WSe_2 heterobilayers and their correlation with interlayer excitons*, 2D Materials **8**, 035030 (2021).

[Pen16] B. Peng, H. Zhang, H. Shao, Y. Xu, X. Zhang, and H. Zhu, *Thermal conductivity of monolayer MoS_2, $MoSe_2$, and WS_2: Interplay of mass effect, interatomic bonding and anharmonicity*, RSC Advances **6**, 5767 (2016).

[Ple12] G. Plechinger, S. Heydrich, J. Eroms, D. Weiss, C. Schüller, and T. Korn, *Raman spectroscopy of the interlayer shear mode in few-layer MoS_2 flakes*, Applied Physics Letters **101**, 22 (2012).

[Ple16] G. Plechinger, P. Nagler, A. Arora, A. Granados Del Águila, M. V. Ballottin, T. Frank, P. Steinleitner, M. Gmitra, J. Fabian, P. C. Christianen, R. Bratschitsch, C. Schüller, and T. Korn, *Excitonic Valley Effects in Monolayer WS_2 under High Magnetic Fields*, Nano Letters **16**, 7899 (2016).

[Pur15] A. A. Puretzky, L. Liang, X. Li, K. Xiao, K. Wang, M. Mahjouri-Samani, L. Basile, J. C. Idrobo, B. G. Sumpter, V. Meunier, and D. B. Geohegan, *Low-Frequency Raman Fingerprints of Two-Dimensional Metal Dichalcogenide Layer Stacking Configurations*, ACS Nano **9**, 6333 (2015).

[Pur16] A. A. Puretzky, L. Liang, X. Li, K. Xiao, B. G. Sumpter, V. Meunier, and D. B. Geohegan, *Twisted $MoSe_2$ Bilayers with Variable Local Stacking and Interlayer Coupling Revealed by Low-Frequency Raman Spectroscopy*, ACS Nano **10**, 2736 (2016).

[Pür19] K. Pürckhauer, D. Kirpal, A. J. Weymouth, and F. J. Giessibl, *Analysis of Airborne Contamination on Transition Metal Dichalcogenides with Atomic Force Microscopy Revealing That Sulfur Is the Preferred Chalcogen Atom for Devices Made in Ambient Conditions*, ACS Applied Nano Materials **2**, 2593 (2019).

[Qua21] J. Quan, L. Linhart, M.-L. Lin, D. Lee, J. Zhu, C.-Y. Wang, W.-T. Hsu, J. Choi, J. Embley, C. Young, T. Taniguchi, K. Watanabe, C.-K. Shih, K. Lai, A. H. MacDonald, P.-H. Tan, F. Libisch, and X. Li, *Phonon renormalization in reconstructed MoS_2 moiré superlattices*, Nature Materials (2021).

[Raj19] A. Raja, L. Waldecker, J. Zipfel, Y. Cho, S. Brem, J. D. Ziegler, M. Kulig, T. Taniguchi, K. Watanabe, E. Malic, T. F. Heinz, T. C. Berkelbach, and A. Chernikov, *Dielectric disorder in two-dimensional materials*, Nature Nanotechnology **14**, 832 (2019).

[Riv15] P. Rivera, J. R. Schaibley, A. M. Jones, J. S. Ross, S. Wu, G. Aivazian, P. Klement, K. Seyler, G. Clark, N. J. Ghimire, J. Yan, D. G. Mandrus, W. Yao, and X. Xu, *Observation of long-lived interlayer excitons in monolayer $MoSe_2$-WSe_2 heterostructures*, Nature Communications **6**, 4 (2015).

[Riv16] P. Rivera, K. L. Seyler, H. Yu, J. R. Schaibley, J. Yan, D. G. Mandrus, W. Yao, and X. Xu, *Valley-polarized exciton dynamics in a 2D semiconductor heterostructure*, Science **351**, 688 (2016).

[Rob20] C. Robert, B. Han, P. Kapuscinski, A. Delhomme, C. Faugeras, T. Amand, M. R. Molas, M. Bartos, K. Watanabe, T. Taniguchi, B. Urbaszek, M. Potemski, and X. Marie, *Measurement of the spin-forbidden dark excitons in MoS_2 and $MoSe_2$ monolayers*, Nature Communications **11**, 1 (2020).

[Ros20] M. R. Rosenberger, H.-J. Chuang, M. Phillips, V. P. Oleshko, K. M. McCreary, S. V. Sivaram, C. S. Hellberg, and B. T. Jonker, *Twist Angle-Dependent Atomic Reconstruction and Moiré Patterns in Transition Metal Dichalcogenide Heterostructures*, ACS Nano **14**, 4550 (2020).

[Sai16] R. Saito, Y. Tatsumi, S. Huang, X. Ling, and M. S. Dresselhaus, *Raman spectroscopy of transition metal dichalcogenides*, Journal of Physics Condensed Matter **28**, 353002 (2016).

[Sch06] C. Schüller, *Inelastic Light Scattering of Semiconductor Nanostructures: Fundamentals and Recent Advances*, Springer-Verlag, Berlin Heidelberg (2006).

[Sch13] J. A. Schuller, S. Karaveli, T. Schiros, K. He, S. Yang, I. Kymissis, J. Shan, and R. Zia, *Orientation of luminescent excitons in layered nanomaterials*, Nature Nanotechnology **8**, 271 (2013).

[Sch16a] J. R. Schaibley, H. Yu, G. Clark, P. Rivera, J. S. Ross, K. L. Seyler, W. Yao, and X. Xu, *Valleytronics in 2D materials*, Nature Reviews Materials **1**, 1 (2016).

[Sch16b] R. Schmidt, A. Arora, G. Plechinger, P. Nagler, A. Granados Del Águila, M. V. Ballottin, P. C. Christianen, S. Michaelis De Vasconcellos, C. Schüller, T. Korn, and R. Bratschitsch, *Magnetic-Field-Induced Rotation of Polarized Light Emission from Monolayer WS_2*, Physical Review Letters **117**, 1 (2016).

[Sey19] K. L. Seyler, P. Rivera, H. Yu, N. P. Wilson, E. L. Ray, D. G. Mandrus, J. Yan, W. Yao, and X. Xu, *Signatures of moiré-trapped valley excitons in $MoSe_2/WSe_2$ heterobilayers*, Nature **567**, 66 (2019).

[Shk02] Y. P. Shkolnikov, E. P. De Poortere, E. Tutuc, and M. Shayegan, *Valley Splitting of AlAs Two-Dimensional Electrons in a Perpendicular Magnetic Field*, Physical Review Letters **89**, 2 (2002).

[Sig20] L. Sigl, F. Sigger, F. Kronowetter, J. Kiemle, J. Klein, K. Watanabe, T. Taniguchi, J. J. Finley, U. Wurstbauer, and A. W. Holleitner, *Signatures of a degenerate many-body state of interlayer excitons in a van der Waals heterostack*, Physical Review Research **2**, 1 (2020).

[Soo85] A. K. Sood, J. Menéndez, M. Cardona, and K. Ploog, *Resonance Raman Scattering by Confined LO and TO Phonons in GaAs-AlAs Superlattices*, Physical Review Letters **54**, 2111 (1985).

[Spl10] A. Splendiani, L. Sun, Y. Zhang, T. Li, J. Kim, C. Y. Chim, G. Galli, and F. Wang, *Emerging photoluminescence in monolayer MoS_2*, Nano Letters **10**, 1271 (2010).

[Ste15] A. Steinhoff, J. H. Kim, F. Jahnke, M. Rösner, D. S. Kim, C. Lee, G. H. Han, M. S. Jeong, T. O. Wehling, and C. Gies, *Efficient Excitonic Photoluminescence in Direct and Indirect Band Gap Monolayer MoS_2*, Nano Letters **15**, 6841 (2015).

[Sti16] A. V. Stier, K. M. McCreary, B. T. Jonker, J. Kono, and S. A. Crooker, *Exciton diamagnetic shifts and valley Zeeman effects in monolayer WS_2 and MoS_2 to 65 Tesla*, Nature Communications **7**, 1 (2016).

[Sti18] A. V. Stier, N. P. Wilson, K. A. Velizhanin, J. Kono, X. Xu, and S. A. Crooker, *Magnetooptics of Exciton Rydberg States in a Monolayer Semiconductor*, Physical Review Letters **120**, 1 (2018).

[Sun17] L. Sun, C. Chen, Q. Zhang, C. Sohrt, T. Zhao, G. Xu, J. Wang, D. Wang, K. Rossnagel, L. Gu, C. Tao, and L. Jiao, *Suppression of the Charge Density Wave State in Two-Dimensional 1T -$TiSe_2$ by Atmospheric Oxidation*, Angewandte Chemie International Edition **56**, 8981 (2017).

[Sur18] A. Surrente, Ł. Kłopotowski, N. Zhang, M. Baranowski, A. A. Mitioglu, M. V. Ballottin, P. C. Christianen, D. Dumcenco, Y. C. Kung, D. K. Maude, A. Kis, and P. Plochocka, *Intervalley Scattering of Interlayer Excitons in a $MoS_2/MoSe_2/MoS_2$ Heterostructure in High Magnetic Field*, Nano Letters **18**, 3994 (2018).

[Tak06] K. Takashina, Y. Ono, A. Fujiwara, Y. Takahashi, and Y. Hirayama, *Valley polarization in Si(100) at zero magnetic field*, Physical Review Letters **96**, 2 (2006).

[Tan04] P. H. Tan, D. Bougeard, G. Abstreiter, and K. Brunner, *Raman scattering of folded acoustic phonons in self-assembled Si/Ge dot superlattices*, Applied Physics Letters **84**, 2632 (2004).

[Tan07] T. Taniguchi and K. Watanabe, *Synthesis of high-purity boron nitride single crystals under high pressure by using Ba-BN solvent*, Journal of Crystal Growth **303**, 525 (2007).

[Tim82] G. Timp, B. Elman, R. Al-Jishi, and G. Dresselhaus, *Observation of superlattice-induced Raman modes in graphite-potassium-amalgam compounds*, Solid State Communications **44**, 987 (1982).

[Tra19] K. Tran, G. Moody, F. Wu, X. Lu, J. Choi, K. Kim, A. Rai, D. A. Sanchez, J. Quan, A. Singh, J. Embley, A. Zepeda, M. Campbell, T. Autry, T. Taniguchi, K. Watanabe, N. Lu, S. K. Banerjee, K. L. Silverman, S. Kim, E. Tutuc, L. Yang, A. H. MacDonald, and X. Li, *Evidence for moiré excitons in van der Waals heterostructures*, Nature **567**, 71 (2019).

[Uch14] K. Uchida, S. Furuya, J.-I. Iwata, and A. Oshiyama, *Atomic corrugation and electron localization due to Moiré patterns in twisted bilayer graphenes*, Physical Review B **90**, 155451 (2014).

[Uge16] M. M. Ugeda, A. J. Bradley, Y. Zhang, S. Onishi, Y. Chen, W. Ruan, C. Ojeda-Aristizabal, H. Ryu, M. T. Edmonds, H. Z. Tsai, A. Riss, S. K. Mo, D. Lee, A. Zettl, Z. Hussain, Z. X. Shen, and M. F. Crommie, *Characterization of collective ground states in single-layer $NbSe_2$*, Nature Physics **12**, 92 (2016).

[Van14] A. M. Van Der Zande, J. Kunstmann, A. Chernikov, D. A. Chenet, Y. You, X. Zhang, P. Y. Huang, T. C. Berkelbach, L. Wang, F. Zhang, M. S. Hybertsen, D. A. Muller, D. R. Reichman, T. F. Heinz, and J. C. Hone, *Tailoring the electronic structure in bilayer molybdenum disulfide via interlayer twist*, Nano Letters **14**, 3869 (2014).

[Ver70] J. L. Verble and T. J. Wieting, *Lattice mode degeneracy in MoS_2 and other layer compounds*, Physical Review Letters **25**, 362 (1970).

[Voß99] D. Voß, P. Krüger, A. Mazur, and J. Pollmann, *Atomic and electronic structure of WSe_2 from ab initio theory: Bulk crystal and thin film systems*, Physical Review B **60**, 14311 (1999).

[Wan13] L. Wang, I. Meric, P. Y. Huang, Q. Gao, Y. Gao, H. Tran, T. Taniguchi, K. Watanabe, L. M. Campos, D. A. Muller, J. Guo, P. Kim, J. Hone, K. L. Shepard, and C. R. Dean, *One-Dimensional Electrical Contact to a Two-Dimensional Material*, Science **342**, 614 (2013).

[Wan17] Z. Wang, L. Zhao, K. F. Mak, and J. Shan, *Probing the Spin-Polarized Electronic Band Structure in Monolayer Transition Metal Dichalcogenides by Optical Spectroscopy*, Nano Letters **17**, 740 (2017).

[Wan18] G. Wang, A. Chernikov, M. M. Glazov, T. F. Heinz, X. Marie, T. Amand, and B. Urbaszek, *Colloquium: Excitons in atomically thin transition metal dichalcogenides*, Reviews of Modern Physics **90**, 21001 (2018).

[Wan19] Z. Wang, D. A. Rhodes, K. Watanabe, T. Taniguchi, J. C. Hone, J. Shan, and K. F. Mak, *Evidence of high-temperature exciton condensation in two-dimensional atomic double layers*, Nature **574**, 76 (2019).

[Wan20a] C. Wang, F. Yang, and Y. Gao, *The highly-efficient light-emitting diodes based on transition metal dichalcogenides: From architecture to performance*, Nanoscale Advances **2**, 4323 (2020).

[Wan20b] L. Wang, E. M. Shih, A. Ghiotto, L. Xian, D. A. Rhodes, C. Tan, M. Claassen, D. M. Kennes, Y. Bai, B. Kim, K. Watanabe, T. Taniguchi, X. Zhu, J. Hone, A. Rubio, A. N. Pasupathy, and C. R. Dean, *Correlated electronic phases in twisted bilayer transition metal dichalcogenides*, Nature Materials **19**, 861 (2020).

[Wan20c] T. Wang, Z. Li, Y. Li, Z. Lu, S. Miao, Z. Lian, Y. Meng, M. Blei, T. Taniguchi, K. Watanabe, S. Tongay, D. Smirnov, C. Zhang, and S. F. Shi, *Giant Valley-Polarized Rydberg Excitons in Monolayer WSe_2 Revealed by Magneto-photocurrent Spectroscopy*, Nano Letters **20**, 7635 (2020).

[Wan20d] T. Wang, S. Miao, Z. Li, Y. Meng, Z. Lu, Z. Lian, M. Blei, T. Taniguchi, K. Watanabe, S. Tongay, D. Smirnov, and S. F. Shi, *Giant Valley-Zeeman Splitting from Spin-Singlet and Spin-Triplet Interlayer Excitons in $WSe_2/MoSe_2$ Heterostructure*, Nano Letters **20**, 694 (2020).

[Wes20] A. Weston, Y. Zou, V. Enaldiev, A. Summerfield, N. Clark, V. Zólyomi, A. Graham, C. Yelgel, S. Magorrian, M. Zhou, J. Zultak, D. Hopkinson, A. Barinov, T. H. Bointon, A. Kretinin, N. R. Wilson, P. H. Beton, V. I. Fal'ko, S. J. Haigh,

and R. Gorbachev, *Atomic reconstruction in twisted bilayers of transition metal dichalcogenides*, Nature Nanotechnology **15**, 592 (2020).

[Wil17] N. R. Wilson, P. V. Nguyen, K. Seyler, P. Rivera, A. J. Marsden, Z. P. Laker, G. C. Constantinescu, V. Kandyba, A. Barinov, N. D. Hine, X. Xu, and D. H. Cobden, *Determination of band offsets, hybridization, and exciton binding in 2D semiconductor heterostructures*, Science Advances **3**, 1 (2017).

[Woo14] C. R. Woods, L. Britnell, A. Eckmann, R. S. Ma, J. C. Lu, H. M. Guo, X. Lin, G. L. Yu, Y. Cao, R. V. Gorbachev, A. V. Kretinin, J. Park, L. A. Ponomarenko, M. I. Katsnelson, Y. N. Gornostyrev, K. Watanabe, T. Taniguchi, C. Casiraghi, H. J. Gao, A. K. Geim, and K. S. Novoselov, *Commensurate-incommensurate transition in graphene on hexagonal boron nitride*, Nature Physics **10**, 451 (2014).

[Woź20] T. Woźniak, P. E. Faria Junior, G. Seifert, A. Chaves, and J. Kunstmann, *Exciton g factors of van der Waals heterostructures from first-principles calculations*, Physical Review B **101**, 1 (2020).

[Wu13] S. Wu, C. Huang, G. Aivazian, J. S. Ross, D. H. Cobden, and X. Xu, *Vapor-Solid Growth of High Optical Quality MoS_2 Monolayers with Near-Unity Valley Polarization*, ACS Nano **7**, 2768 (2013).

[Xi15] X. Xi, L. Zhao, Z. Wang, H. Berger, L. Forró, J. Shan, and K. F. Mak, *Strongly enhanced charge-density-wave order in monolayer $NbSe_2$*, Nature Nanotechnology **10**, 765 (2015).

[Xi16] X. Xi, H. Berger, L. Forró, J. Shan, and K. F. Mak, *Gate Tuning of Electronic Phase Transitions in Two-Dimensional $NbSe_2$*, Physical Review Letters **117**, 1 (2016).

[Xia12] D. Xiao, G. B. Liu, W. Feng, X. Xu, and W. Yao, *Coupled spin and valley physics in monolayers of MoS_2 and other group-VI dichalcogenides*, Physical Review Letters **108**, 1 (2012).

[Xu14] X. Xu, W. Yao, D. Xiao, and T. F. Heinz, *Spin and pseudospins in layered transition metal dichalcogenides*, Nature Physics **10**, 343 (2014).

[Xua20] F. Xuan and S. Y. Quek, *Valley Zeeman effect and Landau levels in two-dimensional transition metal dichalcogenides*, Physical Review Research **2**, 033256 (2020).

[Yao08] W. Yao, D. Xiao, and Q. Niu, *Valley-dependent optoelectronics from inversion symmetry breaking*, Physical Review B **77**, 235406 (2008).

[Ye16] F. Ye, J. Lee, J. Hu, Z. Mao, J. Wei, and P. X. Feng, *Environmental Instability and Degradation of Single- and Few-Layer WTe_2 Nanosheets in Ambient Conditions*, Small **12**, 5802 (2016).

[Yoo19] H. Yoo, R. Engelke, S. Carr, S. Fang, K. Zhang, P. Cazeaux, S. H. Sung, R. Hovden, A. W. Tsen, T. Taniguchi, K. Watanabe, G. C. Yi, M. Kim, M. Luskin, E. B. Tadmor, E. Kaxiras, and P. Kim, *Atomic and electronic reconstruction at the van der Waals interface in twisted bilayer graphene*, Nature Materials **18**, 448 (2019).

[Yu17] H. Yu, G.-B. Liu, J. Tang, X. Xu, and W. Yao, *Moiré excitons: From programmable quantum emitter arrays to spin-orbit-coupled artificial lattices*, Science Advances **3**, e1701696 (2017).

[Yua20] L. Yuan, B. Zheng, J. Kunstmann, T. Brumme, A. B. Kuc, C. Ma, S. Deng, D. Blach, A. Pan, and L. Huang, *Twist-angle-dependent interlayer exciton diffusion in WS_2-WSe_2 heterobilayers*, Nature Materials **19**, 617 (2020).

[Zai14] O. Zaitov and V. A. Kolchuzhin, *Bitter coil design methodology for electromagnetic pulse metal processing techniques*, Journal of Manufacturing Processes **16**, 551 (2014).

[Zen12] H. Zeng, J. Dai, W. Yao, D. Xiao, and X. Cui, *Valley polarization in MoS_2 monolayers by optical pumping*, Nature Nanotechnology **7**, 490 (2012).

[Zha13a] X. Zhang, W. P. Han, J. B. Wu, S. Milana, Y. Lu, Q. Q. Li, A. C. Ferrari, and P. H. Tan, *Raman spectroscopy of shear and layer breathing modes in multilayer MoS_2*, Physical Review B **87**, 115413 (2013).

[Zha13b] Y. Zhao, X. Luo, H. Li, J. Zhang, P. T. Araujo, C. K. Gan, J. Wu, H. Zhang, S. Y. Quek, M. S. Dresselhaus, and Q. Xiong, *Interlayer breathing and shear modes in few-trilayer MoS_2 and WSe_2*, Nano Letters **13**, 1007 (2013).

[Zha14] Y. Zhang, T. R. Chang, B. Zhou, Y. T. Cui, H. Yan, Z. Liu, F. Schmitt, J. Lee, R. Moore, Y. Chen, H. Lin, H. T. Jeng, S. K. Mo, Z. Hussain, A. Bansil, and Z. X. Shen, *Direct observation of the transition from indirect to direct bandgap in atomically thin epitaxial $MoSe_2$*, Nature Nanotechnology **9**, 111 (2014).

[Zha15] X.-X. Zhang, Y. You, S. Y. F. Zhao, and T. F. Heinz, *Experimental Evidence for Dark Excitons in Monolayer WSe_2*, Physical Review Letters **115**, 257403 (2015).

[Zha16] J. Zhang, J. H. Wang, P. Chen, Y. Sun, S. Wu, Z. Y. Jia, X. B. Lu, H. Yu, W. Chen, J. Q. Zhu, G. B. Xie, R. Yang, D. X. Shi, X. L. Xu, J. Y. Xiang, K. H. Liu, and G. Y. Zhang, *Observation of Strong Interlayer Coupling in MoS_2/WS_2Heterostructures*, Advanced Materials **28**, 1950 (2016).

[Zha17] C. Zhang, C. P. Chuu, X. Ren, M. Y. Li, L. J. Li, C. Jin, M. Y. Chou, and C. K. Shih, *Interlayer couplings, Moiré patterns, and 2D electronic superlattices in MoS_2/WSe_2 hetero-bilayers*, Science Advances **3**, 1 (2017).

[Zhu11] Z. Y. Zhu, Y. C. Cheng, and U. Schwingenschlögl, *Giant spin-orbit-induced spin splitting in two-dimensional transition-metal dichalcogenide semiconductors*, Physical Review B **84**, 153402 (2011).

[Zip18] J. Zipfel, J. Holler, A. A. Mitioglu, M. V. Ballottin, P. Nagler, A. V. Stier, T. Taniguchi, K. Watanabe, S. A. Crooker, P. C. Christianen, T. Korn, and A. Chernikov, *Spatial extent of the excited exciton states in WS_2 monolayers from diamagnetic shifts*, Physical Review B **98**, 1 (2018).

[Zom14] P. J. Zomer, M. H. Guimarães, J. C. Brant, N. Tombros, and B. J. Van Wees, *Fast pick up technique for high quality heterostructures of bilayer graphene and hexagonal boron nitride*, Applied Physics Letters **105** (2014).

Danksagung

Abschließend möchte ich allen danken, die zum Gelingen dieser Arbeit beigetragen haben.

Vielen Dank an Tobias Korn, für Deine hervorragende Betreuung in allen Phasen der Dissertation, für Deine Hilfsbereitschaft sowohl im Labor als auch bei der Auswertung und Deinen tollen Humor. Dadurch haben mir die gemeinsamen Jahre mehr Spaß als Arbeit gemacht.
Vielen Dank an Christian Schüller, für die freundliche Aufnahme in Deine Arbeitsgruppe, Dein offenes Ohr für alle Belange und Deine Fähigkeit, schwierige physikalische Themen einfach zu vermitteln.
Ein großer Dank geht an meine Masteranden Marten Scheuck und Philipp Parzefall und Bachelorand/innen Erik Schäfer, Julia Wollny und Jan Markl. Ihr habt einen großen Teil zu dieser Arbeit beigetragen und die Zusammenarbeit mit Euch hat mir immer Spaß gemacht.
Besonders danken möchte ich der Arbeitsgruppe Schüller, für die tolle Atmosphäre, die Hilfsbereitschaft und die gelungene Unterhaltung während der Mittagspausen. Philipp Nagler, Deine Einführung in die Messaufbauten und die fachlichen Erklärungen haben mir sehr geholfen. Michael Kempf, vielen Dank für das Korrekturlesen der Dissertation und die schöne Zeit, sowohl bei der Arbeit als auch privat, im Exil, auswärts, etc. Simon Raiber, vielen Dank für die Korrektur, das Hinterfragen von Allem, die interessanten Diskussionen und den sportlichen Ausgleich. Danke an Eva Weiss, für Deine Hilfe bei bürokratischen Aufgaben, an Sebastian Krug für Deine technische Unterstützung und an Christof Ermer, für Deine Hilfsbereitschaft und die humorvollen Sprüche und Kommentare. Danke an Sven Gelfert, Sebastian Meier, Andreas Beer, Michael Högen und alle anderen Mitglieder der Arbeitsgruppe. Ich hatte und habe eine super Zeit mit Euch.

Teile dieser Arbeit wurden durch Kooperationen mit Gruppen aus Regensburg ermöglicht. Dafür danke ich Kai-Qiang Lin, Jonas Bauer, Jonas Zipfel, Alexey Chernikov, Lorentz Bauriedl und Nicola Paradiso.
Die Möglichkeit im Hochmagnetfeldlabor in Holland zu messen war eine einzigartige Erfahrung, die auch meine Arbeit bereichert hat. Anatolie Mitioglu, Mariana Ballottin, Peter Christianen, i want to thank you very much for the exciting measurements and the good time we had together.
Für die theoretische Unterstützung möchte ich mich einerseits bei Jens Kunstmann, Thomasz Woźniak und Andrey Chaves und andererseits bei Malte Selig, Florian Katsch und Andreas Knorr bedanken. Vor allem persönliche Treffen haben mir wissenschaftlich weitergeholfen und Spaß gemacht.
Danke an Mama und Papa, für Eure Unterstützung in jeder Lage und für die Ermöglichung meines Studiums. Vielen Dank an Maria und Anna, Ihr seid meine Lieblingsschwestern. Danke an Ruth, Du gibst mir sehr viel Kraft.